A STUDY OF ULTRA-LOW FRICTION IN TWO-DIMENSIONAL MATERIALS USING DENSITY-FUNCTIONAL THEORY

by

Tilas Kabengele

Submitted in partial fulfillment of the requirements

for the degree of Master of Science

at

Dalhousie University

Halifax, Nova Scotia

July 2021

This thesis is dedicated to my mom, Victoria, and dad, Tilas Snr., who have always believed in me and supported me. Thank you for the love, care, and provision, even in times when you could not afford it. Thank you for teaching me from a young age to work hard, pursue my dreams, and keep believing that all things are possible.

Contents

List of Figures

List of Tables

List of Abbreviations and Symbols Used

Abbreviation	Description
AFM	Atomic Force Microscopy, Atomic Force Microscope
APW	Augmented Plane-Wave
b-P	Blue phosphorene
B86bPBE	B86b exchange/PBE correlation functional
CAD	Canadian dollars
COMB	Charge-Optimized Many Body
CC	Coupled Cluster
CI	Configuration Interaction
COD	Crystallography Open Database
DFA	Density-Functional Approximation
DFT	Density-Functional Theory
D2	Grimme's Disperison correction model 2
D3	Grimme's Dispersion correction model 3
EAM	Embedded Atom Method
FFM	Friction Force Microscopy, Friction Force Microscope
FK	Frenkel–Kontorova
FKT	Frenkel–Kontorova-Tomlinson model
GGA	Generalized-Gradient Approximation
h-BN	Hexagonal boron nitride
HF	Hartree-Fock theory
HK	Hohenberg-Kohn
HOPG	Highly Oriented Pyrolytic Graphene
KS	Kohn-Sham
LDA	Local Density Approximation
L-J	Lennard-Jones
MBD	Many-Body Dispersion model
MD	Molecular Dynamics
MP	Monkhorst-Pack
MP2	Møller-Plesset second-order perturbation theory
MoS_2	Molybdenum disulfide
$MoSe_2$	Molybdenum diselenide

Abbreviation	Description
PAW	Projector Augmented Wave
PBE	Perdew-Burke-Ernzerhof exchange-correlation functional
PES	Potential Energy Surface(s)
PT	Prandtl–Tomlinson model
REBO	Reactive Empirical Bond-Order
SCF	Self-Consistent Field
STM	Scanning Tunneling Microscopy
TMDC	Transition-metal DiChalcogenides
TS-vdW	Tkatchenko-Scheffler van der Waals method
TBLG	Twisted BiLayer Graphene
UHV	Ultra-High Vacuum
XDM	eXchange-Hole Dipole Moment dispersion model
2D	Two-Dimensional

Symbol	Description
AA	AA-stacked structure
AB	AB-stacked structure
a.u.	Atomic unit
a_1, a_2	XDM damping parameters
Å	Angstrom
a_o, b_o	Lattice vectors of overlayer
a_s, b_s	Lattice vectors of substrate
a_m, b_m	Moiré lattice vectors of substrate
$C_n \ (n = 6, 8, 10)$	Dispersion coefficients
d	Interlayer distance
$\boldsymbol{d}_X$	Exchange-hole dipole moment
E	Energy (see main text for specific definitions)
E_{xc}	Exchange-correlation functional
E_{c}	Correlation functional
E_{x}	Exchange functional
$E_{\mathrm{x}}^{\mathrm{GGA}}$	Exchange functional in the GGA model
$E_{\mathrm{x}}^{\mathrm{LDA}}$	Exchange functional in the LDA model
F_r	Friction force
F_N	Normal force

Symbol	Description
f_{ext}	External normal load
eV	Electron volt
$\mathbf{F_k}$	Plane wave propagated in the direction $\mathbf{k}$
$f(R_{ij\mathbf{L}})$	Becke-Johnson damping function used in XDM
$\boldsymbol{G}$	Reciprocal lattice vector
h_X	Exchange hole
$\mathbf{k}$	Wave vector
$\mathbf{L}$	Lattice vector
L	Moiré pattern periodicity
l	Graphite mesa edge length
m, n	Integer indices from the Moiré pattern scheme
Q_σ	Curvature
$\boldsymbol{R}$	Bravais lattice vector
$\boldsymbol{r}$	(Electronic) Position vector
$R_{c,ij}$	Critical radius between atoms i and j
$R_{\text{vdW},ij}$	van der Waals radius between atoms i and j
T	Kinetic energy
T_o	Kinetic energy of non-interacting system
U	Hartree energy
$u(\mathbf{r})$	Periodic potential felt by electron at point $\mathbf{r}$
V	Potential energy
v_{ext}	External potential
v_o	Kohn-Sham potential
α_i^{at}	Reference free-atom polarizabilities
ΔE	Relative interaction energy
δ	Lattice-constant dissimilarity
δ_c	Critical value of the lattice-constant dissimilarity
δ_{ij}	Kronecker delta
ϵ	Kohn-Sham orbital energy
ϵ^{GGA}	Gradient correction
κ	Moiré factors
λ	Lagrange multipliers
μ	Coefficient of friction
ρ	Electron density

Symbol	Description
σ	Spin index
τ_σ	Kinetic-energy density
τ_f	Shear strength
Φ	Kohn-Sham electronic wavefunction
ψ	Kohn-Sham orbital
φ	Relative rotation angle between Moiré lattice vectors and substrate vectors
θ	Relative rotation angle between Moiré lattice vectors and overlayer vectors
χ	Reduced gradient density
$^\circ$	Degree
∇	Gradient operator

Acknowledgements

Abstract

Overcoming friction in any mechanical system is a universal problem in many aspects of engineering and nanotechnology. Being a dissipative force, friction reduces the efficiency of the system while adding unwanted heat and introducing wear between the surfaces in contact. Solid lubricants have attracted increasing attention in recent years and are starting to gain preference over petroleum-based lubricants because of their biodegradable properties and high-temperature tolerance, which makes them ideal candidates for clean technologies, aviation, aerospace, and defense-related applications.

In this thesis, I theoretically investigate a unique ultra-low frictional property in two-dimensional (2D) materials, known as *structural superlubricity*. Superlubricity has been experimentally observed in a wide range of 2D materials, including graphene, molybdenum disulfide, hexagonal boron nitride (h-BN). It is generally accepted that structural superlubricity in 2D materials arises from the geometrical misalignment of the surfaces in contact, known as *incommensurability*. However, recent studies using molecular dynamics simulations have concluded that incommensurability may not be a requirement for the superlubric behavior in MoS_2. In their work, low-friction regimes were achieved by applying the driving force in a direction that follows an energetically favourable trajectory.

Herein, I present a detailed analysis of friction in commensurate, and structurally incommensurate, bilayer graphene, h$-$BN, MoS_2, and a novel material blue phosphorene, using dispersion-corrected density-functional theory (DFT). For each material, interlayer sliding has been modeled, the associated energy barriers computed, and the corresponding potential energy surfaces plotted. DFT calculations are limited to periodic systems when plane-wave basis sets are employed, hindering the study of the incommensurate geometries that give rise to superlubricity. In this work, this limitation has been circumvented for the first time by using established concepts from Moiré pattern theory. A Moiré pattern scheme was implemented in a python program with the capability of creating Moiré unit cells of arbitrary size, and for any bilayer material, that satisfy the periodic boundary conditions for DFT codes. These unit cells simulate structural incommensurability and, therefore, are expected to exhibit frictional properties that resemble those of real incommensurate structures. For each material studied in this work, rotation angles of $0°$ for the commensurate case, and $21.79°$, $32.20°$, and $13.17°$ for the incommensurate counterparts were considered. Finally, the coefficients of friction for each configuration have been reported and are found to remain 1-2 orders of magnitude lower for the incommensurate structures. Provided the rotation barriers can be overcome, superlubricity is expected to occur in the rotated structures. The theoretical insights obtained in this work will hopefully motivate new experimental strategies that will aid in the design of industrially applicable superlubricants.

Chapter 1

Introduction

1.1 Friction and Lubrication

Friction is the force that resists the relative motion of two bodies in contact. Friction is ubiquitous in our daily lives and nature, permeating nearly all physical and mechanical processes within and around us. From internal biological phenomena in our bodies, such as peripheral resistance during blood flow, to external everyday activities like walking, sitting, or driving – friction is everywhere. However, friction is a very complex force arising from the combination of a wide range of factors, including surface roughness, inter-surface adhesion, surface deformations, contamination at the interface, etc. Due to such intricacies, studies on friction have for many years been limited to empirical formalisms, which have successfully provided us with intuitive and qualitative understanding of the frictional properties of materials. Empirical approaches alone, however, are incapable of fully rationalizing and predicting the frictional behavior of specific materials and systems.

Attempts to formulate a fundamental description of friction date as far back in time as Leonardo da Vinci, Guillaume Amontons, and Charles-Augustin de Coulomb, among many others whose efforts have inspired further work on friction in engineering and applied science.[1] Tribology is a branch of engineering solely dedicated to exploring better ways of overcoming friction. In practice, friction is combated by introducing lubricants between the surfaces of the moving parts, which promotes smooth interaction between contact surfaces, reduces wear, and maximizes the overall mechanical efficiency of the system.

A wide variety of lubricants exist today, from solid to semi-solid, liquid, and gas-phase lubricants. The ultimate goal of modern tribology is to design high-performance lubricants that are chemically inert and capable of enduring large loads and harsh environments. Liquid and semi-solid lubricants, such as oil and grease, are suitable for high-speed and high-load applications in a wide range of environments

due to their chemical inertness and ease of use. As a result, these lubricants have continued to dominate the market since the industrial revolution and remain the most widely used.

However, given what we now know about climate change and how petroleum-based lubricants contribute to the pollution of the environment, solid lubricants are the most attractive alternative, with graphite and molybdenum disulfide (MoS_2) being some of the most commonly used.[2] Numerous studies have examined the economic and environmental benefits of good tribological practices.[3–5] It has been shown in these studies that implementing better friction reduction techniques would reduce CO_2 emissions worldwide. The recent study by Holmberg *et al.*,[5] for example, highlights that utilizing new friction reduction techniques in cars alone could reduce the energy lost through friction by 18% in the short-term (5-10 years), and by about 61% in the long-term (15-25 years). This corresponds to $174,000$ million euros ($\sim 257,000$ million CAD), and $576,000$ million euros ($\sim 850,000$ million CAD) in global economic savings, respectively. Therefore, promoting clean lubrication is a beneficial endeavor for both the economy and the environment.

Other substitutes for petroleum-based lubricants include biodegradable lubricants, such as wheat flour, starch, and vegetable oils. Although such lubricants do not pose a threat to the environment, they degrade at much lower temperatures for most application purposes.[6] Solid lubricants, on the other hand, can withstand very high temperatures, pressure, and radiation. These attributes make them well-suited for applications such as lubrication of aerospace, aviation, and defense machinery. To this effect, two-dimensional (2D) layered materials, such as graphite, MoS_2, and hexagonal boron nitride (h$-$BN), could be the most promising class of lubricants today.

The impacts of friction on production costs and machinery repairs became apparent during the industrial revolution. Efforts to understand the nature of friction were no longer mere academic or intellectual pursuits, but urgent, high-priority endeavors that would accelerate the design of effective lubricants and increase profits. Experimental studies were limited to macro-scale analyses of the physical and mechanical properties of materials, while theoretical approaches began to hint at the atomistic description of friction. In the early 20th century, Ludwig Prandtl, a German physicist, and two soviet scientists, Yakov Frenkel and Tatiana Kontorova, independently developed the first viable atomistic models that have come to be widely recognized today as the Prandtl–Tomlinson (PT),[7] and the Frenkel–Kontorova (FK)[8,9] models, respectively. These ideas, however, only came to be verified a few decades ago with the emergence of more sophisticated experimental techniques, such as Scanning Tunneling Microscopy (STM), Frictional Force Microscopy (FFM), and Atomic Force Microscopy (AFM).[10] These studies have shown that the fundamental origin of friction is from atomistic locking between constituent atoms of the surfaces in contact.[11]

1.2 Superlubricity

In the early '90s, Hirano *et al.* predicted that friction would completely vanish if the surfaces in contact were atomically flat, rigid, clean, weakly interacting, and structurally non-matching, i.e., incommensurate.[11] Hirano referred to this ultra-low friction state as *superlubricity.*[12] In 2004, Dienwiebel *et al.* experimentally verified superlubricity between two graphene surfaces[13] using an AFM. Similar studies have examined ultra-low friction in a wide range of lamellar materials, including heterostructures of graphene, transition metals, and transition-metal dichalcogenides (TMDCs).[14–16] Researchers in recent years have examined how physical characteristics, such as layer dependence, structural orientation, temperature, and pressure, relate to ultra-low frictional properties of materials.[17–19]

Despite the tremendous progress on friction and lubrication through both theoretical and experimental efforts over the years, the nature and origin of superlubricity remain speculative. For instance, structural incommensurability is considered a vital requirement for superlubricity. Contrastingly, in a 2019 theoretical study, Claerbout *et al.* suggested that incommensurability may not be a requirement for superlubricity in MoS_2.[20] In their study, low-friction regimes were attained by varying the trajectory of the driving force and avoiding high-friction energy barriers on the Potential Energy Surface (PES) landscape of commensurate (i.e., structurally aligned) MoS_2.

For commensurate 2D layered materials, the periodicity of the upper body, e.g., the top layer in a bilayer material, aligns with the periodicity of the lower body (bottom layer). Incommensurate structures, on the other hand, are characterized by lattice mismatches due to lattice-constant dissimilarities, or relative rotation of one of the layers (see Figure 1.1). The resulting geometrical mismatch of the periodic lattices can be understood as large-scale interference patterns, known as *Moiré patterns* (see Figure 1.2). Moiré patterns, and therefore incommensurability, are only achievable in homogeneous structures if the upper body rotates or twists relative to the lower body.[21–23]

Moiré pattern theory is a detailed mathematical description of Moiré lattices. Moiŕe pattern theory is focused on the geometrical features of the system, such as the lattice-constant dissimilarity between the upper and lower bodies, $\delta = a_1/a_2 - 1$, where a_1 and a_2 are the lattice constants of the top and bottom layers (or vice versa), and $a_1 > a_2$; the periodicity of the given Moiré structure, $L = \sqrt{3}d/(2\sin\frac{\varphi}{2})$, where d is the bond length; and the rotation angle, φ. Analyzing L, δ, and φ allows us to understand the periodicities of the Moiré lattice and study incommensurability geometrically. As detailed later in this work, Moiré pattern theory has enabled us to create unit cells that satisfy periodic boundary conditions for planewave DFT codes, making it possible, for the first time, to study superlubricity in homogeneous materials from first principles.

Figure 1.2 shows the evolution of Moiré patterns for selected values of φ between $0°$ and $60°$. The period L of the Moiré pattern increases as φ approaches $0°$ or $60°$. A perfectly commensurate configura-

Figure 1.1: Illustration of commensurate and incommensurate periodicities. For commensurate configurations, the periodicity of the top layer aligns with the periodicity of the bottom layer. Incommensurate structures, on the other hand, are characterized by lattice mismatches facilitated by lattice-constant dissimilarities, and/or the relative rotation of one of the layers.

(a) COMMENSURATE   **(b)** INCOMMENSURATE
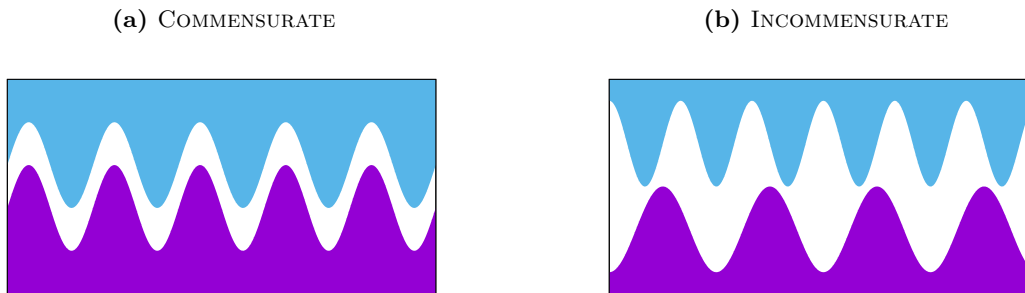
tion, e.g., a (1×1) unit cell with no rotation, can be thought of as a structure with an upper limit of L. As $L \to \infty$, a given incommensurate configuration will become less misaligned, and more commensurate. The opposite of this is also true; a highly incommensurate configuration will have no periodicity at all. Commensurate states have been observed to have large L compared to incommensurate ones, and φ is typically less than δ. Talapov defined a critical value for δ, such that, if $\delta > \delta_c$, the geometry transitions to an incommensurate state, otherwise the structure is commensurate.[24] δ_c is influenced by a critical temperature, T_c, given by the elastic moduli of the crystal lattice, and is, therefore, material dependent.

In an experimental study using atomic force microscopy (AFM), scanning tunnelling microscopy (STM), and Raman spectroscopy to measure the strain distribution in graphene adsorbed on h−BN at different rotation angles, a commensurate-incommensurate transition in the heterostructure was observed when φ was on the order of δ.[25] For $\varphi < \delta$, graphene stretched locally to achieve an energetically favourable commensurate state with h−BN, while regions where $\varphi > \delta$ were shown to be incommensurate. In fact, examining the geometrical patterns on a Moiré lattice of graphene has shown regions of both AA and AB stacked patterns periodically arranged on the lattice.[26] This means that, geometrically, a Moiré lattice is a combination of different atomic stacking.

In superlubricity studies (including this work), unique frictional properties in incommensurate structures have been mainly attributed to structural misorientations (i.e., Moiré patterns) rather than strain or stress distributions. Thus, all the rotated structures studied in this work have been geometrically constructed from Moiré pattern theory. Although details of experimental conditions, such as strain, stress, or temperature, are not incorporated in Moiré pattern theory, these structures are expected to retain the physical properties of real structural incommensurability in the context of superlubricity. This is the case because the important feature of structural incommensurability for achieving superlubricity is the geometrical mismatch of the atoms. For example, in Dienwiebel's superlubricity experiments on graphite, all configurations with mismatched atoms showed similar superlubric effects, while the commensurate configurations with φ of 0°, 60°, 120°, etc., exhibited high friction (see Figure 1.3).

Figure 1.2: The evolution of Moiré patterns for selected values of φ between $0°$ and $55°$. The period L of the Moiré pattern increases as φ approaches $0°$ or $60°$. A perfectly commensurate configuration, (a), can be thought of as a structure with an upper limit of L. As $L \to \infty$, a given incommensurate configuration will become less misaligned, and more commensurate. The Moiré structures are comprised of both AA and AB stacked regions periodically arranged within the lattice.

(a) $0.00°$ **(b)** $1.70°$ **(c)** $3.48°$ **(d)** $5.36°$

(e) $7.34°$ **(f)** $9.43°$ **(g)** $11.64°$ **(h)** $13.96°$

(i) $16.43°$ **(j)** $19.03°$ **(k)** $21.79°$ **(l)** $24.70°$

(m) $27.80°$ **(n)** $31.07°$ **(o)** $34.54°$ **(p)** $38.21°$

(q) $42.10°$ **(r)** $46.22°$ **(s)** $50.57°$ **(t)** $55.16°$
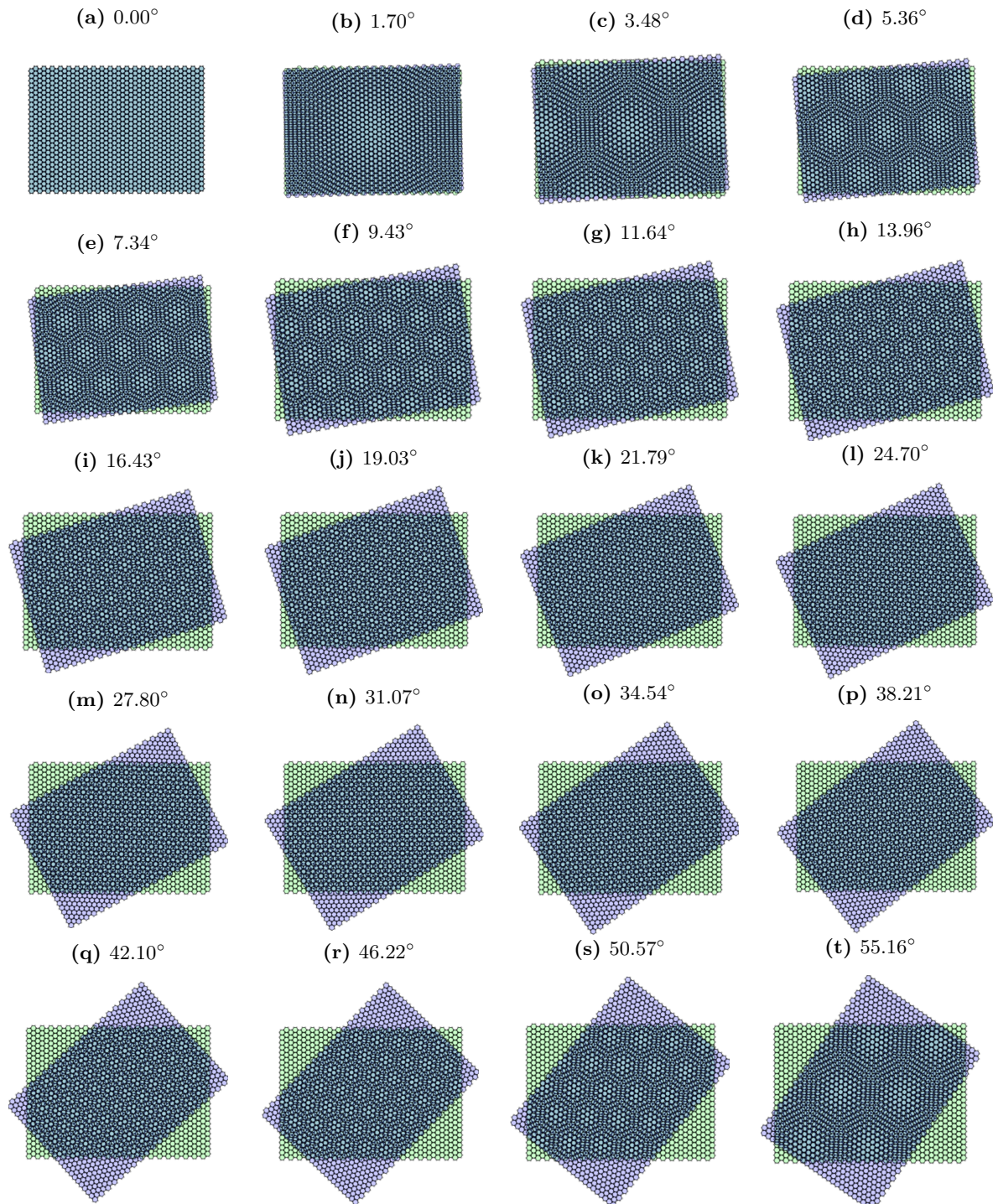
Superlubricity is generally greater in heterostructures than at homogeneous interfaces due to the intrinsic lattice-constant dissimilarity between the constituent layers in heterostructures, which supports incommensurability.[15] For homogeneous interfaces and structures with very similar lattice constants, commensurate configurations are more stable than incommensurate ones. The uniformity of the periodic lattices promotes the energetically favorable collapse to default commensurate orientations, making incommensurate geometries practically harder to sustain.[15, 27, 28]

Previous studies have investigated the behavior of friction at homogeneous interfaces and heterojunctions.[29–31] Notably, Vazirisereshk *et al.* recently examined the frictional behavior of MoS_2, graphene, and the graphene/MoS_2 heterostructure and observed the lowest friction not in the heterostructures, but in the homogeneous graphene layers.[31] The varying frictional behavior in these materials was attributed to the difference in the energy barriers during molecular sliding.

Studies such as those done by Claerbout *et al.*,[20] Vazirisereshk *et al.*,[31] and others, allude to the fact that our theories of friction and superlubricity are still incomplete. Further research focused on ultra-low friction at commensurate, incommensurate, homogeneous, and heterostructural interfaces must be conducted for a consensus view to be established.

1.2.1 Experimental Studies

Verification of Superlubricity

In 2004, Dienwiebel *et al.*[13] examined the energy dissipation for the tip of a frictional force microscope (FFM) sliding over a graphite surface under a dry nitrogen atmosphere. They measured the atomic-scale friction as a function of the rotational angle between the tip and the top layer of the graphite surface, and found ultra-low friction regimes between rotated graphite layers, as shown in Figure 1.3. Two narrow peaks of high friction were observed at around $0°$ and $60°$ rotation angles. These peaks correspond to commensurate configurations of the graphite hexagonal lattice and highlight the role of incommensurability in achieving ultra-low friction.

Further experimental studies have explored the limitations and practical challenges to achieving superlubricity at larger scales and under ambient conditions. Surface contamination and surface deformations increase under such conditions. Surface contamination introduces asperities on the surface that increase surface roughness, thereby promoting friction. Structural deformations have been observed at the interface of the overlayer and substrate during sliding. When the contact starts undergoing deformation, incommensurate states can be terminated, leading to the reorientation of the structure back into a commensurate high-friction configuration.[32] Such deformations are more significant in larger systems, and increase with normal load, temperature, and pressure.[33–38] This is a major impediment to achieving superlubricity at scales suitable for industrial applications.[39–41]

Figure 1.3: Average friction force versus rotation angle of a graphite sample around an axis normal to the sample surface. Two narrow peaks of high friction were observed at 0° and 61°, respectively. Between these peaks a wide angular range with ultra-low friction close to the detection limit of the instrument was found. The first peak has a maximum friction force of 306 ± 40 pN, and the second peak has a maximum of 203 ± 20 pN. The solid curve shows results from a model calculation for a 96-atom flake. Figure source: Ref. 13. Figure reused with permission from Dienwiebel *et al.*, Phys. Rev. Lett. **92** (2004). Copyright 2004 American Physical Society.
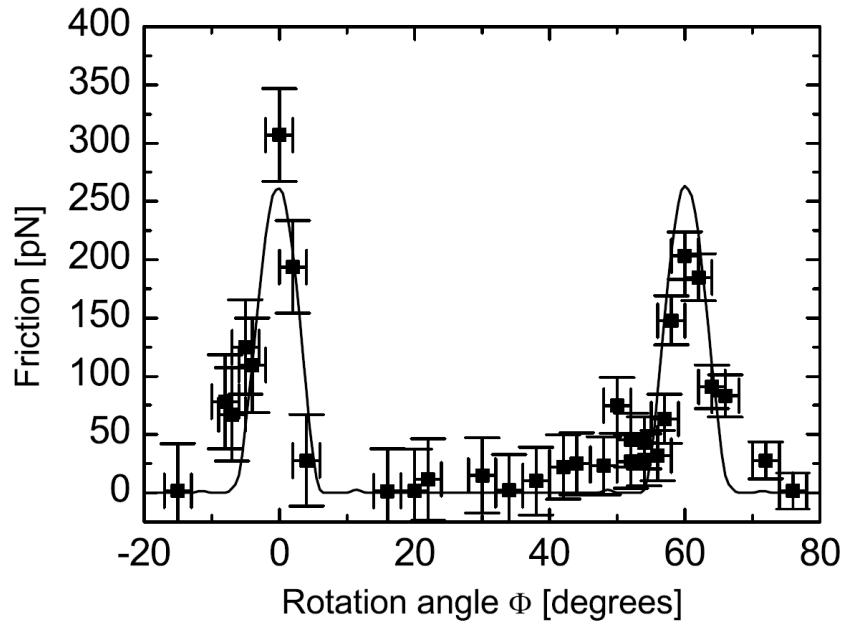
Self-Retraction of Graphite Microflakes

For a long time, surface experiments on superlubricity were limited to ultra-high vacuum (UHV) conditions (or at least dry nitrogen atmospheres) due to the issue of surface contamination. In 2012, Liu *et al.*[42] introduced a technique that addressed this problem and achieved microscale superlubricity. Liu's work was based on a novel phenomenon know as *self-retraction*, previously observed by Zheng *et al.*[43] in graphene microflakes. Here, tiny flakes of graphite, after being displaced to various suspended positions from islands of highly orientated pyrolytic graphite (HOPG), retracted back onto the islands under no external influences.[43]

In Liu *et al.*'s experiment,[42] a micromanipulator was used to shear a lithographically defined graphite mesa as shown in Figure 1.4. The shear stresses were measured for different self-retraction angles. The friction resistance force (i.e., the force resisting self-retraction) for the square graphite mesa of edge length L sheared to a distance x, is given by $F_f = \tau_f L(L - x)$, where τ_f is the shear strength. An upper bound of the areal friction stress, τ_f, was determined by analysing the friction resistance and self-retraction forces. For flakes in incommensurate contact during self-retraction, the friction at the interface was on the same order of magnitude as the superlubric regime reported by Dienwiebel *et al.*[13] Furthermore, lock-in rotation angles were observed at 0° and 60° symmetries, where self-retraction and shearing were almost completely suppressed. It was therefore concluded that self-retraction occurred due

Figure 1.4: The self-retraction mechanism of graphite using a micromanipulator. (a) After mechanical exfoliation, (1) a silicon dioxide (SiO_2) film is grown on the graphite surface by plasma-enhanced chemical vapor deposition, and the film is coated with photoresist. (2), (3) Microscopic SiO_2 squares are defined by electron beam lithography and (4) used as a mask for reactive ion etching of the squares into the HOPG, to define graphite mesas. SEM images of the top and side views of the mesas are shown. (b) Illustration of a mesa being partially sheared with a micromanipulator, to form a self-retracting flake on a graphite platform. When the microtip is raised to release the flake, it automatically returns to its original position on the mesa.(c) Observation of this process in a vacuum in a SEM.(d) Observation of the same process under ambient conditions with an optical microscope. Figure source: Ref. 42. Figure reused with permission from Liu *et al.*, Phys. Rev. Lett. **20** (2012). Copyright 2012 American Physical Society.
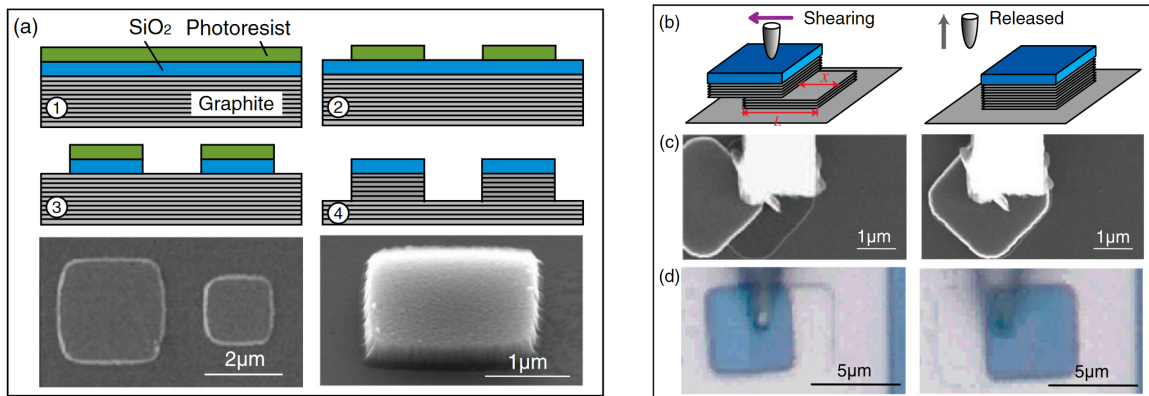
to structural lubricity between the surfaces in contact. Liu's work[42] was a significant step forward from nanoscale structural lubricity earlier demonstrated by Dienwiebel *et al.*[13] to achieving superlubricity in larger systems.

1.2.2 Theoretical Developments

The PT[7] and FK[8,9] models, initially developed to model one-dimensional (1D) friction, are widely employed to study friction at the atomic level. The PT and FK models have been further extended into the Frenkel-Kontorova-Tomlinson (FKT) model.[44,45] The difference between these models is illustrated in Figure 1.5. The PT model assumes that a point mass hanging on a spring of effective elastic constant k is dragged with velocity v over a 1D sinusoidal potential (mimicking the interaction between an AFM tip and a substrate). If x is the tip position, the total potential energy of the PT system can be written as[45]

$$V_{\text{PT}} = U \cos\left(\frac{2\pi x}{a}\right) + \frac{k}{2}(x - vt)^2, \tag{1.1}$$

where U is the amplitude of the sinusoidal corrugation potential, and a is its periodicity. The instantaneous lateral friction force in the PT model, and as measured in FFM experiments, is given by $F = -k(x - vt)$. The kinetic friction, F_k, is then the time average of F.

Predictions made with the PT model are often used to inform and guide more detailed models as they provide qualitative conclusions about the atomic-scale friction of a system. However, oversimplification by

the PT model omits physical features of the system that may carry crucial information about the system in some cases, particularly, the number of atoms in the upper body. In reality, the AFM tip consists of more than a single atom. The FK model thus assumes a more realistic approach by incorporating several atoms into the system. The FKT model, as an improvement to the FK model, further incorporates an elastic potential in the vertical direction of each individual atom in the system (instead of only 1), which results in a more accurate representation of interactions in the normal direction as the overlayer slides atop the substrate. The total potential energy of a FKT system with N particles will therefore be given by[45]

$$V_{\text{FKT}}(x,t) = \sum_{i=1}^{N} -\frac{1}{2}U\cos\left(\frac{2\pi x_i}{a}\right) + \sum_{i=1}^{N-1} -\frac{k_t}{2}(\Delta x_{i,i+1} - b)^2 + \sum_{i=1}^{N} \frac{k}{2}(vt + (i-1)b - x_i)^2, \quad (1.2)$$

where U is the amplitude of the sinusoidal corrugation potential, x_i is the displacement of the ith atom, a and b are, respectively, the lattice spacing in the lower and upper bodies (i.e., lattice constants) as shown in Figure 1.5, $\Delta x_{i,i+1}$ is the distance between adjacent atoms i and $i+1$, v is the sliding velocity, and t is the time. The first, second, and third terms are the corrugation potential, the elastic potential between the upper and lower bodies via horizontally connected elastic springs k_t, and the elastic potential due to tethering to the support vertically by springs k, respectively. The instantaneous friction force is then the sum of the forces experienced by the atoms in the upper body given by

$$F = \sum_{i=1}^{N} k(vt + (i-1)b - x_i). \quad (1.3)$$

From the FK/FKT models, the frictional properties of a system can be examined by studying the Hamiltonian dynamics conserving the energy and analyzing quantities such as the momentum, center of mass, and the sliding time of the upper body.[46–48] If we assume an extreme case where $k_t = \infty$, the corrugation potential, U_c, between the lower and upper bodies can be expressed as

$$U_c = -\frac{1}{2}U\sum_{i=1}^{N}\cos\left(\frac{2\pi(i-1)b + x}{a}\right) = -\frac{1}{2}U\frac{\sin(Nb\pi/a)}{\sin(b\pi/a)}\cos\left(\frac{\pi(Nb - b + 2x)}{a}\right). \quad (1.4)$$

Note the magnitude of the corrugation potential goes to zero if $Nb/a \in \mathbb{Z}$. In this case, the friction also goes to zero, assuming there is no viscous drag (i.e., phonon excitation). For realistic systems, it can be shown that, for any value of Nb/a, friction increases linearly with sliding velocity and contact area due to phonon excitation.[45] For this reason, some researchers have criticized the term "superlubricity", stating that it is misleading and could potentially be confused with the underlying physics of phenomena such as *superconductivity* and *superfluidity*. *Structural lubricity* (or *structural superlubricity*) was suggested by Müser[49] as a more appropriate term since it highlights the fact that ultra-low friction occurs mainly due to structural incommensurability of the crystal lattices, and not as a consequence of supercooling or
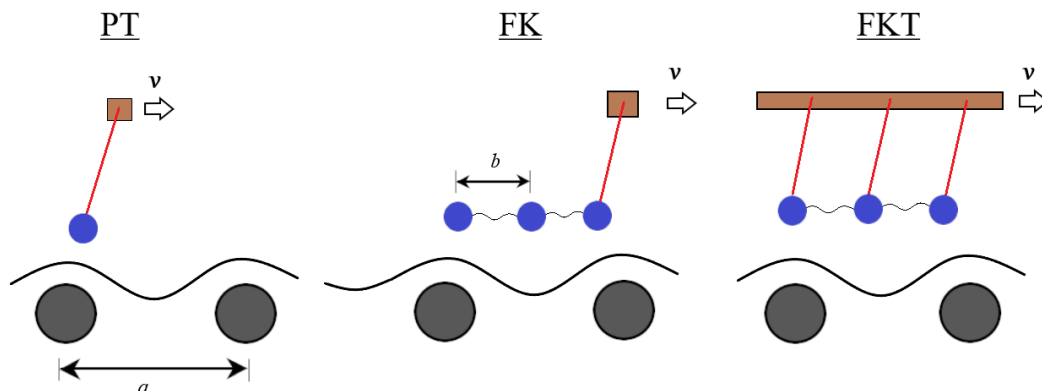
Figure 1.5: Illustrations of the 1D PT, FK, and FKT models. Large solid spheres represent the particles in the upper body (blue) and lower body (gray). a is the equilibrium distance between two particles in the lower body, while b is the lattice constant of the upper body. Atoms in the top layer feel the potential of the atoms in the bottom layer as the upper body slides atop the lower body. These models predict a "stick" (high friction peaks) and "slip" (low friction troughs) mechanism on the potential energy surface landscape. Superlubricity is predicted to occur when the interaction energy between the layers flattens due to a systematic cancellation of forces on atoms in incommensurate configurations.[45]

any physical manipulations of phonon excitation in the solid. In this work, the terms "superlubricity", "structural lubricity", or "structural superlubricity" are used interchangeably, all referring to ultra-low friction due to structural incommensurability.

Implementation of the PT and FK/FKT models in modern programming and mathematical modeling software, such as MATLAB/OCTAVE and others, is relatively easy.[45] The computational cost required for such codes is significantly lower than classical Molecular Dynamics (MD) simulations, or standard Density-Functional Theory (DFT).[39,45,50] While these classical models cannot provide the level of detail possible with full-fledged MD simulations or DFT, their simplistic approach enables investigation of atomic friction under almost all experimental conditions, some of which are inaccessible to MD (e.g., modeling long time scales) and DFT (e.g., modeling large systems).

1.2.3 Computational Modeling

Molecular Dynamics

MD is a computational approach that is widely used to study the frictional properties of surfaces and interfaces.[27,50–54] Classical MD simulations describe the interaction energy and dynamics of atoms using Newtonian mechanics. In MD simulations, it is possible to set a variety of parameters, e.g., normal load, velocity, temperature, contact area, compliance (relationship between force and stiffness in AFM experiments), and other properties. Different materials are specified by assigning empirical potentials fit to the system being investigated. Numerous potentials optimized for various purposes are available, including the Lennard-Jones (LJ) potential,[55] the Embedded Atom Method (EAM),[56] the reactive empirical bond-order (REBO) potential,[57] the adaptive intermolecular REBO potential,[58] and

ReaxFF,[59] among others.

A recent MD study of the interlayer friction and superlubricity in bilayer graphene and the MoS_2/$MoSe_2$ (molybdenum diselenide) van der Waals heterostructures investigated the effects of temperature, sliding velocity, and normal load on the ultra-low frictional properties of the system for a range of rotation angles.[27] The results showed a 2-3 order of magnitude drop in the coefficient of friction for incommensurate contacts. In both graphene and the MoS_2/$MoSe_2$ heterostructures, friction increased linearly with temperature, sliding velocity, and normal load. For the heterostructures, superlubricity was achieved in the range of rotation angles of $9° \leq \varphi \leq 51°$, while configurations with rotation angles close to the MoS_2/$MoSe_2$ commensurate contact ($\varphi \leq 10°$ and $\varphi \geq 50°$) exhibited significantly greater friction.

Classical MD simulations provide a good approximation of the dynamic and mechanical properties of a system. However, choosing an accurate empirical potential is critical to predicting realistic behaviour. Due to the numerous empirical potentials and parameters that exist, researchers need to be able to carefully evaluate the efficacy and accuracy of these models. A common challenge in MD simulations is capturing interactions between dissimilar materials. This has been addressed to a certain degree by implementing potentials purposefully designed to model materials that are composed of diverse chemical species. The charge-optimized many body (COMB) potential, for example, accommodates the simultaneous modeling of interactions between metals, oxides, and structures held together by covalent bonds.[60,61] The ReaxFF potential[59] has also been parametrized for a variety of materials. These recent developments in MD potentials have inevitably led to more accurate results. Nevertheless, classical MD simulations still remain less accurate than electronic-structure methods, such as density-functional theory (DFT), due to their heavy reliance on empirical parameters.

Density-Functional Theory

DFT is an *ab initio* quantum chemistry method for solving the electronic structure problem of a system. In the framework of Kohn-Sham (KS) DFT, the many-body Schrödinger equation of interacting particles is replaced by a set of single-particle Schrödinger equations (i.e., the KS equations) using a density-dependent effective potential, which is solved self-consistently until the total energy of the system is minimized. KS theory, together with the Hohenberg-Kohn (HK) theorems detailed later in this work, form the premise of most DFT methods. The main idea is that the kinetic, potential, exchange, and correlation (or *exchange-correlation*) energies can now be expressed as functionals of the electron density. The total energy of the system is then the sum of all the aforementioned energy terms. In KS DFT, both the kinetic- and potential-energy terms are exact for classical electrons, such that only the quantum-mechanical exchange-correlation term needs to be approximated. The accuracy of a DFT method will therefore depend on the quality of the exchange-correlation functional. For this reason, most of the research in DFT in the past years has been centered around finding more accurate formulations of the

exchange-correlation term.

Although the practical implementation of DFT requires a certain degree of approximation, in principle, DFT is an exact theory derived from the fundamental equations of physics and devoid of empirical data. The end result of the developments by Hohenberg, Kohn, and Sham has been the inception of a robust first-principles quantum-mechanical method with a reasonable trade-off between accuracy and computational cost. DFT has grown in popularity over the past few decades due to its relatively lower computational cost compared to traditional Hartree-Fock and post-Hartree-Fock methods, such as Coupled Cluster (CC) theory,[62–64] Configuration Interaction (CI),[65–67] and Møller-Plesset perturbation theory,[68–70] among many others.

From a first-principles approach, the frictional behavior of 2D materials can be studied by modelling the potential energy surface (PES) of the given system.[71–73] For interlayer sliding of a 2D material, the PES is defined by translation of the overlayer atop the substrate. At each static point on the PES, the atomic positions are optimized to minimize the electronic energy of the system. PES computed from DFT can be used to validate empirical potentials employed in classical MD, and can also be used as input for simple nanoscale models of friction, such as the PT and FK models.[78,9,74] DFT has also been previously employed in collaboration with experiments to study friction in commensurate homogeneous interfaces and heterostructures.[31,75] Other DFT studies of van der Waals materials have highlighted the importance of London dispersion interactions in the stabilization of these systems, and in understanding their tribological properties.[76,77] London dispersion is a type of van der Waals interaction that occurs when electrons are distributed asymmetrically about the nucleus to form temporary instantaneous dipoles between neighboring atoms. Although these interactions are quite small in magnitude in comparison to exchange and correlation, their collective contribution to the system is non-negligible. In fact, London dispersion plays an important role in determining various chemical and physical properties of molecular solids and surfaces, including conditions for phase changes, adsorption, adhesion, and friction.[76–80] Proper treatment of dispersion forces in 2D materials consequently leads to more accurate results. Conversely, neglecting these interactions may result in erroneous or even non-physical predictions.[78–80] In this regard, dispersion-corrected DFT is a far more accurate technique than classical MD simulations.

1.3 Thesis Objective

The goal of this research is to provide further insight into the intricacies of friction and superlubricity in 2D materials from a first-principles perspective. Bilayer structures of graphite, MoS_2, $h-BN$, and the novel material blue phosphorene ($b-P$) have been investigated. A detailed analysis of the behavior of friction in these materials has been carried out using DFT. In computational studies of superlubricity, large-scale calculations are often necessary to capture a realistic scope of the features in a system, e.g., the

periodicity of the Moiré patterns, the dissimilarity between the lattices, rotation, and so forth. However, standard DFT methods are limited to only a few hundred atoms and their utility confined to periodic systems when planewave basis sets are employed, prohibiting application to incommensurate structures. In this work, this limitation is circumvented for the first time by analyzing the Moiré patterns formed when the overlayer is rotated with respect to the substrate.[81–83] It is then possible to define computationally tractable, rotated unit cells with properties expected to resemble those of incommensurate interfaces and, hence, show superlubricity.[31, 71, 72, 75]

Additionally, non-local, long-range electron correlation effects are very important when studying layered materials. However, standard DFT methods do not include such long-range effects that give rise to London dispersion. The eXchange-hole Dipole Moment (XDM) dispersion model developed by Becke and Johnson, where the source of the instantaneous dipole moments is taken to be the dipole moment of the exchange hole,[84, 85] has been utilized in this work. Precise computations of the interaction energy between constituent atoms of the bilayers has provided a reliable assessment of friction between the interacting surfaces. Hopefully, this work sheds new light on friction in 2D materials and on achieving superlubricity in real systems.

The remainder of this thesis is structured as follows: Chapter **2** details the theoretical and computational methodologies used in this work, particularly, the fundamentals of DFT, and Moiré pattern theory for bilayer materials. Chapter **3** discusses the `BiCrystal` program – a python 3 algorithm developed for this work to create Moiré unit cells for DFT calculations. Chapter **4** explores structural superlubricity in homogeneous bilayers of graphene, h−BN, MoS_2, and b−P. Chapter **5** presents a detailed analysis of the coefficients of friction computed from DFT results. Chapter **6** summarizes and concludes the results and main ideas of this work.

Chapter 2

Theory and Methods

In this chapter, we shall review the computational tools and methods used in our study and discuss the underlying theory behind these methods.

In our pursuit of a more detailed description of friction, we need a sufficiently accurate understanding of the interactions between the surfaces in contact. An *ab initio* calculation is required in order to give insight into the electronic structure of these surfaces and provide us with information such as energy barriers and corrugation of the Potential Energy Surface (PES).

2.1 Density-Functional Theory

Over the past decades, Density-Functional Theory (DFT) has become one of the most powerful and widely used computational tools for modelling quantum-mechanical systems.[86] Much of this progress can be attributed to the rapid development of computing hardware as well as software, which has made it possible perform intensive computations that require large amounts of memory and computing power.[87–90]

The term *electronic structure* is used to describe the behavior of electrons in atoms, molecules or crystals. Like any other first-principles method, DFT attempts to solve the electronic-structure problem not by trying to fit to experimental data, but rather by solving the equations of quantum mechanics that describe the given system, i.e. solving the Schrödinger equation.

The foundations of DFT rest on three major developments:

1. The Born-Oppenheimer approximation (1927)[91]

2. The Hohenberg-Kohn Theorems (1964)[92]

3. Kohn-Sham Theory (1965)[93]

We shall examine each of these concepts briefly below.

2.1.1 The Born-Oppenheimer Approximation

Virtually all the chemistry of a material is determined by the electrons. However, for systems with many particles, solving the many-body Schrödinger equation (i.e. finding the orbitals and energy) is a great impediment due to the high dimensionality of the problem. The Born-Oppenheimer approximation reduces the complexity of this problem by assuming that all nuclei in the system are stationary. This premise is supported by the fact that, in comparison to the mass of an electron, the nucleus of any atom is much (at least 3 orders of magnitude) heavier. This is the first step towards building a practical DFT method.

2.1.2 The Hohenberg-Kohn (HK) Theorems

Theorem 1

From a purely quantum-mechanical understanding, the external potential determines all the properties of a system. Hohenberg and Kohn demonstrated that the mapping of the electron density to the external potential is unique and one-to-one, i.e. $\rho \to V$. They showed that the ground-state density uniquely determines the potential up to an arbitrary constant. This allows us to write the ground-state energy in the following manner:

$$E[\rho] = \min_{\rho} \left(F[\rho] + \int \rho(r)\, v_{\text{ext}}(r)\, d^3r \right), \tag{2.1}$$

where $\rho(r)$ is the electron density, and $F[\rho]$ is a functional containing the kinetic- and potential-energy contributions to the energy of the system.

Theorem 2

Further, Hohenberg and Kohn showed that the functional $F[\rho]$ exists and its form is universal for all systems. In theory, if we can find the exact form of this functional and minimize the result with respect to the density, this would give us the exact ground-state energy of the system. This brings us to the final part of HK theorems where we minimize the energy functional.

Theorem 3

From calculus of variations, we know that if we wish to minimize a functional $E[\rho]$ for a given $v_{\text{ext}}(r)$ while keeping the number of particles, N, fixed, we can do so via the Euler-Lagrange formalism.[94–96] In this scheme, the Lagrange multipliers method is used, where we minimize $E[\rho] - \lambda N$ and find the Euler-Lagrange equation:

$$\frac{\delta F}{\delta \rho(r)} + v_{\text{ext}}(r) = \lambda, \tag{2.2}$$

where λ is identified as the chemical potential of the system, $\lambda = \frac{\partial E}{\partial N}$. In theory, the exact functional derivative $\delta F / \delta \rho$ would give us the exact $v_{\text{ext}}(r)$. In practice, this is unfortunately not the case. This is because the functional $F[\rho]$ contains functionals of the kinetic and potential energy, which are themselves approximations. Finding a more accurate form of $F[\rho]$ is therefore paramount to having a density-functional theory that actually works.

2.1.3   Kohn-Sham Theory

The earliest attempt to formulate a density-functional theory was the Thomas-Fermi approach.[97]   In this method, Thomas and Fermi approximated $F[\rho]$ of a uniform electron gas by local approximations for the kinetic energy, plus the Hartree energy. This was a rather crude but important first step in the right direction towards formulating a DFT method. The major source of error was the approximation of the kinetic energy ($10\% - 20\%$ error), which was too large for any useful predictions in chemistry calculations.[97–99]   Other sources of error included the complete neglect of electron correlation and the inaccurate description of the exchange energy.

Kohn and Sham in the 60's reconciled these issues by introducing the so-called Kohn-Sham system[92, 93] of fictitious non-interacting electrons, such that the kinetic energy, and henceforth, the electron density, can be formulated exactly. In this approach, the electron density ρ is given by a set of real, occupied orbitals

$$\rho = \sum_i |\psi_i|^2 \tag{2.3}$$

that satisfy the set of Schrödinger-like Kohn-Sham equations for each orbital,

$$-\frac{1}{2}\nabla^2 \psi_i + v_o \psi_i = \varepsilon_i \psi_i, \tag{2.4}$$

where v_o is the single-electron effective potential, ε_i is the energy of orbital i, and $-\frac{1}{2}\nabla^2$ is the kinetic energy operator. The total kinetic energy of the non-interacting system is given by

$$T_o = -\frac{1}{2}\sum_i \nabla^2 \psi_i. \tag{2.5}$$

The *Kohn-Sham wavefunction*, Φ, is the wavefunction that yields the exact $\rho(r)$, which minimizes the total kinetic energy via the Euler-Lagrange equation,

$$\frac{\delta T_o}{\delta \rho(r)} + v_o(r) = \lambda, \tag{2.6}$$

such that

$$T_o[\rho] = \min_{\Phi \to \rho} \langle \Phi | T | \Phi \rangle. \tag{2.7}$$

The ground-state functional of an interacting system can now be written as a sum of the non-interacting kinetic energy, T_o, the Hartree energy, U, and an exchange-correlation term:

$$F[\rho] = T_o[\rho] + U[\rho] + E_{\text{xc}}[\rho]. \tag{2.8}$$

The largest contribution to the total energy functional comes from the kinetic and Hartree energy (which can also be written exactly as a functional of ρ), so, the only term we need to approximate is E_{xc}. In other words, if we insert $F[\rho]$ in the Euler-Lagrange equation 2.2 and note that the right hand side is identical to that of equation 2.6, we can write an expression for the Kohn-Sham potential as

$$v_o = v_{\text{ext}} + \frac{\delta U}{\delta \rho} + \frac{\delta E_{\text{xc}}}{\delta \rho}, \tag{2.9}$$

where the functional derivative of the Hartree energy is given by

$$\frac{\delta U}{\delta \rho} = \int d\boldsymbol{r} \frac{\rho(\boldsymbol{r})}{|\boldsymbol{r} - \boldsymbol{r'}|},$$

which makes it possible to solve the Schrödinger equation in the framework of Kohn-Sham theory. Unlike the Thomas-Fermi approach, Kohn-Sham theory is applicable to various realistic systems in quantum chemistry with an acceptable level of accuracy.[100]

DFT is 100% accurate in theory, but requires approximations in practice, since we do not know the exact form of the exchange-correlation functional. Much of the research effort in DFT has therefore been towards finding ways of improving DFT approximations through better formulations of E_{xc}.[101] In the next section, we will see some of the most widely used approaches that have been developed to help deal with the errors that come from approximating the exchange-correlation functional.

2.2 Density Functionals

2.2.1 The Local Density Approximation (LDA)

The earliest approximation of the exchange-correlation energy was introduced by Kohn and Sham following their formulation of DFT. Similar to the Thomas-Fermi model, they used a uniform electron gas to model the system, where the exchange-correlation energy is evaluated using only the electron density at each point in space. This model is called the Local Density Approximation (LDA) or Local Spin-Density

Approximation (LSDA). The exchange-correlation energy functional in this model is given by

$$E_{xc}^{\text{LDA}} = \int \varepsilon_{xc}^{\text{UEG}} dr, \tag{2.10}$$

where $\varepsilon_{xc}^{\text{UEG}}[\rho]$ is the exchange-correlation energy, per unit volume, of a uniform electron gas. The exchange-correlation energy can be separated into two terms, *exchange* and *correlation*, such that

$$E_{\text{xc}} = E_{\text{x}} + E_{\text{c}}. \tag{2.11}$$

Most of the contribution to E_{xc} comes from the E_x term. Since the formulation of the correlation term is much more complicated and less relevant for our discussions, we shall focus only on the exchange term moving forward in this section. Analogous to the exchange-correlation energy, the exchange energy in the LDA is given by

$$E_{\text{x}}^{\text{LDA}} = \int \varepsilon_{\text{x}}^{\text{UEG}} dr, \tag{2.12}$$

where, $\varepsilon_x^{\text{UEG}}$, has the analytical form

$$\varepsilon_{\text{x}}^{\text{UEG}} = -\frac{3}{4} \left(\frac{3}{\pi}\right)^{1/3} \rho(r)^{4/3}. \tag{2.13}$$

Contrary to the assumption made in the LDA, the density of real chemical systems is not uniform. This results in inaccurate predictions of bond lengths, exchange and correlation energies.[102, 103] Applications have shown that the LDA underestimates exchange energies and overestimates both correlation energies and bond energies. For systems with slowly varying ρ, however, the LDA gives reasonably good predictions. Interestingly, the LDA also gives reasonable bond lengths and energies for many van der Waals systems, e.g. graphene, where treatment of long-range interactions is important. This is however not because of accurate treatment of these interactions in the LDA, but by the fortuitous cancellation of errors. A more accurate, consistent, and reliable model is therefore required.[104]

2.2.2 Generalized Gradient Approximation (GGA)

To account for the non-uniform nature of the electron density in real systems, a dependency on the gradient of the density, $\nabla\rho$, is introduced in our Density-Functional Approximation (DFA). Functionals that depend on the density as well as the gradient density are known as Generalized Gradient Approximation (GGA) functionals.[105, 106]

We can think of a GGA as a correction to the LDA, such that

$$E_{\text{x}}^{\text{GGA}} = E_{\text{x}}^{\text{LDA}} - \epsilon^{\text{GGA}}, \tag{2.14}$$

Figure 2.1: A plot of the enhancement factor versus the reduced gradient for different GGA exchange functionals.
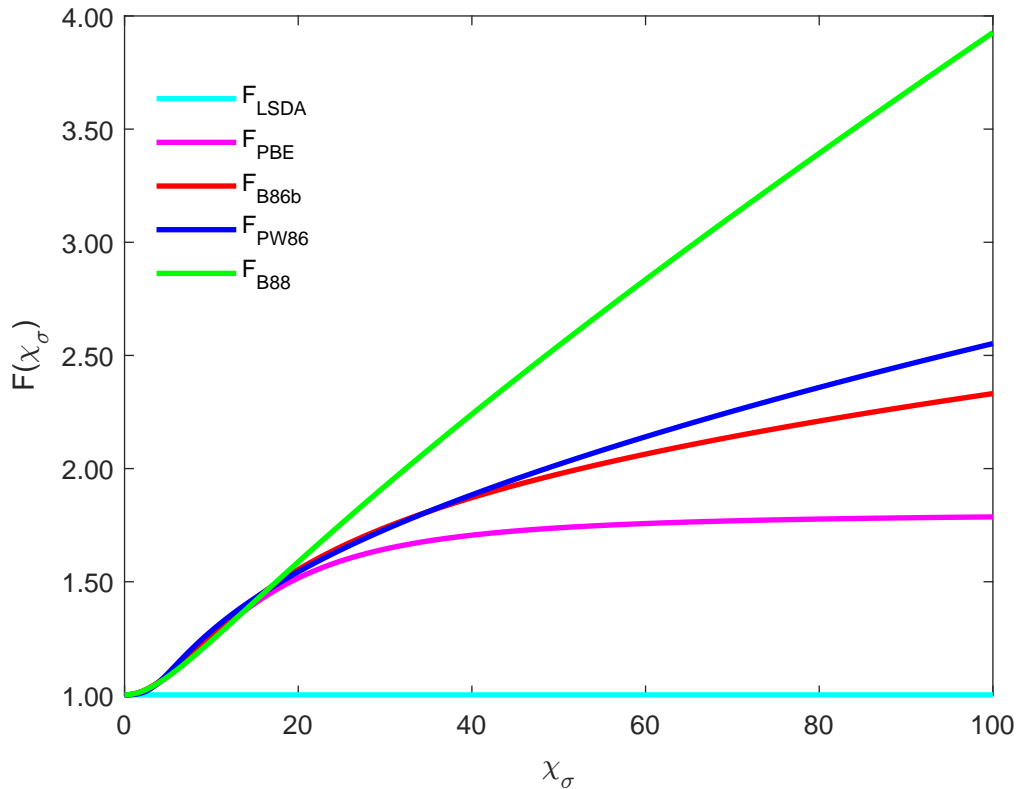
where ϵ^{GGA} is the gradient correction. It is common to write GGAs in terms of an *enhancement factor*, $F(\chi)$,

$$E_{\text{x}}^{\text{GGA}} = \int E_{\text{x}}^{\text{LDA}} F(\chi) dr, \tag{2.15}$$

where

$$\chi = \frac{|\nabla \rho|}{\rho^{4/3}}, \tag{2.16}$$

is know as the reduced or dimensionless gradient density.

The enhancement factor helps us analyze the performance of these functionals in different regions. The correct behavior of $F(\chi)$ is the zero-gradient limit to recover the LDA and in the large-gradient limit is

$$\lim_{\chi \to \infty} F(\chi) \sim \chi^{2/5} \tag{2.17}$$

to properly account for semi-local exchange repulsion.[104, 107–109] This is especially important for van der Waals materials, where covalent or ionic interactions are absent and dispersion interactions are extremely relevant.

Figure 2.1 shows the enhancement factors of selected GGA functionals. The LDA and PBE functionals[107, 110–113] underestimate the exchange energy for large reduced gradients, while B88[109] overestimates it. These functionals do not possess the correct large-gradient limit. PW86[114] and B86b,[107] on the other

hand, have the desirable asymptotic behavior required for capturing long-range non-bonded repulsion.[115]

In our work, we use the B86b exchange functional for the reasons stated above. The enhancement factor for this functional is given by

$$F(\chi) = 1 + \frac{\beta}{c_x} \frac{\chi^2}{(1 + \gamma\chi^2)^{4/5}}, \tag{2.18}$$

which clearly satisfies the large gradient limit of equation 2.17. β, γ and c_x are constants. Since the B86b functional has no correlation component, we pair it with the a PBE correlation functional. To denote that we are using the B86b functional to account for exchange and PBE to account for correlation, we write this functional as B86bPBE.

Despite the improved performance of GGAs over the LDA, these functionals still do not include the highly non-local electron correlations responsible for London dispersion. In the next section, we therefore discuss the importance of such weak interactions in chemistry and how we account for them in DFT calculations.

2.3   Accounting for Dispersion in DFT

London Dispersion Forces

Due to the constant motion of the electrons in atoms or molecules, a temporary dipole can be developed when electrons are distributed asymmetrically about the nucleus. The *London dispersion force* is an attractive force that results when the electrons in two neighboring atoms occupy positions that make the atoms or molecules form instantaneous dipoles. In the framework of DFT, instantaneous dipoles are formed between two fluctuating electron densities. Dispersion interactions exist between all molecules, whether polar or non-polar. London dispersion is the weakest intermolecular interaction and is responsible for attraction between non-polar chemical species. Although dispersion interactions are quite small in magnitude in comparison to exchange and correlation, their collective contributions play a significant role in determining various chemical and physical properties of molecular solids and surfaces, such as conditions for phase changes, adsorption, adhesion, and friction.[79, 116–118]

Various methods have been proposed over the past decade to include dispersion interactions in DFT calculations. These methods can be categorized in two groups: (i) Methods that explicitly include non-local dispersion contributions to the E_{xc} functional,[119] and (ii) methods where dispersion is calculated independently and its contribution added afterwards,[120, 121] such that

$$E_{\mathrm{DFT}} = E_{\mathrm{base}} + E_{\mathrm{disp}}, \tag{2.19}$$

where E_{base} is the functional without any explicit treatment of dispersion, and E_{disp} is a dispersion

contribution to the total energy. Methods that account for dispersion in this manner are computationally cheaper and, thus, more desirable when dealing with larger systems. Dispersion models that follow this approach are known as *post-SCF dispersion corrections.*

The dispersion energy term in equation 2.19 is given by

$$E_{\mathrm{disp}} = -\frac{1}{2} \sum_{\mathbf{L}} \sum_{i,j} \sum_{n} \frac{C_{n,ij} f(R_{ij\mathbf{L}})}{R_{ij\mathbf{L}}^{n}}, \tag{2.20}$$

where $C_{n,ij}$ are the n-th order interatomic dispersion coefficients, $f(R_{ij\mathbf{L}})$ is a damping function that prevents divergence of the dispersion interaction at short range, and

$$R_{ij\mathbf{L}} = |\mathbf{R}_i + \mathbf{R}_j + \mathbf{L}| \tag{2.21}$$

is the distance between atoms i and j in cells separated by lattice vector $\mathbf{L}$. Using perturbation theory, we can write equation 2.20 as a sum of pairwise atomic terms:

$$E_{\mathrm{disp}}^{(2)} = -\sum_{\mathbf{L}} \sum_{i<j} \left(\frac{C_{6,ij} f_6(R_{ij\mathbf{L}})}{R_{ij\mathbf{L}}^{6}} + \frac{C_{8,ij} f_8(R_{ij\mathbf{L}})}{R_{ij\mathbf{L}}^{8}} + \frac{C_{10,ij} f_{10}(R_{ij\mathbf{L}})}{R_{ij\mathbf{L}}^{10}} + ... \right). \tag{2.22}$$

In general, however, dispersion is not pairwise additive, i.e. the sum of dispersion energies of all atomic pairs in the system do not equal the dispersion energy. The largest contribution to the dispersion energy beyond the pairwise terms in equation 2.22 is the Axilrod-Teller-Muto (ATM) term,[122] which corresponds to the interaction between three dipoles:

$$E_{\mathrm{atomic}}^{(3)} = \sum_{i<j<k} \frac{C_{9,ijk} \left[3\cos(\theta_i)\cos(\theta_j)\cos(\theta_k) + 1 \right] f_9(R_{ij\mathbf{L}}), R_{jk\mathbf{L}}), R_{ki\mathbf{L}})}{R_{ij\mathbf{L}}^{3} R_{jk\mathbf{L}}^{3} R_{ki\mathbf{L}}^{3}}. \tag{2.23}$$

For virtually all calculations in chemistry, the first 3 leading pairwise terms are sufficient to give a very accurate account of dispersion, without taking into account the beyond-pairwise term. $E_{\mathrm{atomic}}^{(3)}$ is minuscule and negligible (except for very precise calculations on noble gases) compared to even the C_{10} term.[123]

Various post-SCF dispersion corrected models have been developed over the years. The commonly used ones include Grimme's series of dispersion corrections (DFT-D2, -D3, and D4),[124–126] the Tkatchenko-Scheffler model (TS-vdW)[127] and many-body (MBD) methods,[121] and the eXchange-Hole Dipole Moment (XDM) model.[85,128,129] These methods differ in how dispersion coefficients are computed, what damping functions are used, what additional parameters are added in front of the summation (in equation 2.20), to which order they are summed, i.e. C_6 (as is the case in the DFT-D2 and TS-vdW methods), C_8 (D3 and D4), C_{10} (XDM), and whether or not the ATM term is included. Electronic many-body effects are captured by equation 2.22 provided the dispersion coefficients have appropriate density dependence,

as opposed to being constants.[123] In the XDM model, electronic many-body effects are captured to all orders by constructing the dispersion coefficients from the exchange hole, which is evaluated using the interacting electron density. We use the XDM model throughout our work, which has been shown to perform consistently and accurately in calculations involving molecular crystals, metal surfaces and layered materials.[77,80,130] We shall therefore devote the next subsection to reviewing the XDM dispersion model.

2.3.1 The XDM Dispersion Model

The exchange-hole dipole moment (XDM) was developed over a series of papers[129,131–134] by Johnson and Becke to account for dispersion interactions in DFT calculations. In the XDM model, the dispersion energy and dispersion coefficients are evaluated routinely from ground-state DFT through standard quantum-chemistry codes. The XDM has been implemented in the Quantum ESPRESSO suite,[135,136] which is the utility we use throughout this work. XDM dispersion coefficients are derived from pairwise interactions between instantaneous atomic multipole moments, which originate from the distribution of electrons plus exchange-hole dipoles.

The first three terms from equation 2.22 in the XDM model are given by

$$C_{6,ij} = \frac{\alpha_i \alpha_j \langle M_1^2 \rangle_i \langle M_1^2 \rangle_j}{\langle M_1^2 \rangle_i \alpha_j + \langle M_1^2 \rangle_j \alpha_i}, \tag{2.24}$$

$$C_{8,ij} = \frac{3}{2} \frac{\alpha_i \alpha_j \left(\langle M_1^2 \rangle_i \langle M_2^2 \rangle_j + \langle M_2^2 \rangle_i \langle M_1^2 \rangle_j \right)}{\langle M_1^2 \rangle_i \alpha_j + \langle M_1^2 \rangle_j \alpha_i}, \tag{2.25}$$

$$C_{10,ij} = \frac{3}{2} \frac{\alpha_i \alpha_j \left(\langle M_1^2 \rangle_i \langle M_3^2 \rangle_j + \langle M_3^2 \rangle_i \langle M_1^2 \rangle_j \right)}{\langle M_1^2 \rangle_i \alpha_j + \langle M_1^2 \rangle_j \alpha_i} + \frac{21}{5} \frac{\alpha_i \alpha_j \langle M_2^2 \rangle_i \langle M_2^2 \rangle_j}{\langle M_1^2 \rangle_i \alpha_j + \langle M_1^2 \rangle_j \alpha_i}, \tag{2.26}$$

where $\langle M_l^2 \rangle (l = 1, 2, 3, ...)$ are the expectation values of the l-th order exchange-hole multipole moments, and α_i is the atom-in-solid polarizability of atom i. $\langle M_l^2 \rangle$ is given by

$$\langle M_l^2 \rangle = \sum_\sigma \int \omega_{H,i}(\mathbf{r}) \rho_\sigma^r(\mathbf{æ}) \left[r_i^l - (r_i - d_{X_\sigma}(\mathbf{r}))^l \right]^2 d\mathbf{r}, \tag{2.27}$$

and α_i by

$$\alpha_i = \frac{\int r^3 \omega_{H,i}(\mathbf{r}) \rho_\sigma^{ae}(\mathbf{r}) d\mathbf{r}}{\int r^3 \rho_i^{at}(\mathbf{r}) d\mathbf{r}} \alpha_i^{at}, \tag{2.28}$$

where d_{X_σ}, σ, ρ_σ^{ae} and r_i signify the exchange-hole dipole moment, spin index, all-electron spin-density, and distance from atom i, respectively. ρ_i^{at} are the reference free-atom (r.f.a) densities, while α_i^{at} are the r.f.a polarizabilities. $\omega_{H,i}$ is the weight of that atom's contribution to the spin density (or simply

electron density).

There are various schemes for partitioning the weights, e.g., the Becke scheme,[137] the Hirshfeld partitioning scheme,[138] and iterative stockholder Analysis.[139,140] Detailed discussions about each of these methods can be found in the references. In the XDM model, the Hirshfeld partitioning scheme, $\omega_{H,i}$, is used:

$$\omega_{H,i}(\mathbf{r}) = \frac{\rho_i^{at}(\mathbf{r})}{\sum_j \rho_j^{at}(\mathbf{r})}. \tag{2.29}$$

The in-solid polarizabilities α_i are computed from the ratio between the in-solid and free atomic volumes, multiplied by their *in vacuo* (r.f.a.) counterparts α_i^{at}. Equation 2.28 can therefore be written more compactly as

$$\alpha_i = \frac{V_i}{V_{i,free}} \alpha_i^{at}, \tag{2.30}$$

where V_i and $V_{i,free}$ are the in-solid and r.f.a. volumes, respectively.

The exchange-hole dipole moment d_{X_σ} from equation 2.27 is given by

$$d_{X_\sigma}(\mathbf{r}) = \int \mathbf{r}' h_{X_\sigma}(\mathbf{r}, \mathbf{r}') - \mathbf{r}, \tag{2.31}$$

where h_{X_σ} is the exchange-hole,

$$h_{X_\sigma}(\mathbf{r}, \mathbf{r}') = -\frac{1}{\rho_\sigma(\mathbf{r_1})} \sum_{i,j} \psi_{i\sigma}(\mathbf{r})\psi_{j\sigma}(\mathbf{r}')\psi_{j\sigma}(\mathbf{r})\psi_{i\sigma}(\mathbf{r}'), \tag{2.32}$$

and $\psi_{i,j}$ are the occupied KS orbitals. Computing the exact $h_{X_\sigma}(\mathbf{r}, \mathbf{r}')$ is very difficult since it involves a double sum operation over occupied states. To alleviate this difficulty, the Becke-Roussel (BR) semi-local model for the spherically averaged exchange hole is used.[132]

The BR model hole has the form of an off-centered exponential function $A\exp(-ar)$ displaced from the electron's reference point by a distance b. Three constraints are imposed on the BR model that uniquely determine three parameters A, a and b. These constraints are that the hole (i) must be normalized to -1 electron, (ii) must deplete to the spin density at the reference point, and (iii) must have the same curvature as the exact exchange hole at the reference point. Applying these constraints, the normalization constant on A gives

$$A = -\frac{a^3}{8\pi}, \tag{2.33}$$

and the spin-density constraint gives

$$\rho_\sigma = \frac{a^3}{8\pi} \exp(-ab). \tag{2.34}$$

The exact exchange hole curvature is given by

$$Q_\sigma = \frac{1}{6}\left[\nabla^2\sigma_\sigma - 2\tau_\sigma + \frac{1}{2}\frac{\nabla\rho_\sigma}{\rho_\sigma}\right], \tag{2.35}$$

where the positive-definite kinetic-energy density τ_σ is defined as

$$\tau_\sigma = \sum_i |\nabla\psi_{i,\sigma}|^2. \tag{2.36}$$

The curvature constraint is then

$$Q_\sigma = \frac{\rho_\sigma}{6b}(a^2 b - 2a). \tag{2.37}$$

The values of a and b are fixed by solving the non-linear equations that arise from inserting the spin-density Equation 2.34 into Equation 2.35 and making the change of variable $x = ab$:

$$\frac{x\exp(-2x/3)}{x-2} = \frac{2}{3}\pi^{2/3}\frac{\rho_\sigma^{5/3}}{Q_\sigma}. \tag{2.38}$$

This non-linear equation is solved numerically for x using the Newton-Raphson method. b is calculated as

$$b^3 = \frac{x^3\exp(-x)}{8\pi\rho_\sigma}, \tag{2.39}$$

with an additional constraint to replace b with r if $b > r$. This is done in order to exclude non-physical values of the exchange-hole dipole moment, $d_{X_\sigma} = b$.

The final component to completing the XDM model is the choice of damping function.[131] The Becke-Johnson damping function used in XDM has the form

$$f(R_{ij\mathbf{L}}) = \frac{R_{ij\mathbf{L}}}{R_{\text{vdW},ij}^n + R_{ij\mathbf{L}}} \tag{2.40}$$

where

$$R_{\text{vdW},ij}^n + R_{ij} = a_1 R_{c,ij} + a_2, \tag{2.41}$$

and

$$R_{c,ij} = \frac{1}{3}\left[\left(\frac{C_{8,ij}}{C_{6,ij}}\right)^{1/2} + \left(\frac{C_{10,ij}}{C_{6,ij}}\right)^{1/4} + \left(\frac{C_{10,ij}}{C_{8,ij}}\right)^{1/2}\right]. \tag{2.42}$$

The critical radius, $R_{c,ij}$, is constructed from the ratios of the first three leading-order pairwise disper-

sion coefficients, $C_{6,ij}$, $C_{8,ij}$, and $C_{10,ij}$. The parameters a_1 and a_2 are obtained semi-empirically by minimizing the residual errors between computed and reference binding energies for a benchmark set (the Kannemann-Becke set) of non-covalently bound dimers.[141] These parameters vary depending on the functional being used and serve to match the long-range dispersion and short-range exchange-correlation contributions.

There are various types of calculations that we can perform with standard DFT codes, including self-consistent field (SCF) calculations and geometry optimizations.[84] In this work, we model the PES by performing a geometry optimization at different relative sliding position. The goal of a geometry optimization is to obtain a local minimum. The initial geometry of the structure is optimized iteratively through multiple sets of SCFs until the force acting on each atom is zero. The dispersion contribution to the atomic forces for an atom i is given by

$$F_{\text{disp},i} = \sum_{\mathbf{L}} \sum_j \sum_n \frac{nC_{n,ij}R_{ij\mathbf{L}}^{n-2}}{(R_{vdW,ij}^n + R_{ij\mathbf{L}}^n)^2} R_{ij\mathbf{L}}. \tag{2.43}$$

Note that the dispersion coefficients in these expressions are assumed constant when evaluating the forces throughout the geometry optimization. This is not strictly correct because any small change in the geometry would result in a different electron density and, hence, different dispersion coefficients. However, keeping the dispersion coefficients fixed in the manner described above has been shown to have negligible effects on accuracy of the total energy. The XDM model has been implemented in quantum ESPRESSO (the utility we use in this work) in this manner.

2.4 DFT for Periodic Solids

When treating periodic systems such as crystalline solids, we can subvert the realistic but intractable (and unnecessary) approach of considering the entire bulk material and using an effectively infinite number of orbitals to describe the states of all the electrons in the system. Periodic solids can be truncated into repeating unit cells, such that we need only to define specifically the position of the atoms in a unit cell. We can picture the atoms as being enclosed in a volume defined by the Bravais lattice vectors

$$\mathbf{R} = \sum_{i=1}^{3} n_i \mathbf{a}_i, \tag{2.44}$$

which can be translated along the 3 spatial directions $\mathbf{a}_i$. n is an integer representing the number of lattice translations and $i = 1, 2, 3$. Exploiting further the premise of periodicity in this formulation, the potential, $u(\mathbf{r})$, felt by an electron at an arbitrary point, $\mathbf{r}$, in a unit cell is given by

$$u(\mathbf{r}) = u(\mathbf{r} + \mathbf{R}). \tag{2.45}$$

Since the potential 2.45 is periodic, we can describe the wave function of the crystal using plane waves and invoking Bloch's theorem.[142]

2.4.1 Plane Waves and Bloch's Theorem

A *plane wave* propagated in the direction $\mathbf{k}$ is a wave whose value is defined on every plane orthogonal to the direction of propagation. A simple plane wave can be written as a complex exponential function,

$$\mathbf{F}_{\mathbf{k}}(\mathbf{r}) = \exp(i\mathbf{k} \cdot \mathbf{r}). \tag{2.46}$$

Bloch's theorem states that the electronic wave function, $\psi_{\mathbf{k}}(\mathbf{r})$, can be written as a product of a plane wave and a periodic potential, i.e.,

$$\psi_{\mathbf{k}}(\mathbf{r}) = \mathbf{F}_{\mathbf{k}}(\mathbf{r})u(\mathbf{r}). \tag{2.47}$$

Since $u(\mathbf{r})$ is periodic, and $\mathbf{k}$ lies within the reciprocal space unit cell, we can take its discrete Fourier transform,

$$u(\mathbf{r}) = \sum_{\mathbf{G}} c_{\mathbf{G}} \exp(i\mathbf{G} \cdot \mathbf{r}), \tag{2.48}$$

and substitute it in equation 2.47 to obtain the general form of the crystal's wave function,

$$\psi_{\mathbf{k}}(\mathbf{r}) = \mathbf{F}_{\mathbf{k}}(\mathbf{r}) \sum_{\mathbf{G}} c_{\mathbf{G}} \exp(i\mathbf{G} \cdot \mathbf{r}), \tag{2.49}$$

where $c_{\mathbf{G}}$ are the Fourier coefficients, and $\mathbf{G}$ is the reciprocal lattice vector. Note that all states corresponding to $\mathbf{k}$ and any $\mathbf{k} + \mathbf{G}$ are equal, such that $\psi_{\mathbf{k}}(\mathbf{r})$ is periodic in reciprocal space. The wave functions can therefore be any plane wave of momentum $\mathbf{k} + \mathbf{G}$. Further, the periodic potential must have the periodicity of the Bravais lattice. In order to satisfy this requirement, $\mathbf{G} \cdot \mathbf{R} = 2\pi m$, where m is an integer. The coefficients $c_{\mathbf{G}}$ are obtained by inserting $\psi_{\mathbf{k}}(\mathbf{r})$ in the Schrödinger equation. The energy levels of the electrons are then defined by $\mathbf{k}$-vectors.

2.4.2 K-point Sampling

In order to capture all the important electronic properties of the crystal, sampling an infinite number of vectors is not only impossible but also not required. In practice, we only need a minimal set of $\mathbf{k}$ vectors to accurately sample the space. A sample of $\mathbf{k}$-points within a crystal is known as a $\mathbf{k}$-point grid. It is important to create an efficient $\mathbf{k}$-point grid that is 1) properly positioned (not biased in any direction) such that it will not miss any vital points in the Brillouin zone, and 2) dense enough that it will not omit any vital information about the system and result in inaccurate results.

In this work, we use the Monkhorst-Pack (MP)[143][143] **k**-point grid system implemented in the quantum ESPRESSO package, which provides an efficient way to address the issues stated above. In MP grids, a set of **k**-vectors is established by producing an equally-spaced mesh of points in each of the three dimensions of the cell in **k**-space. The notation used to specify the number of points along each direction is $i \times j \times k$, where i, j and k are positive integers.

When using planewave methods, we can limit the number of wave functions included in the basis set. This can be done systematically in standard DFT codes by setting kinetic-energy cutoffs for the electron density and wavefunction. It is important to perform convergence tests on the electron density and kinetic energy cutoffs, as well as **k**-points, so that we can run the DFT code in the cheapest way possible, i.e., with the lowest possible cutoffs and least number of **k**-points without compromising the accuracy.

Using a plane-wave basis set becomes problematic for solid-state calculations because of the rapidly oscillating behaviour of the wavefunction near the nuclei, in comparison to the valence regions. As a result, calculations can require a very large number of plane waves to achieve convergence and correctly capture the orthogonality of valence orbitals to the core orbitals. This problem can be alleviated by using atomic pseudopotentials.

2.4.3 Atomic Pseudopotentials

A pseudopotential allows replacement of the highly oscillatory core-electron wave functions with a smoother potential. A pseudopotential divides an atom into the valence and core regions. Core-electron wave functions are fixed since they do not participate in chemical processes such as bonding or adsorption. They are therefore incorporated into an atomic valence wave function as an effective potential. The valence electron wave function then becomes the effective atomic wave function. Each pseudopotential is characterized by a core radius that originates at the nucleus and terminates at the boundary of the core and valence regions.

Many types of pseudopotentials have been developed, with the two main types being norm-conserving and ultrasoft.[144, 145] Pseudopotentials are generated using DFT codes in packages such as SIESTA, Quantum ESPRESSO, VASP, Open-source Pseudopotential Interface/Unification Module (OPIUM), and several others. Pseudopotentials are generated for a specific atom on the periodic table and are specific to the type of exchange-correlation functional being used. Although there exist numerous codes and packages for generating pseudopotentials, the procedure for generating efficient pseudopotentials is the same. 1) Generate atomic levels and orbitals with DFT code. 2) From the atomic results, generate the pseudopotential using the DFT package/code of choice. 3) Check whether the resulting pseudopotential is working properly, and whether it is transferable, i.e. can be used for different systems. If not, steps 2 and 3 must be repeated. There are several parameters that one can adjust in order to improve a

pseudopotential. In the Quantum ESPRESSO suite, pseudopotentials are generated using the `atomic` program, `ld1.x`. The parameters to be adjusted include the valence-core partition, electronic reference configuration, non-linear core correction, type of pseudization, pseudization energies, pseudization radii, and local potential. A detailed description of each of these parameters of the procedure used to generate pseudopotentials can be found in Ref 146. The essence is that these parameters determine which electrons are included in the core-electron basis set and which are omitted. The proper utilization of the pseudopotential method ultimately leads to a reduction of computational time without sacrificing the accuracy.

2.4.4   The Projector-Augmented Wave (PAW) Method

The Projector-Augmented Wave (PAW) method, developed by Blöchl,[147] and further generalized by Kresse and Joubert,[148] is a combination of the pseudopotential method and plane-wave DFT. It is based on the concept from Slater's augmented plane-wave (APW) method,[149] where a linear combination of plane waves and pseudopotentials is used to treat the valence electrons of a solid-state system, and the total wave function of the crystal partitioned into *intra-* and *inter-*atomic regions. In the PAW method, the intra-atomic region is described using radial functions and spherical harmonics, whereas the inter-atomic continuum is modelled with plane waves. Replacing the rapid oscillatory plane waves near the nuclei with radial functions has the benefit of reducing the computational cost. Another advantage of the PAW method is that the core wave functions are not completely omitted, as in other pseudopotential methods, but can be retained using linear transformations. These wavefunctions are important when describing chemical properties that require both core and valence electrons.

The all-electron wave function can be reconstructed from a smooth pseudo wave function, ψ_{ps}, using a linear transformation, $\hat{T}$, such that

$$|\psi_{\text{real}}\rangle = \hat{T} |\psi_{\text{ps}}\rangle, \tag{2.50}$$

where

$$\hat{T} = 1 + \sum_{i}^{N} (|\phi_{\text{real},i}\rangle - |\phi_{\text{ps},i}\rangle) \langle p_i|, \tag{2.51}$$

and $\langle p_i|$ is the projection function that projects the pseudo wave function onto the all-electron wave function. The PAW method is one of the most reliable and widely used plane-wave methods in DFT, and is the method employed in this work.

2.5 Moiré Pattern Theory

Moiré patterns can be understood as large-scale interference patterns produced by superimposing two periodic structures on top of each other. The resulting structure, referred to as a Moiré structure, is also periodic (or quasi-periodic). Moiré structures have recently garnered attention from researchers in the solid-state physics and tribology communities. Much focus has been placed on the electronic and physical properties of Moiré structures following the detection of Moiré patterns in Twisted Bilayer Graphene (TBLG) using the Scanning Tunnelling Microscopy (STM).[150, 151] Further studies suggest that these structures possess peculiar electronic and physical properties such as superconductivity and super-lubricity (ultra-low friction) and, therefore, have the potential to revolutionize both electronics[152–154] and tribology.[19, 28, 155, 156] Our interest in this work is in the latter.

Moiré patterns have also been observed when graphene adsorbs on the surfaces of metals[157] and on two-dimensional (2D) materials such as hexagonal boron nitride[158] and molybdenum disulfide.[27] In order to study Moiré structures analytically, mathematical descriptions have been developed.[81] Although, in principle, it is possible to create Moiré patterns for two overlapping structures of any Bravais lattice type, Moiré patterns have only been observed in hexagonal Bravais lattices. We shall therefore focus on discussing Moiré pattern theory of two superimposed hexagonal lattices, for which experimental data is available.

2.5.1 Bilayer Crystal Structures

Bilayer crystals are 2D structures that are comprised of a *substrate* (bottom) and an *overlayer* (top), stacked atop each other and held together by van der Waals forces. As we have discussed in earlier sections of this chapter, dispersion should be appropriately incorporated in our DFT methods, especially for layered materials where covalent and ionic bonds are absent between vertically adjacent layers. In this case, long-range interactions are extremely important. These materials are essential to experimental, theoretical, and computational studies of friction and electronic properties of solids.

The periodic and spatial properties of the substrate and overlayer can be represented in Wood's notation[159] by $(p_1 \times p_2)R\alpha$, where $p_1 = a_o/a_s$, $p_2 = b_o/b_s$, and α is the angle of rotation of the overlayer lattice vectors with respect to those of the substrate. (a_o, b_o) and (a_s, b_s) are the lattice vectors of the overlayer and substrate, respectively.

2.5.2 Moirons and Moiré Parameters

When two hexagonal lattices overlap, the Moiré interference patterns created are characterized by the formation of regions with periodic spaces called *moirons*. Fictitious lattice vectors can be created from these quasi-periodic moirons, as shown in Figure 2.1. The Moiré vectors are referred to as fictitious due

Table 2.1: Moiré patterns formed by rotation of the overlayer. The black arrows show the fictitious Moiré lattice vectors that span from one moiron to the other. In TBLG, h-BN, and blue phosphorene, a relative rotation of 13.17° will result in a unit cell with 76 atoms.

Moiré vectors	Unit cell
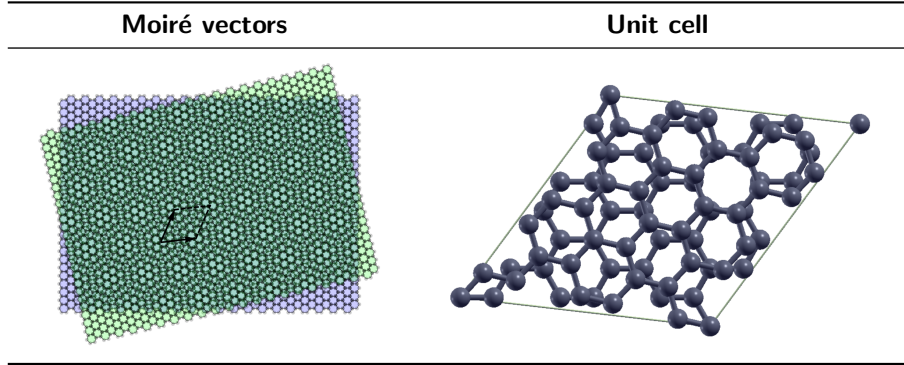
to the fact that moirons are not exactly periodic.[81] The geometrical detail of the structure of Moiré surfaces is very complex. Mathematical approximations using Fourier transforms have been developed to describe the visual periodicity of Moiré structures. The moirons can be understood as long-range modulations in the Fourier series that describe the spatial and structural properties of the bilayer.

In order to properly quantify the geometrical properties and periodicity of moirons separated by Moiré vectors, a set of parameters is defined in Moiré pattern theory. This includes the fictitious Moiré vectors themselves, and Moiré factors and angles. A general description of each of them is given below.

Moiré Vectors

The Moiré vectors, a_m and b_m, are related to the lattice vectors of the substrate, (a_s, b_s), by a linear transformation P, such that[81]

$$\begin{pmatrix} a_m \\ b_m \end{pmatrix} = P \cdot \begin{pmatrix} a_s \\ b_s \end{pmatrix}, \tag{2.52}$$

where

$$P = \frac{1}{\Delta \sin(\gamma)} \cdot \begin{pmatrix} p_1[\sin(\gamma - \varphi) - p_2 \sin(\gamma)] & q\, p_1 \sin(\varphi) \\ -\frac{1}{q} p_2 \sin(\varphi) & p_2[\sin(\gamma + \varphi) - p_1 \sin(\gamma)] \end{pmatrix}, \tag{2.53}$$

$$\Delta = 1 + p_1 + p_2 - (p_1 + p_2)\cos(\varphi) + (p_1 - p_2)\cot(\gamma)\sin(\varphi), \tag{2.54}$$

and

$$q = \frac{a_s}{b_s}. \tag{2.55}$$

Figure 2.2 shows the relationship between the Moiré vectors and lattice vectors. For a hexagonal Bravais lattice, γ takes values 60° or 120° and $q = 1$. The angle φ is the relative rotation angle between the lattice vectors of the substrate and the Moiré lattice vectors.

Figure 2.2: Relationship of Moiré vectors with vectors of the substrate and overlayer. Note the a_o, b_o are lattice vectors for the overlayer, a_s, b_s are for the substrate, and a_m, b_m are the Moiré vectors. φ and θ are the angles between a Moiré vector and the corresponding substrate and overlayer lattice vectors, respectively.
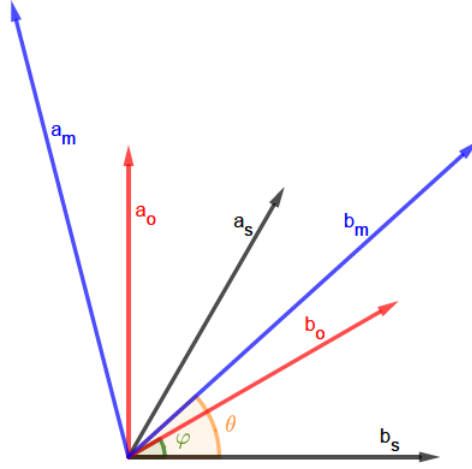
Moiré Factors and Moiré Angles

The size of moirons is characterized by the Moiré factors, (κ_1, κ_2), and Moiré angles, (θ_1, θ_2). The Moiré factors determine the visibility and detectability of Moiré patterns and are given by the expressions[81]

$$\kappa_1 = \frac{a_m}{a_s} = \frac{p_1}{\Delta}\sqrt{1 + p_2^2 - 2p_2\cos(\varphi)}, \tag{2.56}$$

$$\kappa_2 = \frac{b_m}{b_s} = \frac{p_2}{\Delta}\sqrt{1 + p_1^2 - 2p_1\cos(\varphi)}, \tag{2.57}$$

where large values of the Moiré factors signify larger and more visible moirons.

The Moiré angles can be obtained from[81]

$$\tan(\theta_1) = \frac{\sin(\varphi)}{\cos(\varphi) - p_2} \tag{2.58}$$

and

$$\tan(\theta_2) = \frac{\sin(\varphi)}{\cos(\varphi) - p_1}. \tag{2.59}$$

θ_1 and θ_2 refer to the angles $a_s \angle a_m$ and $b_s \angle b_m$, respectively. Note that for a hexagonal lattice, $\theta_1 = \theta_2$, which we denote simply as θ in Figure 2.2 and onwards in this work. For hexagonal Bravais lattices, θ, φ, and γ are connected through the relation

$$\theta = \gamma - \varphi. \tag{2.60}$$

By varying the Moiré parameters, we obtain moirons of different sizes and, therefore, can create

various sizes of Moiré unit cells. This approach to split Moiré structures into smaller fragments bounded by the fictitious Moiré lattice vectors permits us to study such systems using DFT. The number of atoms in each Moiré unit cell is influenced by the Moiré parameters we choose and the scaling factors $(p_1 \times p_2)$.

Moiré patterns have been observed in homogeneous structures as well as heterostructures.[51, 152, 157, 160] Below, we discuss the necessary ingredients and parameters for obtaining Moiré patterns in homogeneous and heterogeneous structures. We shall immediately note that, in both cases, the substrate and the overlayer must be of the same Bravais lattice type.

2.5.3 Rotated Homogeneous Structures

From the general formalism of Wood's notation, let us set $p_1 = p_2 = 1$ and examine Moiré patterns formed in such a system. The only way to obtain Moiré patterns in this scenario is by varying φ. Accordingly, the Moiré lattice vectors of the structure $(1 \times 1)R\varphi$ will be defined by equation 2.52. The linear transformation Equation 2.53 will take the form

$$P = \frac{1}{\Delta_{11}\sin(\gamma)} \cdot \begin{pmatrix} \sin(\gamma - \varphi) - \sin(\gamma) & q\sin(\varphi) \\ -\frac{1}{q}\sin(\varphi) & \sin(\gamma + \varphi) - \sin(\gamma) \end{pmatrix}, \tag{2.61}$$

where $\Delta_{11} = \Delta(p_1 = 1, \ p_2 = 1) = 1 - \cos(\varphi)$, and the Moiré parameters are given by

$$\kappa = \left(2\left|\sin\frac{\varphi}{2}\right|\right)^{-1}, \tag{2.62}$$

$$\theta = 90° + \frac{\varphi}{2}. \tag{2.63}$$

The Moiré lattice vectors a_m and b_m are stretched and rotated equally in comparison to a_s and b_s; therefore, the resulting unit cell will always be of the same Bravais lattice type as the substrate. The relation 2.63 shows that vectors a_m and b_m will, in general, not point along the directions of a_s and b_s.

Moiré patterns obtained from rotated $(1 \times 1)R\varphi$ overlayers will be clearly detectable only for κ values above a minimum threshold, $\kappa_{\min}$, where moirons are large enough to be visually distinguishable. In theoretical calculations, this threshold corresponds to structures with very large unit cells with thousands of atoms, and Moiré angles in the limits 90°, 120°, 180°, and so forth. Due to the computational cost of DFT, however, our calculations are limited to only a few hundred atoms. Table 2.2 shows the Moiré parameters and rotation angles used for some of the materials studied in this work.

Table 2.2: The lattice constant a_o, relative rotation angles φ, Moiré factors κ, and Moiré angles θ used in this work for TBLG, h-BN, MoS$_2$ and blue phosphorene. Notice how the Moiré parameters remain the same for different lattice constants. This indicates that the occurrence and periodicity of Moiré patterns is independent of the material. The important feature in creating Moiré patterns is the Bravais lattice type of the surface.

Material	a_s (Å)	φ (degrees)	a_m (Å)	θ (degrees)	κ (Å)
TBLG	2.47	21.79	6.50	100.89	2.65
		32.20	8.86	106.10	3.61
		13.17	10.71	96.59	4.36
h-BN	2.51	21.79	6.65	100.89	2.65
		32.20	9.06	106.10	3.61
		13.17	10.95	96.59	4.36
MoS$_2$	3.15	21.79	8.33	100.89	2.65
		32.20	11.36	106.10	3.61
		13.17	13.73	96.59	4.36
b-P	3.33	21.79	8.81	100.89	2.65
		32.20	12.01	106.10	3.61
		13.17	14.52	96.10	4.36

2.5.4 Unrotated Heterostructures

Apart from rotated systems, Moiré patterns can be seen in heterostructures where the lengths of the lattice constants of the constituent materials of the heterostructure are very close. The small mismatch in the lattice constants creates commensurate Moiré interference patterns, for example, when graphene adsorbs on the surfaces of metals such as Cu, Pt, Ir, and Ru.[34, 76, 151, 161, 162] In Wood's notation, these systems correspond to isotropically scaled $(p \times p)$ structures, i.e. $\varphi = 0°$. The linear transformation 2.53 will then simplify to

$$P = \frac{p}{1-p} \cdot \begin{pmatrix} 1 & 0 \\ 0 & 1 \end{pmatrix}, \tag{2.64}$$

and the Moiré parameters are given by

$$\kappa = \frac{p}{|1-p|}, \tag{2.65}$$

$$\theta \approx \begin{cases} 0° & \text{for } p < 1 \\ 180° & \text{for } p > 1. \end{cases} \tag{2.66}$$

2.5.5 Rotated Heterostructures

Lastly, Moiré patterns can can be formed in rotated isotropically scaled heterostructures $(p \times p)R\varphi$. The linear transformation 2.53 in such systems is given by[81]

$$P = \frac{p}{\Delta_{pp}\sin(\gamma)} \cdot \begin{pmatrix} \sin(\gamma - \varphi) - p\sin(\gamma) & q\sin(\varphi) \\ -\frac{1}{q}\sin(\varphi) & \sin(\gamma + \varphi) - p\sin(\gamma) \end{pmatrix}, \tag{2.67}$$

where $\Delta_{pp} = \Delta(p_1 = p, \ p_2 = p) = 1 + p^2 - 2p\cos(\varphi)$, and the Moiré parameters have the form

$$\kappa = \frac{p}{\sqrt{1 + p^2 - 2p\cos(\varphi)}}, \tag{2.68}$$

$$\tan(\theta) = \frac{\sin(\varphi)}{\cos(\alpha) - p}. \tag{2.69}$$

For small rotation angles, the Moiré parameters can be approximated by the relations[81]

$$\kappa \approx \frac{p}{\sqrt{(1 - p)^2 + p\varphi^2}} \tag{2.70}$$

and

$$\theta \approx \begin{cases} \frac{\varphi}{1-p} & \text{for } p < 1 \\[2mm] \frac{\varphi}{p-1} & \text{for } p > 1. \end{cases} \tag{2.71}$$

From the mathematical formalism of Moiré pattern theory, it is clear that DFT can be applied in the modelling of real systems provided we choose appropriate sets of Moiré parameters, such that the resulting structures are: 1) computationally tractable by size, i.e. have a reasonable number of atoms in the unit cell, and 2) satisfy the periodic boundary conditions in DFT codes. In our work, we have addressed both of these issues using an algorithm that we discuss in the next chapter.

Chapter 3

BiCrystal: Creating Moiré Unit Cells for Planewave Density-Functional Theory Codes

In this chapter, we discuss our procedure for creating Moiré unit cells of bilayer materials. We shall devote the first half of our discussion to an explanation of the main ideas of our algorithm. In the second part of this chapter, we discuss the implementation of this algorithm in Python 3. Lastly, we shall walk the reader through the download, installation, and usage of our `BiCrystal` program.

Our discussion in this section is limited to the latest version of `BiCrystal` as of the time of writing this chapter. Any *post-factum* changes have therefore not been included. This version (v1.0.7) reads CIF files and writes the new structure to a Quantum ESPRESSO input file. The program also provides additional information such as the bond distance between atoms, lattice vectors in Bohr and Ångstrom, and a simple 3D plot of each layer.

3.1 Algorithm

A wide variety of quantum chemistry and solid-state physics visualization software exists today. Although most of these packages provide very powerful tools for analyzing, visualizing, and manipulating periodic crystal structures, constructing Moiré unit cells of bilayer materials can be very daunting. It is surely possible to use a visualization tool such as XCrysDen, replicate the primitive cell multiple times in the x and y directions, extract the atomic positions of the bottom and top layer, apply a rotation matrix to one layer, and finally write the new coordinates to a new input file. There are three main challenges associated with this approach: 1) picking the correct atoms from the bilayer is often very difficult or impractical to do by hand; 2) since most solid-state codes require the atomic positions to be in crystal coordinates, it can be hard to keep track of coordinate system conversions and rotation matrix manipulations; 3) if the selection of atoms, coordinate system conversions, and rotation are not done systematically and

Figure 3.1: 1×1 AB-stacked structure of bilayer graphene showing the selected initial atom.

(a) AB-stacked graphene

(b) Selected initial atom A

consistently, an accumulation of errors is very likely. These three points have in fact been the primary motivation for the development of such an algorithm and, subsequently, the `BiCrystal` code.

Our algorithm consists of 8 steps. Below, we discuss the main concepts behind each of them. We demonstrate these ideas starting from an AB-stacked structure of graphene. The same steps apply for any bilayer material with a hexagonal bravais lattice.

3.1.1 Step 1: Reading the Initial Structure

The first step in our algorithm is to read the given structure. The crystallographic file for the AB-stacked structure of bilayer graphene shown in figure 3.1a can be obtained from standard crystallographic databases.[163]

3.1.2 Step 2: Selecting the Initial Atoms

Next, we select an initial atom in the bottom and top layers. Let us call these atoms A_{bottom} and A_{top}, respectively. In figure 3.1b, we show only the top atom selected, which we denote by A. Ideally, the initial atoms should be on one of the vertices of the unit cell. Although this is not a requirement (in principle, we could select any atom to be an initial atom), it does help us illustrate the operations of this algorithm.

3.1.3 Step 3: Replicating the Unit Cell

After selecting the initial atoms, we need to replicate the unit cell multiple times in the x and y directions, starting from the chosen initial atom. Figure 3.2 shows a 9×9 supercell replicated from the unit cell. We do this for the bottom and top layers.

3.1.4 Step 4: Defining the Boundaries of the New Unit Cell

From Moiré pattern theory as described in Section 2.5, we understand that it is possible to achieve periodic Moiré structures in homogeneous bilayers by rotating the top layer at specific angles φ.[13, 19, 28, 155] Different rotation angles result in unit cells of various sizes. The various cell vectors obtained for different rotation angles correspond to the Moiré vectors discussed in Section 2.5.2 of this work.

Figure 3.2: 9×9 supercell of the AB-stacked structure of bilayer graphene.
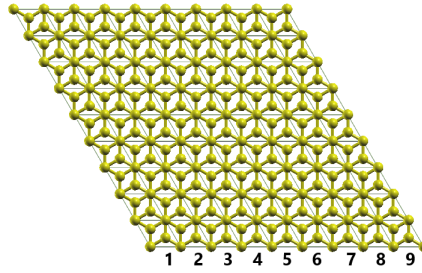
There are numerous parameters and definitions of parameters that we need to keep track of in Moiré pattern theory. Although the fundamental interpretation reviewed in Section 2.5 is necessary for the purpose of gaining a theoretical understanding of Moiré patterns, it is not a suitable scheme to implement in a computer program due to the number of parameters and variables involved. For convenience, we shall shall introduce two new parameters, m and n, that will effectively summarize all the Moiré parameters and the parameters in Wood's notation discussed in section 2.5.

Given parameters (m, n), we can define the rotation angle for a hexagonal lattice[83, 164] using

$$\cos(\varphi) = \frac{m^2 + 4mn + n^2}{2(n^2 + mn + m^2)}, \tag{3.1}$$

and calculate the cell vectors of the resulting Moiré unit cell by

$$\mathbf{a_m} = |\overrightarrow{\boldsymbol{AB}}| = m\mathbf{a_o} + n\mathbf{b_o} \tag{3.2}$$

and

$$\mathbf{b_m} = |\overrightarrow{\boldsymbol{AB}}| = -n\mathbf{a_o} + (m + n)\mathbf{b_o}, \tag{3.3}$$

where $\overrightarrow{\boldsymbol{AB}}$ is the vector from atom A to atom B as shown in Figure 3.3, m and n are positive integers with $n > m$, and $\mathbf{a_o}$ and $\mathbf{b_o}$ are the lattice vectors of the top layer (overlayer). Note that the same equations apply for the bottom layer. We only need to substitute $\mathbf{a_o}$ and $\mathbf{b_o}$ with the lattice vectors of the bottom layer (substrate) $\mathbf{a_s}$ and $\mathbf{b_s}$, respectively. For homogeneous bilayers, $|\mathbf{a_s}| = |\mathbf{a_o}|$, $|\mathbf{b_s}| = |\mathbf{b_o}|$, and in all cases $|\mathbf{a_m}| = |\mathbf{b_m}|$. Figure 3.3 shows the selected atoms X and B from initial position A when $m = 2$ and $n = 1$. To obtain the location of X, we move 2 ($m = 2$) lattice spacings to the right from A. B is then 1 lattice spacing ($n = 1$) in the y direction, such that the angle between vector $\overrightarrow{\boldsymbol{AB}}$ and $\overrightarrow{\boldsymbol{AB}}$ is 120° (see Figure 3.3).

Having obtained the vectors of the new unit cell, we can complete the unit cell by identifying the remaining vertices C and D. This is a simple task to do using linear algebra since the new cell has the same hexagonal symmetry as the initial unit cell. Table 3.1 shows unit cells constructed for different combinations of (m, n).

Figure 3.3: Defining the boundaries of the new unit cell using m,n parameters. In the case shown, $m = 2$ and $n = 1$.
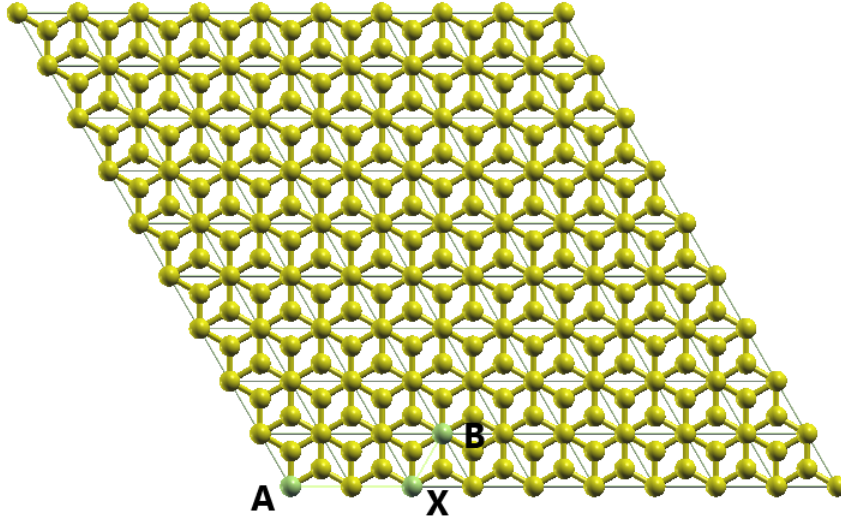
3.1.5   Step 5: Selecting Substrate and Overlayer Atoms

After defining the boundaries of the unit cell, we need to identify which atoms are in the substrate (bottom layer) and overlayer (top layer). This is straightforward and easy to automate by using the z-component of the atomic coordinates.

3.1.6   Step 6: Rotating Overlayer Atoms

It is important to convert all atomic positions to Cartesian coordinates and determine φ in degrees (Equation 3.1) before applying the rotation matrix. Note that rotation is done with respect to an origin position known as the *axis of rotation*. The conversions from crystal coordinates to Cartesian is as follows:

$$A_{\text{crystal}} = A_{\text{cartesian}} \cdot U^{-1}_{\text{cartesian}}, \tag{3.4}$$

where U is the unit cell matrix and U^{-1} is its inverse.

We first shift the vertices of the unit cell in accordance with the axis of rotation, i.e.

$$v_{i,\text{new}} = v_{i,\text{old}} - U_{\text{origin}} \tag{3.5}$$

where $i = \{1, 2, 3, 4\}$, U_{origin} is the axis of rotation, and $v_{i,\text{new}}$ and $v_{i,\text{old}}$ are the shifted and unperturbed vertices of the unit cell, respectively. We choose the center of the unit cell as the axis of rotation.

Table 3.1: Defining boundaries of the new unit cells from (m, n) combinations of $(2, 1)$, $(3, 1)$, and $(3, 2)$.

Selected (2,1)

Selected (3,1)
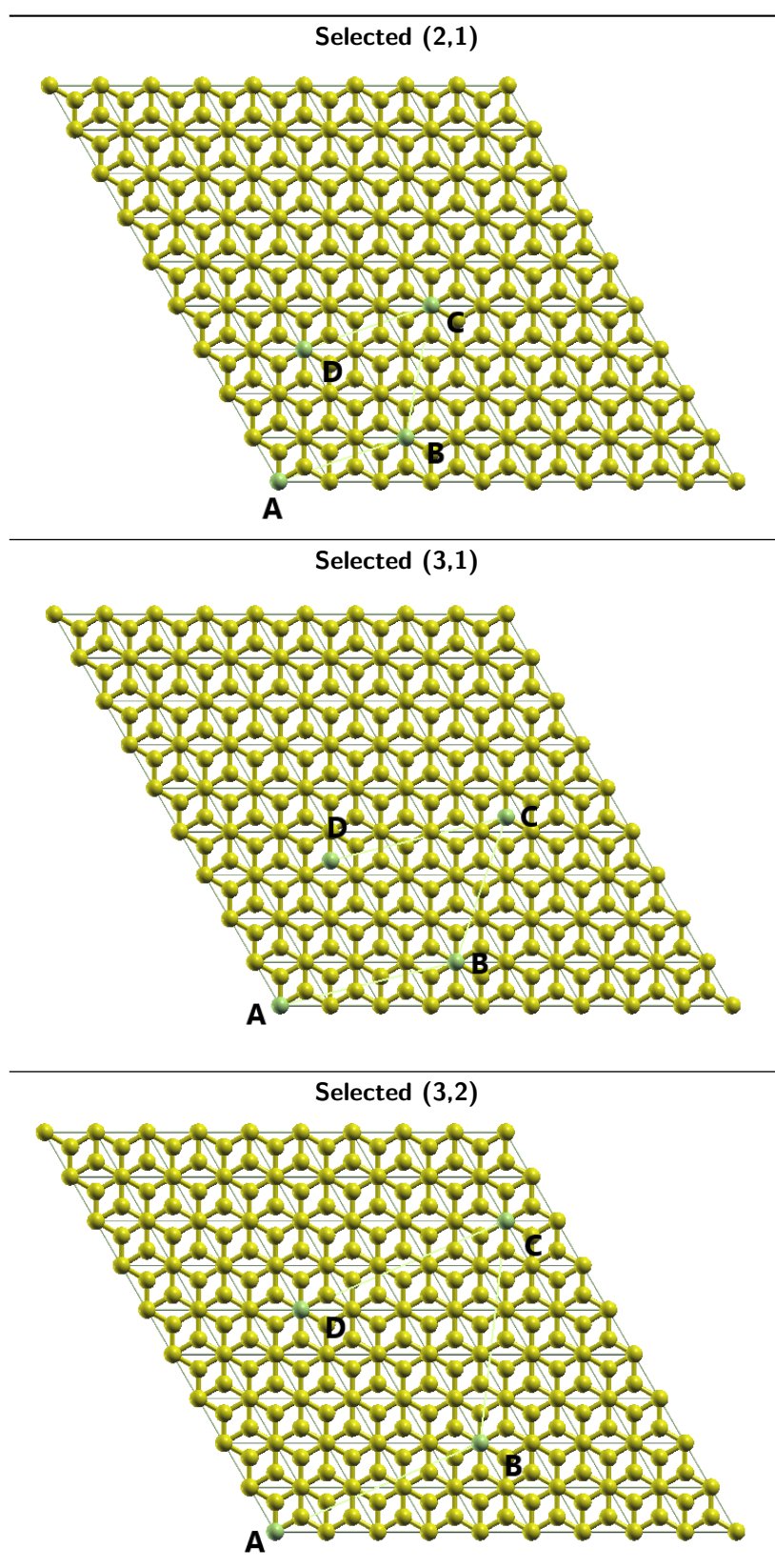
Selected (3,2)

Table 3.2: The relationships between the rotation angle, number of atoms in the unit cell, and the parameters (m, n) for Moiré unit cells of selected materials.

Material	(m, n)	φ (degrees)	Number of atoms (Å)
TBLG	$(2, 1)$	21.79	28
h-BN	$(3, 1)$	32.20	52
Phosphorene	$(3, 2)$	13.17	76
MoS_2	$(2, 1)$	21.79	42
	$(3, 1)$	32.20	78
	$(3, 2)$	13.17	114

Finally, we apply the rotation matrix

$$R_\varphi = \begin{pmatrix} \cos(\varphi) & -\sin(\varphi) \\ \sin(\varphi) & \cos(\varphi) \end{pmatrix} \tag{3.6}$$

to the coordinates of each atom A_i in the overlayer.

3.1.7 Step 7: Eliminating Symmetry-Equivalences and Restoring Missing Atoms

Rotation will often result in some of the overlayer atoms falling outside the fixed unit cell. To overcome these issues, 1) all atoms that may fall outside the unit cell must be tracked and mapped back to the unit cell in order to obtain a complete structure and 2) all symmetrically equivalent atoms (duplicate atomic positions) must be eliminated.

Eliminating symmetry-equivalent atoms is achieved by converting all atomic positions from Cartesian to crystal coordinates via Equation 3.4. In crystal (fractional) coordinates, atomic positions are defined as ratios of the unit-cell lattice vectors; atomic positions in the unit cell take on values between 0 and 1. To eliminate symmetry equivalences, we therefore delete all atoms with crystal coordinates that are greater than 1 or less than zero 0. This will eliminate any atoms that fall outside the fixed unit cell. To complete this procedure and prepare for the visualization of our structure, we need to convert back to crystal coordinates from Cartesian using the transformation

$$A_{\text{cartesian}} = A_{\text{crystal}} \cdot U_{\text{cartesian}}. \tag{3.7}$$

3.1.8 Step 8: Visualizing and Saving the Moiré Structure

Finally, we can visualize the obtained structure and write atomic positions for the substrate and rotated overlayer to a single file. Table 3.3 shows the new structures obtained for different combinations of (m, n). The size of the unit cell and the total number of atoms in the cell are proportional to $m + n$. Table 3.2 shows the relationship between the rotation angle, the number of atoms in the unit cell, and

Table 3.3: The top view of the new unit cells of bilayer graphene for (m, n) parameters of (2,1), (3,1), and (3,2), respectively. Note that the top and bottom layer have the same number of atoms. The symmetry properties of Moiré unit cells permit us to use planewave DFT codes with periodic boundary conditions.

Rotated (2,1)	Rotated (3,1)	Rotated (3,2)
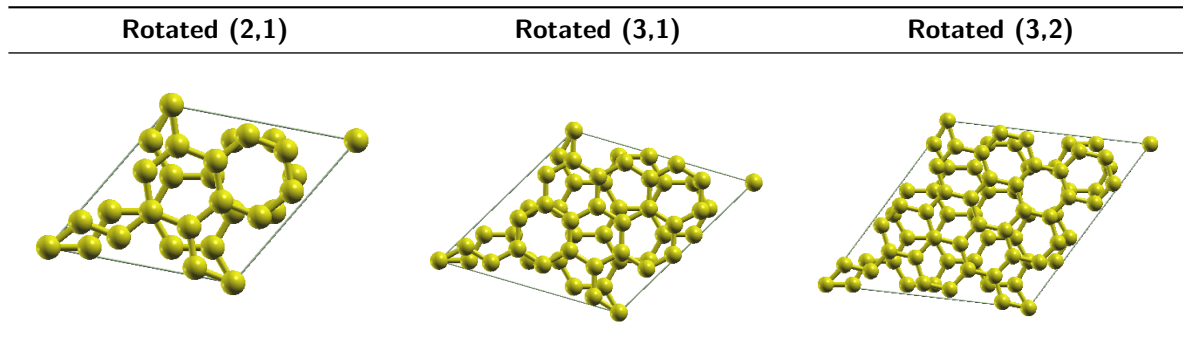
the parameters (m, n) for the homogeneous bilayer materials studied in this work.

3.2 The BiCrystal Code

3.2.1 Program Structure

The `BiCrystal` code is a Python 3 program with over 700 lines of code. For convenience, we have sectioned the code into three main parts: 1) initialization, 2) functions, and 3) the main program.

Initialization

The initialization imports all the required libraries into the Python 3 work environment. The libraries used in `BiCrystal` include **pandas**, **numpy**, **scipy**, **shapely**, and **crystals**. A full installation of Python 3 normally includes all these packages by default, except for the **shapely** and **crystals**[165] packages, which must be installed separately as described in Appendix A. Below we describe the usage of selected packages imported in our program. For a full list of the packages and functions imported into the program, see the source code in the appendices.

- **crystals** - The crystals package provides functions that provide convenient manipulation of crystal structures. It contains tools that allow us to extract the atomic positions and chemical symbols from CIF files. Additionally, we can switch from fractional to Cartesian coordinates using only the crystals package.

- **shapely** - From shapely, we import functions that allow us to work with points enclosed in a polygon. We apply this when dealing with atoms bounded by the unit cell.

- **pandas** - Pandas is a very versatile Python library for data science. In our program, we use pandas to read the csv file containing the periodic table of elements. With pandas, we can extract the

columns we need from this file and create a list of atomic numbers and atomic symbols.

- **sklearn** - Scikit learn, typically used for building machine learning algorithms, contains the *nearest neighbors* algorithm. We employ this algorithm to determine which pairs of atoms should form bonds, and which ones should not. We use a small threshold around the calculated bond distances.

- **matplotlib** - We use functions in matplotlib to generate a 3D plot of the atomic positions, with the chemical bonds assigned by sklearn.

- **numpy** - We use numeric python for all of our matrix calculations.

Functions

In addition to the standard functions imported from Python libraries, we define supplementary functions to execute repetitive tasks in our algorithm. This includes tasks such as determining which atoms belong to the bottom and top layers, creating the new unit cell, and determining which atoms are in the new unit cell. See the *functions* section in the source code accessible via the supplementary information provided in the appendices.

Main Program

The first part of the main program prints information about the `BiCrystal` program and initiates the output environment for the program. We have labeled this environment as **workspace**. All the output will be written to this file. The final formatting and saving of this file into a Quantum ESPRESSO input file is done from the **bicrystal** bash script. This file is present in the zip folder when the `BiCrystal` program is downloaded. See Appendix for A for more details.

After the workspace has been created, the user is prompted to enter their CIF file, (m, n) parameters, and to choose the initial atoms within the top and bottom layers. This immediately executes the first three steps of our algorithm as described in sections 3.1.1, 3.1.2 and 3.1.3.

The remaining portion of the main program can be further split into 4 parts: 1) bottom layer, 2) Top layer, 3) Plotting, and 4) Summary report. Below, we describe the key elements of each subsection in the main program.

- **Bottom layer** - In this part, we use the parameters entered by the user in the previous steps to replicate the unit cell multiple times in the x and y directions using nested **for** loops. Note that, if the replicated supercell is not large enough, we could end up with missing atoms in the rotated structure. One way of ensuring that this doesn't happen would be to loop over a very large integer L, where $L \gg m$ and $L \gg n$. This, however, may pose a computational problem since looping over an arbitrarily large number of nested **for** loops can be computationally expensive. For this reason, we have optimized our code not to loop over a rigid parameter L, but to determine L based

on the input values of m and n. We have found that $L = (m + n) \times 15$ yields reliable results and is computationally tractable even for structures with over five thousand atoms (see Table 3.4 and Figure 3.9). The bottom layer section of the `BiCrystal` code executes steps 4 and 5 (Equations 3.1.4 and 3.1.5) for the bottom layer atoms.

- **Top layer** - In addition to all the procedures carried for the bottom layer, we multiply each overlayer atom by the rotation matrix 3.6. This completes steps 4 through 7 (3.1.4, 3.1.5, 3.1.6, 3.1.7) for the overlayer atoms.

- **Plotting** - We use **matplotlib** functions generate a simple 3D plot of the new structure. In order to include the chemical bonds only between atoms that are within the bond radius, we employ the *nearest neighbor* function from the **sklearn** library.

- **Summary report** - The final part of the program prints out a summary of the results. This includes the number of atoms in the top and bottom layers of the final structure, the Moiré angle, and the Moiré constant. The user has the option to save the results as a Quantum ESPRESSO input file or quit the program.

3.2.2 Download, Installation and Usage

Download and Installation

For information on how to download and install the `BiCrystal` program, see appendix A.

Usage

`BiCrystal` is an interactive program that prompts input from the user. To start the program, in the terminal window type:

```
$ bicrystal
```

Firstly, we input the CIF file which must be located in the current directory. Let us use a CIF file with filename graphene.cif as an example.

```
   ***Input cif file***
graphene.cif
```

Next, we input the scaling parameters (m, n). Let $m = 2$ and $n = 1$, for instance. `BiCrystal` calculates the relative rotation angle for the given m and n. In this case, the rotation angle will be 21.79 degrees. Information about rotation, unit conversions, and bond distances will be printed to the output file.

```
 ***Rotation parameters***

Enter m 2

Enter n 1
```

After that, the user will be required to pick a zeroth atom from each of the layers. If we were picking the atoms by hand using visualization software such as XCrysDen, this would be the atom from which we start when creating the new cell vectors, i.e., the initial atoms according to Section 3.1.2. Let us pick atoms 1 and 3.

```
  Intializing atoms...

Initial TOP atoms..
Atom No. 1   c   [0.  0.  0.5]
Atom No. 2   c   [0.66667 0.33334 0.505  ]
```

```
Initial BOTTOM atoms..
Atom No. 3   c   [0. 0. 0.]
Atom No. 4   c   [0.33333 0.66667 0.005  ]
```

```
Select zeroth TOP atom
Enter Atom No. 1

Select zeroth BOTTOM atom
Enter Atom No. 3
```

After picking the initial atoms, a message will be printed to the screen showing that the calculation is in process.

```
Zeroth TOP (angstrom) c [0.     0.    3.348]

Zeroth BOTTOM (angstrom) c [0. 0. 0.]

Bond distance =  1.418

Lattice Vectors  (Angstrom)
      2.126958    -1.228000     0.000000
      0.000000     2.456000     0.000000
      0.000000     0.000000     6.696000

Lattice Vectors  (Bohr)
      4.019369    -2.320584     0.000000
      0.000000     4.641167     0.000000
      0.000000     0.000000    12.653605

Rotation angle theta (degrees) =  19.106605350869096

Moire angle gamma (degrees) =  21.7867892982618

CALCULATING ATOMIC POSITIONS...

Please wait...
```

Figure 3.4: A simple 3D plot from `BiCrystal` for AB-stacked graphene. The parameters (m, n) have been set to $(4, 3)$.
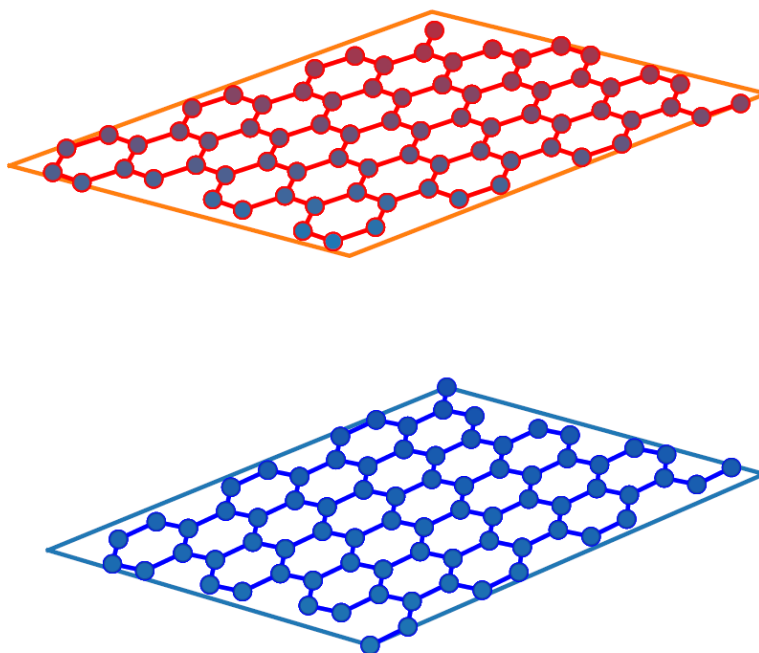
A window displaying a simple 3D plot of the new unit cell will popup shortly after the calculation is done. Figure 3.4 shows a sample of the plots generated with `BiCrystal`.

Finally, a summary report will be printed to the screen, followed by the option to save or exit the program. The result can be saved as a Quantum ESPRESSO input file. For more sophisticated visualization tools, this file can be opened with the native visualization software for Quantum ESPRESSO files, XCrysDen.

```
********************* SUMMARY REPORT **********************

Rotation angle (deg) =   19.107
Relative Rotation (deg) =   21.787

Top atoms(rotated) =   14
Bottom atoms   =   14


Total atoms
= 28


************************** Done! **************************

Would you like to write Espresso file?[Y/n]
```

Figure 3.5: The top view of a graphene unit cell with 124 atoms. This structure is generated from parameters $(5, 1)$.
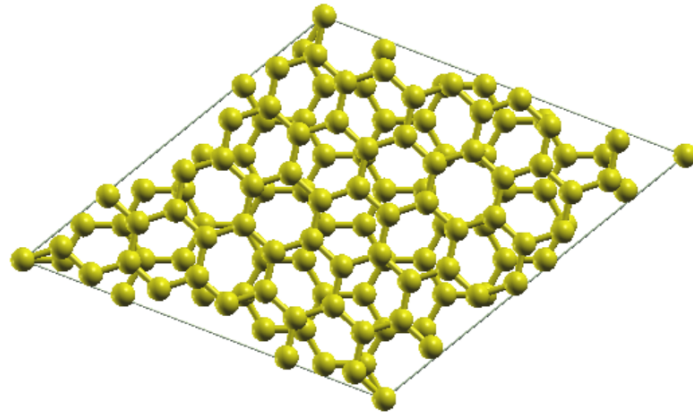
Figure 3.6: The top view of a h-BN unit cell with 148 atoms. This structure can be generated from parameters $(4, 3)$.
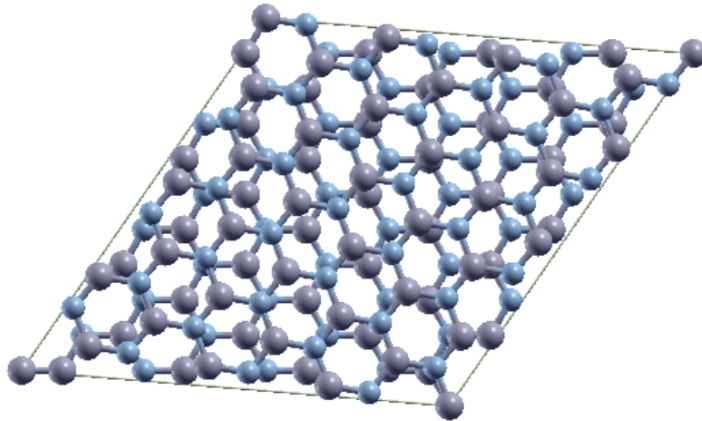
3.2.3 Examples

Graphene $(5, 1)$

The unit cell of graphene generated from (m, n) parameters $(5, 1)$ will have 124 atoms. The top view of this structure is shown in Figure 3.5.

h-BN $(4, 3)$

The unit cell of hexagonal boron nitride generated from (m, n) parameters $(4, 3)$ will have 148 atoms. Figure 3.6 shows the top view of this structure.

Figure 3.7: The top view of a blue phosphorene unit cell with 172 atoms. This structure can be generated from parameters $(6, 1)$.
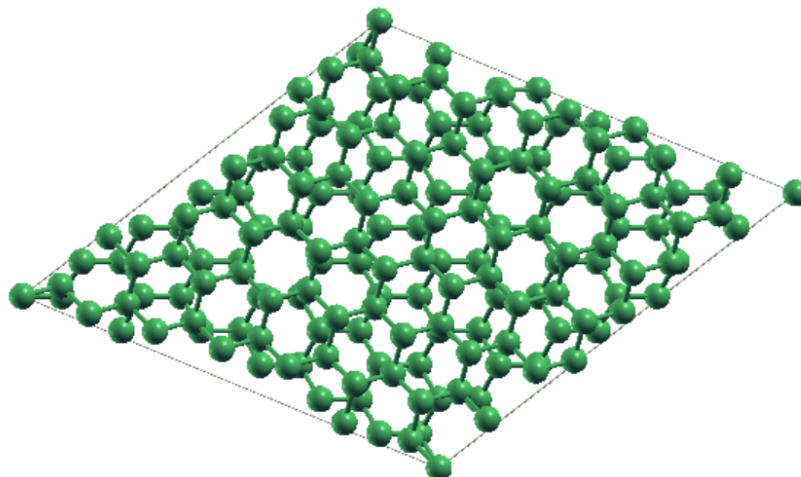
Figure 3.8: The top view of an MoS_2 unit cell with 222 atoms. This structure can be generated from parameters $(4, 3)$.
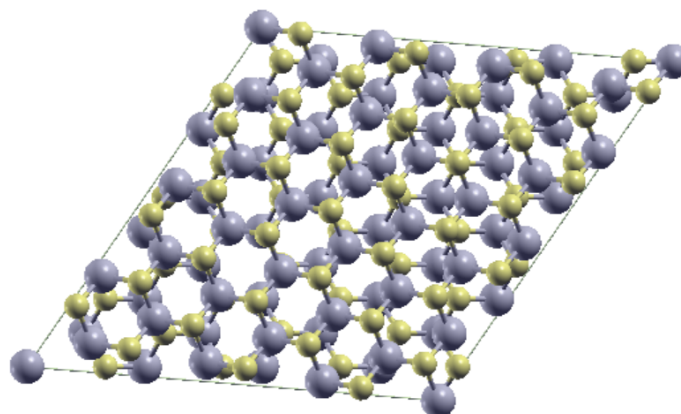
Blue Phosphorene $(6, 1)$

The unit cell of blue phosphorene generated from (m, n) parameters $(6, 1)$ will have 172 atoms. The top view of this structure is shown in 3.7.

MoS_2 $(4, 3)$

The unit cell of molybdenum disulfide generated from (m, n) parameters $(4, 3)$ will have 222 atoms. Figure 3.8 shows the top view of this structure.

Table 3.4: Computational time for different components of the `BiCrystal` program. We report the replication, bottom layer, top layer, and plotting computational times for graphene for different values of (m, n) parameters.

(m, n)	Number of atoms	Replication (s)	Bottom layer (s)	Top layer (s)	Plotting (s)
$(2, 1)$	28	0.03	0.25	0.17	16
$(3, 1)$	76	0.07	0.55	0.48	16
$(6, 5)$	364	0.25	2.8	2.7	22
$(9, 8)$	868	0.46	8.0	8.0	21
$(12, 11)$	1588	0.78	19.80	19.80	25
$(15, 4)$	2524	1.23	41.80	41.80	33
$(18, 17)$	3676	1.74	79.40	79.30	40
$(21, 20)$	5044	2.46	138.6	137.46	53

3.2.4 Performance

The computational time required to run `BiCrystal` can range from a few seconds to a few minutes depending on the number of atoms in the resulting structure. Thanks to the optimization strategy employed in the replication of the unit cell as discussed earlier in this section, we have been able to cut down the cost of the replication procedure while maximizing the program's reliability. We are guaranteed no missing atoms in the superstructure.

Table 3.4 and Figure 3.9 show the performance of each subsection of the **main program**, while Figure 3.10 shows how the sum of the input parameters, $m + n$, relates to the number of atoms in the resulting structure. We have used graphene as an example, but this applies to h-BN and blue phosphorene as well. For smaller values of m and n, it would seem that the most expensive component of the program is the plotting; however, larger values of the input parameters shows us that this is not always the case.

The **top** and **bottom layer** parts are the most computationally expensive components of the program. For large unit cells, this is due to the inverse matrix operations that are done on every substrate and overlayer atom. A potential solution to this problem would be to bypass matrix inversions by operating solely in crystal coordinates. However, this may introduce new complications to the algorithm arising from the non-trivial rotation matrix operations in crystal coordinates.

Invoking different approaches from crystallographic theory, for instance, rotation matrices from Miller indices,[166] Bunge Euler angles,[167] or Rodrigues-Frank vectors,[168–171] could possibly overcome these challenges. The efficacy of these methods shall be explored in a future version of the `BiCrystal` program.

3.3 Conclusion

Bilayer structures involving Moiré patterns are currently a significant component of theoretical studies in tribology, nanotechnology, and electronics due to their peculiar electronic and physical properties, such as superconductivity and superlubricity (ultra-low friction).[19, 28, 152–156] To our knowledge, there is currently no software or algorithm readily available for the purpose of creating Moiré unit cells for

Figure 3.9: The performance curves for different components of the `BiCrystal` program.
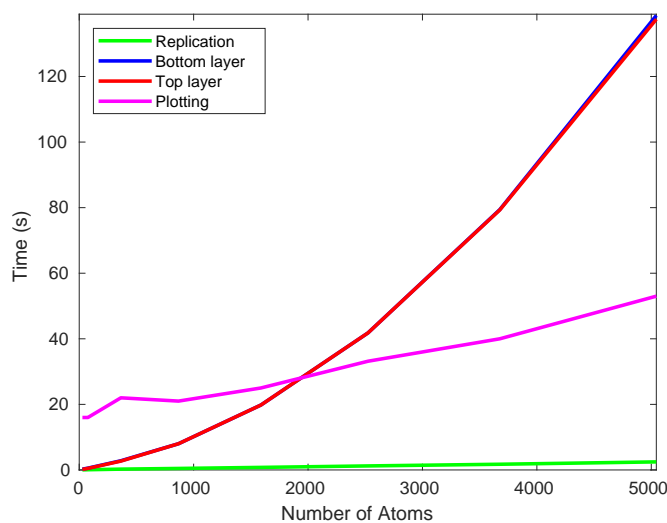
Figure 3.10: The relationship between (m, n) parameters and structure size. We see that small increments in m and n drastically increase the number of atoms in the unit cell.
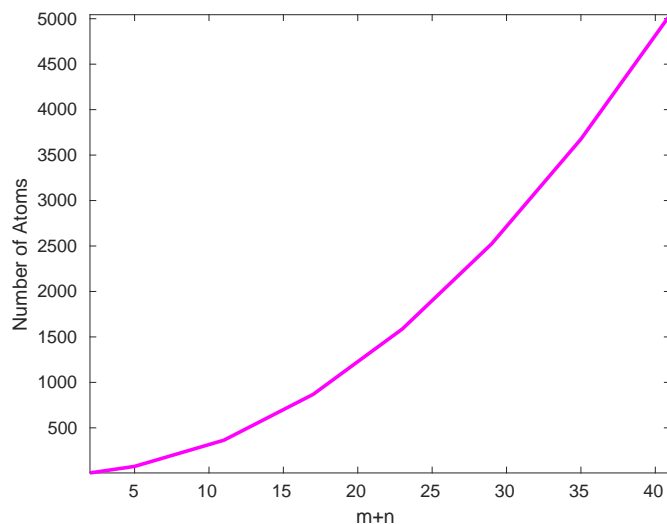
plane-wave DFT calculations. This deficit, combined with the insurmountable challenge of creating very large Moiré unit cells by hand, has motivated us to develop the `BiCrystal` program.

The program structure, usage, performance, and the underlying 8-step algorithm on which it is based, have been discussed in this chapter. We have demonstrated the reliability of our program for creating Moiré unit cells of various sizes. From the performance curves, we have shown how different components of the program scale with structure size. The top and bottom layer calculations are the most computationally expensive due to the inverse matrix operations required for every substrate and overlayer atom. We have discussed possible approaches from crystallographic theory that can be used to evade some of the inverse matrix conversions, which shall be pursued in future versions of the code.

We have demonstrated that, despite the computational challenge posed by matrix operations, our program is still very reliable for large structures. Even for structures with more than five thousand

atoms, our program is capable of producing sensible results within a few minutes. DFT calculations are typically limited to only a few hundred atoms due to the computational cost of DFT itself. Thus, generating structures with thousands of atoms is not a major hindrance at present.

We have used our program to generate Moiré unit cells for graphene, h-BN, MoS_2, and blue phosphorene, which enabled the study of the ultra-low frictional properties of these materials presented in the next chapter of this thesis. Finally, we hope that the simplicity of this algorithm and accessibility of our code will continue to aid future theoretical and computational studies involving Moiré structures.

Chapter 4

Theoretical Modeling of Structural Superlubricity in Rotated Bilayer Graphene, Hexagonal Boron Nitride, Molybdenum Disulfide, and Blue Phosphorene

T. Kabengele and E. R. Johnson. Theoretical Modeling of Structural Superlubricity in Rotated Bilayer Graphene, Hexagonal Boron Nitride, Molybdenum Disulfide, and Blue Phosphorene, *Nanoscale*, 2021. DOI: https://doi.org/10.1039/D1NR03001A. Copyright 2021 Royal Society of Chemistry

Contributions to the submitted manuscript   TK performed the calculations, and wrote the first draft of the manuscript. ERJ contributed to the final version of the manuscript, and supervised the project.

4.1   Motivation

The frictional properties of solid lubricants, such as graphite and MoS_2, have been widely studied for many years. Fundamentally, the force of friction originates from molecular interactions between constituent atoms of solids due to atomistic locking.[11] The phenomenon of structural superlubricity,[12,39,49] where friction completely vanishes for incommensurate interactions between two clean, atomically flat surfaces, was predicted[11,172] and subsequently verified experimentally in graphite[13,17,43] and other layered materials.[14–16,161,162,173,174]

Experimental surface-force techniques, such as atomic force microscopy, are typically used to investigate frictional properties of layered two-dimensional (2D) materials and surfaces. In an experimental

investigation of the frictional properties of graphite, Dienwiebel *et al.*[13] examined the energy dissipation for the tip of a frictional force microscope (FFM) sliding over a graphite surface under a dry nitrogen atmosphere. They measured the atomic-scale friction as a function of the rotational angle between the tip and the top layer of the graphite surface, and found ultra-low friction regimes between rotated graphite layers. Similar studies have been conducted on a wide range of 2D materials, including MoS_2,[14] and heterostructures of graphene with h-BN.[15, 161] These studies have demonstrated that structural superlubricity results from the incommensurability of the surfaces in contact.

Further theoretical and experimental work is needed to gain a better understanding of the atomic-scale processes at the sliding interface. Notably, Claerbout *et al.*[20] recently suggested a novel mechanism for achieving low friction in commensurate MoS_2, and concluded that incommensurability may not be a requirement for superlubricity. In their work, low-friction regimes were achieved by varying the direction of the driving force during a classical molecular-dynamics (MD) simulation involving commensurate MoS_2 layers.

Classical MD simulations provide a good approximation of the dynamic and mechanical properties of a system. However, choosing an accurate empirical potential is critical to predicting realistic behaviour. Due to the numerous empirical potentials and parameters that exist, researchers need to be able to carefully evaluate the efficacy and accuracy of these models. Since MD simulations rely heavily on empirical parameters, they are less accurate than electronic-structure methods, such as density-functional theory (DFT).

In this work, we use dispersion-corrected DFT to investigate structural superlubricity in rotated bilayers of graphene, h-BN, MoS_2, and blue phosphorene (b-P). We model the sliding PES for Moiré cells of these materials with $0°$, $13.17°$, $21.79°$, and $32.20°$ relative rotation angles. Additionally, we compute the exfoliation energy and rotation barriers of each material. We show that commensurate sliding of 2D materials along very specific trajectories results in small barriers, suggesting that incommensurability is not required for low friction. However, drastically lower sliding barriers are found for the rotated cells. These results confirm superlubricity for rotated graphene, MoS_2, and h-BN, and we report the first prediction of superlubricity for the novel material b-P.

4.2 Computational Methods

4.2.1 Unrotated Structures, $\varphi = 0°$

Crystal structures for graphite, h-BN, and MoS_2 were obtained from the crystallographic open database (COD).[175] The structure for b-P was constructed based on known parameters in the literature.[176, 177] Graphene, h-BN, MoS_2, and b-P have hexagonal unit cells; their x, y-lattice parameters, $a_\circ$, were held fixed at the experimental values of 2.47, 2.51, 3.15, and 3.33 Å, respectively. Bilayer structures of the

Table 4.1: Commensurate structures of bilayer graphene, h-BN, MoS$_2$, and b-P with 0° rotation of the top layer.[178]

Material	View 1	View 2	View 3
Graphene			
h-BN			
MoS$_2$			
b-P			
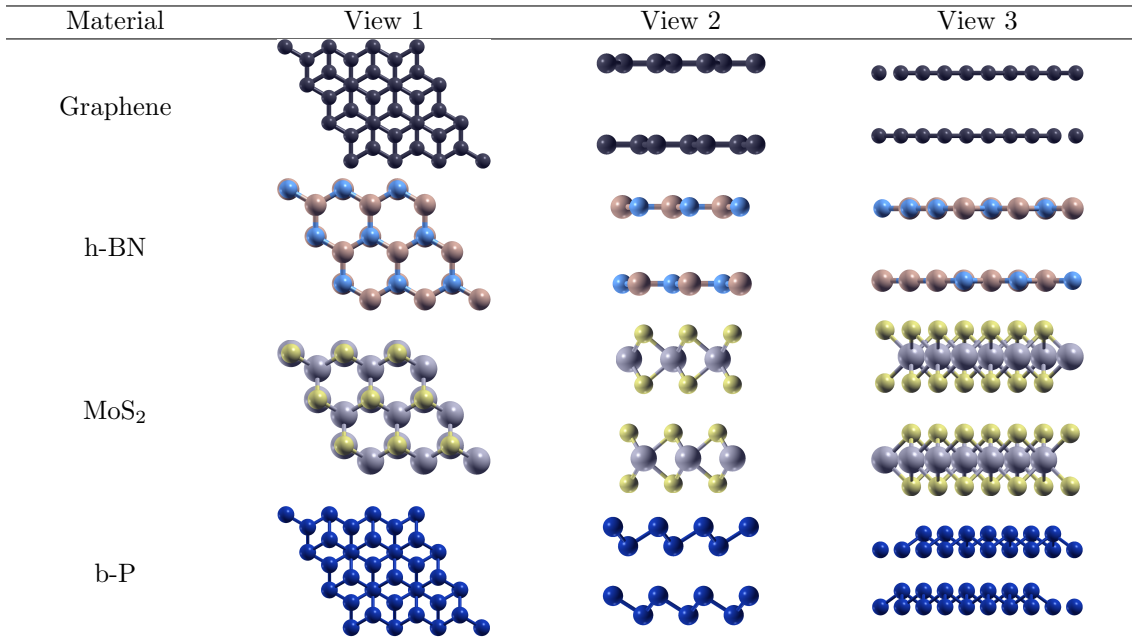
Table 4.2: The (m, n) parameters and the relative rotation angles, φ, of the overlayer to the substrate for the Moiré unit cells. The numbers of atoms in the graphene, h-BN, and b-P unit cells are also shown; the MoS$_2$ unit cells contain 1.5 times more atoms.

(m, n)	φ (degrees)	Atoms
(1×1)	0.00	4
$(2, 1)$	21.79	28
$(3, 1)$	32.20	52
$(3, 2)$	13.17	76

materials were generated by inserting a large vacuum region, such that all unit cells spanned 80 Bohr (42.33 Å) in the z direction. The relative rotation angle of the overlayer to the substrate, φ, is implicitly 0° in this case. Table 4.1 shows the unrotated structures of these materials.

4.2.2   Rotated Structures, $\varphi \neq 0°$

Rotating the overlayer with respect to the substrate creates Moiré patterns.[81] Appropriate choices of rotation angle allow definition of sufficiently small unit cells to allow us to perform planewave DFT calculations, which require periodic boundary conditions.

Obtaining Moiré unit cells for hexagonal lattices through the rotation of one layer with respect to the other has been discussed at length elsewhere.[83, 164] We let $\mathbf{a}_\circ$ and $\mathbf{b}_\circ$ be the lattice vectors of the (1×1) cell of a given material. The full range of the possible unit cells is given by two parameters, (m, n), used

Table 4.3: Rotated structures of graphene, h-BN, MoS_2, and b-P.[178]

(m, n)	$(2, 1)$	$(3, 1)$	$(3, 2)$
Graphene			
h-BN			
MoS_2			
b-P			
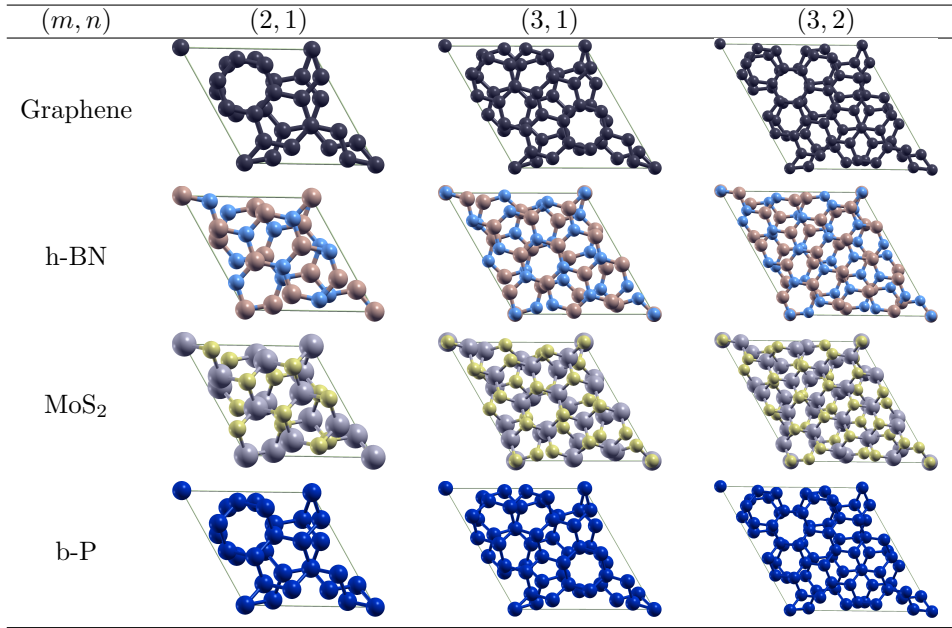
to define the lattice vectors of the resulting Moiré unit cell:

$$\mathbf{a}_m = m\mathbf{a}_\circ + n\mathbf{b}_\circ \tag{4.1}$$

and

$$\mathbf{b}_m = -n\mathbf{a}_\circ + (m + n)\mathbf{b}_\circ, \tag{4.2}$$

where $m, n \in N$, and $m > n$. The rotation angle for the hexagonal Moiré cell is then evaluated as

$$\cos(\varphi) = \frac{m^2 + 4mn + n^2}{2(n^2 + mn + m^2)}. \tag{4.3}$$

We implemented the scheme described above in a `python` program to obtain rotated structures with (m, n) parameters of $(2, 1)$, $(3, 1)$, and $(3, 2)$ for each material. These correspond to relative rotation angles of 21.79°, 32.20°, and 13.17°, respectively. Tables 4.2 and 4.3 show the number of atoms in the respective Moiré unit cells, and the top views of these structures, respectively.

4.2.3 Density-Functional Theory

All DFT calculations in this work were carried out with the projector augmented-wave approach[147, 179] and the B86bPBE[107, 110] exchange-correlation functional using Quantum ESPRESSO.[135] The eXchange-hole Dipole Moment (XDM) model,[85, 130] previously shown to be highly accurate for properties of layered materials,[78] was used to account for dispersion interactions. The total electronic energy can then be

written as

$$E = E_{\text{base}} + E_{\text{disp}}, \tag{4.4}$$

where E_{base} is the contribution from the base B86bPBE density functional, which includes electrostatics and non-bonded repulsion, while E_{disp} is the XDM dispersion energy. The XDM damping parameters were taken as their canonical values for use with the B86bPBE functional ($a_1 = 0.6512$, $a_2 = 1.4633$ Å).

The planewave cutoff energies were set to 80 Ry for the wave functions and 800 Ry for the electron density. All calculations used uniform k-point sampling, with $8 \times 8 \times 1$, $6 \times 6 \times 1$, $4 \times 4 \times 1$, and $2 \times 2 \times 1$ meshes selected for the 4-atom, 28-atom, 52-atom, and 76-atom unit cells, respectively. For MoS_2, k-point meshes of $8 \times 8 \times 1$, $4 \times 4 \times 1$, $2 \times 2 \times 1$, and $1 \times 1 \times 1$ were used for the 6-atom, 42-atom, 78-atom, and 114-atom unit cells, respectively. For geometry relaxations, the convergence thresholds were set to 10^{-5} Ry for the energy and 10^{-4} Ry/Bohr for the forces.

For both the (1×1) and rotated cells, all atomic positions were relaxed with the cell parameters held fixed. 2D sliding of each material was then modeled by gradually translating the atoms comprising the overlayer along the long diagonal of the unit cell in a series of 50 increments. During sliding, the x, y atomic positions were held fixed, with the z atomic positions allowed to relax at each point to properly determine the interaction energy between the layers in the z (normal) direction. The minimum energy points on the resulting potential energy surfaces were then identified and used to evaluate the rotation barriers and exfoliation energies.

The rotation barriers were computed as

$$\Delta E_{\text{rot}} = E_{\text{min,rotated}} - E_{\text{min,unrotated}}, \tag{4.5}$$

where $E_{\text{min,rotated}}$ and $E_{\text{min,unrotated}}$ are the minimum energies obtained for the rotated and unrotated geometries. The exfoliation energies (i.e. the energy required to separate the layers) for the unrotated cells were evaluated using

$$\Delta E_{\text{ex}} = E_{\text{min,unrotated}} - 2E_{\text{monolayer}}, \tag{4.6}$$

where $E_{\text{monolayer}}$ is the energy of a single layer. The rotation and exfoliation energies are typically expressed either per atom or per unit area. For a hexagonal cell, the area is $A = (\sqrt{3}/2)a_\circ^2$.

4.3   Results and Discussion

4.3.1   Exfoliation Energies

Exfoliation energies were computed according to Eqn. 4.6 for the (1×1) unit cell of each bilayer. These values will be roughly half those for the bulk materials. Our B86bPBE-XDM method has been

Table 4.4: Total exfoliation energies of the bilayer materials, in meV/atom, as well as the separate base-functional and dispersion contributions. Values in meV/Å^2 are given in parentheses.

Material	Total	Base	Dispersion
Graphene	24.4 (18.5)	-8.5 (-6.4)	32.9 (24.9)
h-BN	29.4 (21.6)	-5.7 (-4.2)	35.1 (25.7)
MoS_2	32.5 (22.7)	-11.1 (-8.8)	43.6 (30.4)
b-P	25.6 (10.7)	-14.5 (-6.0)	40.1 (16.7)

shown to perform extremely well for the exfoliation energies of layered materials.[78] It should be noted that the exfoliation energies for bulk graphite and h-BN obtained with B86bPBE-XDM (viz. 54.31 and 56.32 meV/atom, respectively[78]) are effectively identical to those from HSE-MBD (viz. 53.29 and 58.17 meV/atom, respectively[180]). In a recent study, PES generated with HSE-MBD were used to parameterize a force field for subsequent MD simulations that yielded frictional properties in good agreement with available experimental data.[180] It was further concluded that fairly sophisticated DFT-based dispersion models (such as MBD and XDM) that include electronic many-body effects[123, 181] were essential for good performance. For contrast, the HSE-TS method, which does not include electronic many-body effects, gave much higher exfoliation energies of 85.12 and 89.85 meV/atom for graphite and h-BN, respectively.[180]

Table 4.4 shows the bilayer exfoliation energies, along with a decomposition into the base density-functional and XDM dispersion terms. The base functional contributions are all negative, as expected since dispersion is responsible for binding of these layered materials. In the absence of the XDM dispersion correction, there would be no binding between the layers, since the base B86bPBE functional is dispersionless. The dispersion energy is larger in magnitude than the total exfoliation energy, as dispersion must also compensate for the non-bonded repulsion between the layers arising from the base functional.

The overall trend in the magnitude of the dispersion energies (per atom) is graphene<h-BN<b-P<MoS_2, while for the total exfoliation energies, this trend is changed to graphene<b-P<h-BN<MoS_2. The base functional repulsion is lower for h-BN than for the other three materials since it adopts a stacked configuration to maximize favourable electrostatic interactions, rather than a staggered configuration to maximize dispersion (see Table 4.1).
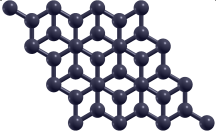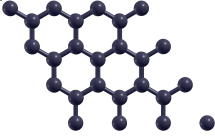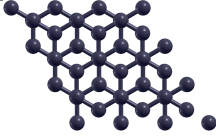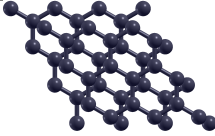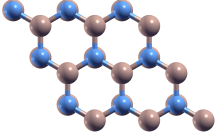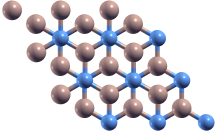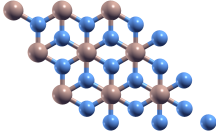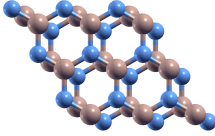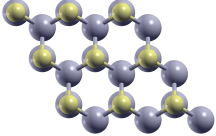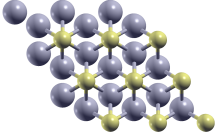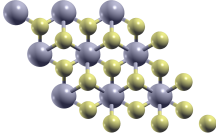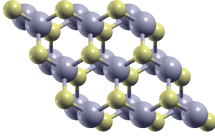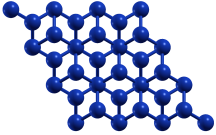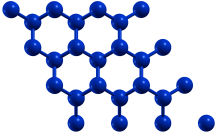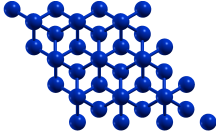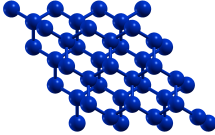
4.3.2   Sliding PES without Rotation, $\varphi = 0°$

Figure 4.1 shows the PES for interlayer sliding of the unrotated (1×1) unit cells. Similar results have been reported previously for graphene, h-BN, and MoS_2.[73] For each material, two minima are obtained at fractional sliding coordinates of 0 and ²/₃, while two maxima, corresponding to high- and low-friction peaks, are seen at fractional coordinates of ¹/₃ and ⁵/₆, respectively. The geometries of these stationary

Figure 4.1: Potential energy surfaces for interlayer sliding of the unrotated unit cells (black lines) of (a) graphene, (b) h-BN, (c) MoS_2, and (d) b-P. The horizontal lines represent the rotation barriers for each cell, while the purple line (Avg) is the average of the black curve over all the full PES. Note the larger y-axis scale for MoS_2 and b-P compared to graphene and h-BN.
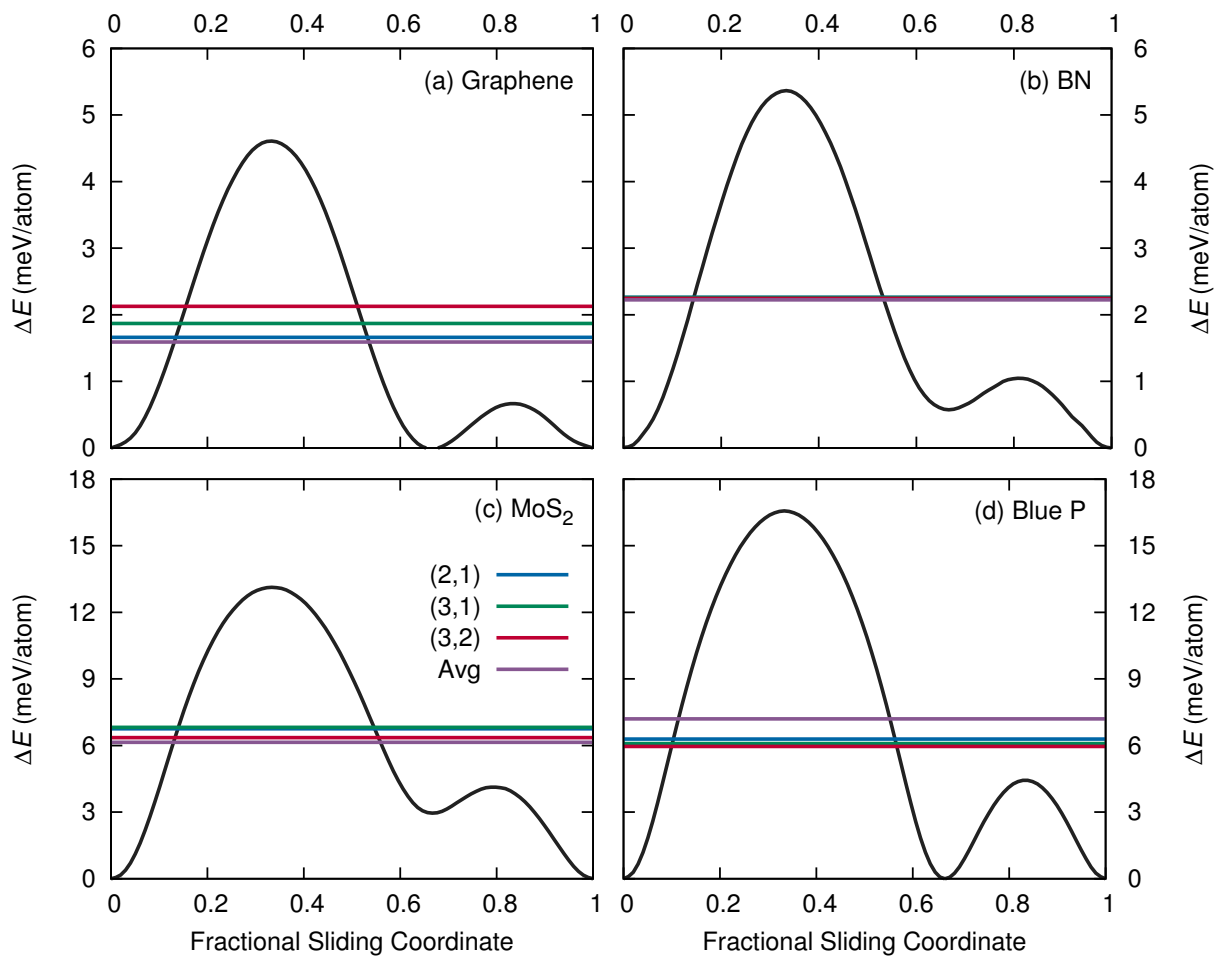
Table 4.5: Geometries of stationary points on the interlayer sliding PES for unrotated, (1×1) unit cells.[178]

Material	Global Minimum	Global Maximum	Local Minimum	Local Maximum
Graphene				
h-BN				
MoS$_2$				
b-P				

points are shown in Table 4.5.

For graphene, the two minima are degenerate (i.e. equal in energy) and have the atomic layers staggered to maximize dispersion interactions while minimizing non-bonded repulsion. The global maximum has the layers stacked so that the atoms are perfectly aligned in the z direction. Conversely, for h-BN, the global minimum has the layers aligned with the B atoms located directly above or below the N atoms of the other layer to maximize favourable electrostatic interactions. The higher-energy local minimum for h-BN has the B atoms vertically aligned, but the N atoms staggered, while the global maximum has the N atoms vertically aligned and the B atoms staggered. The global minimum for MoS$_2$ also has stacked layers, with the S atoms from one layer vertically aligned above or below the Mo atoms of the other layer. In the local minimum configuration, the Mo atoms are aligned and the S atoms staggered, to minimize repulsion between the more electronegative S atoms, whereas the S atoms are aligned and the Mo atoms staggered in the global maximum configuration. Finally, the stationary points for b-P resemble those of graphene, with staggered layers for the two degenerate minima and aligned layers for the global maximum.

The sliding barriers, defined as the energy differences between the maxima and minima on the PES, should be directly related to the frictional behaviour of the materials. From Figure 4.1, MoS$_2$ and b-P have sliding barriers approximately 3 times larger than those seen for the graphene and h-BN PES. Unlike graphene and h-BN, the atomically thin layers in MoS$_2$ and b-P are corrugated, leading to a greater contact area and, hence, greater friction. The overall trend for the sliding barriers is graphene<h-BN<MoS$_2$ <b-P.

The two saddle points on the PES in Figure 4.1 show that the top layer feels different energy barriers as

Figure 4.2: Representative 2D potential energy surface for commensurate sliding of a layered material using the unrotated (1×1) cell. The anistropy of the PES leads to different coefficients of friction for different sliding directions. The lowest friction is obtained for the zig-zag paths corresponding to 30° and 90° sliding trajectories, while the highest friction is obtained for 0° and 60° trajectories.
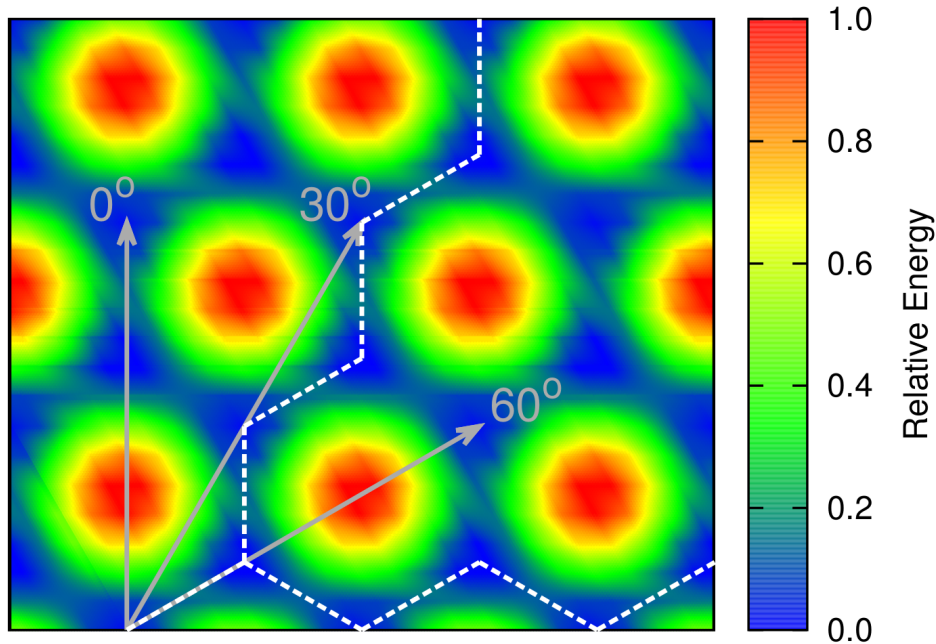
Table 4.6: Minimum-energy sliding barriers, in meV/atom, for the unrotated, (1×1) cells of each material along a zig-zag path, as shown in Figure 4.2; sliding barriers for the various rotated cells are shown for comparison.

Material	(1×1)	$(2, 1)$	$(3, 1)$	$(3, 2)$
Graphene	0.67	0.00	0.00	0.00
h-BN	1.05	0.01	0.01	0.01
MoS_2	4.13	0.16	0.15	0.36
b-P	4.44	0.41	0.33	1.33

it slides over different regions of the substrate within the unrotated, commensurate unit cell. This means that, for unrotated structures, sliding in different directions can yield remarkably different frictional behaviours. Using classical MD, Claerbout *et al.*[20] recently showed that applying a driving force in different sliding directions can drastically alter the friction in commensurate MoS_2. In their work, a low-friction regime was found when the overlayer slid in a zig-zag path that avoided the higher energy barrier on the potential energy surface, as shown in Figure 4.2. Their findings are consistent with the results in this work and similar energetically favorable sliding paths exist for unrotated, commensurate graphene, h-BN, MoS_2, and b-P. Here, the lower of the two barriers appearing on each PES in Figure 4.1 (for a fractional coordinate of ⁵/₆) corresponds to the barrier for sliding along the minimum-energy, zig-zag path. These values are collected in the first column of Table 4.6 for all four materials.

Table 4.7: Total rotation energies, in meV/atom, as well as the base-functional and dispersion contributions.

Material	(m, n)	Total	Base	Dispersion
Graphene	$(2, 1)$	1.66	0.06	1.60
	$(3, 1)$	1.87	0.37	1.50
	$(3, 2)$	2.13	0.35	1.78
h-BN	$(2, 1)$	2.26	0.11	2.16
	$(3, 1)$	2.26	0.11	2.16
	$(3, 2)$	2.25	0.12	2.12
MoS_2	$(2, 1)$	6.75	-2.12	8.87
	$(3, 1)$	6.82	-2.04	8.86
	$(3, 2)$	6.36	-2.20	8.56
b-P	$(2, 1)$	6.29	-3.80	10.09
	$(3, 1)$	6.09	-4.68	10.77
	$(3, 2)$	5.96	-3.88	9.85

4.3.3 Rotation Energies

The rotation barrier, computed using equation 4.5, is the minimum energy required to obtain a Moiré structure by means of rotating the overlayer with respect to its substrate. These barriers allow us to assess the stability of the Moiré cells, relative to the (1×1) cells. Table 4.7 shows the total rotation energies, as well as the base-functional and dispersion contributions, for each material and rotation angle considered. Similar to the exfoliation energy, the rotation barriers are dominated by dispersion interactions. For graphene and h-BN, the base-functional contributions to the rotation energies are negligible due to the planarity of the 2D atomic layers. The magnitudes of the total and component rotation energies for MoS_2 and b-P are much larger than for graphene and h-BN due to the corrugated nature of the 2D layers in the former two materials.

In the minimum-energy configurations of the (1×1) cells, the MoS_2 and b-P layers are interlocking, allowing close interlayer distances that maximize dispersion attraction. Conversely, in the rotated cells, the layers cannot interlock due to their mis-alignment. This results in larger interlayer distances (by ca. 0.25 Å in MoS_2 and 0.40 Å in b-P, see Table 4.8), which decreases the magnitudes of both dispersion attraction and non-bonded repulsion. Hence, there is a negative contribution to the rotation energy from the base functional due to reduced repulsion in the rotated cell. This is offset by the much greater reduction in dispersion binding, resulting in higher total rotation barriers.

The rotation barriers for each Moiré cell are also shown in Figure 4.1, where they are denoted by the horizontal lines cutting through the sliding PES for the unrotated cells. The rotation barriers are consistently higher than the minimum sliding barriers for the commensurate configurations of each

Table 4.8: Interlayer separation between the top and bottom layers. The minimum ($d_{\min}$), maximum ($d_{\max}$), and average (d_{avg}) z-distances over all the data points in each PES scan are shown. (1×1) denotes the unrotated unit cells.

Material	(m, n)	$d_{\min}$	$d_{\max}$	Δd	d_{avg}
	(1×1)	3.38	3.57	**0.19**	3.45
Graphene	$(2, 1)$	3.43	3.43	0.00	3.43
	$(3, 1)$	3.43	3.43	0.00	3.43
	$(3, 2)$	3.43	3.43	0.00	3.43
	(1×1)	3.29	3.51	**0.22**	3.37
h-BN	$(2, 1)$	3.37	3.37	0.00	3.37
	$(3, 1)$	3.37	3.37	0.00	3.37
	$(3, 2)$	3.34	3.35	0.01	3.34
	(1×1)	2.99	3.60	**0.61**	3.24
MoS_2	$(2, 1)$	3.27	3.27	0.00	3.27
	$(3, 1)$	3.27	3.27	0.00	3.27
	$(3, 2)$	3.24	3.27	0.03	3.25
	(1×1)	3.16	4.08	**0.92**	3.55
b-P	$(2, 1)$	3.54	3.60	0.06	3.59
	$(3, 1)$	3.59	3.62	0.04	3.61
	$(3, 2)$	3.43	3.55	0.12	3.51

material. Their positive values indicate that the rotated cells are less stable than the (1×1) cells and obtaining the rotated structures would therefore require overcoming a significant energy barrier. However, if this barrier is overcome, the energy required to slide the overlayer atop the substrate will drop significantly, as shown in Table 4.6.

Additionally, we find that the rotation barriers are comparable to the average value of the (1×1) sliding PES for each of the four materials. This can be rationalized through understanding of the interlayer contacts. As noted above, the unrotated PES show two distinct maxima, which correspond to high and low frictional contacts. However, when the overlayer is rotated, these distinct contacts are disrupted, resulting in a structure with an even mixture of favourable and unfavourable interlayer contacts. The interlayer interactions of the rotated structure will therefore be a distribution over all the contact points, and the relative energy of the rotated cell will be approximately equal to the average of all the points on the unrotated PES.

4.3.4 Interlayer Separation

The idea that the rotated cells involve averaged interatomic contacts is reinforced further by analysis of the interlayer distances during sliding. As the overlayer slides atop the substrate, the vertical interlayer distance, d, changes due to the varying strength of the potential at different relative sliding positions.

Figure 4.3: Potential energy surfaces for interlayer sliding of Moiré unit cells of (a) graphene, (b) h-BN, (c) MoS_2, and (d) b-P. Note the larger y-axis scale for MoS_2 and b-P compared to graphene and h-BN.
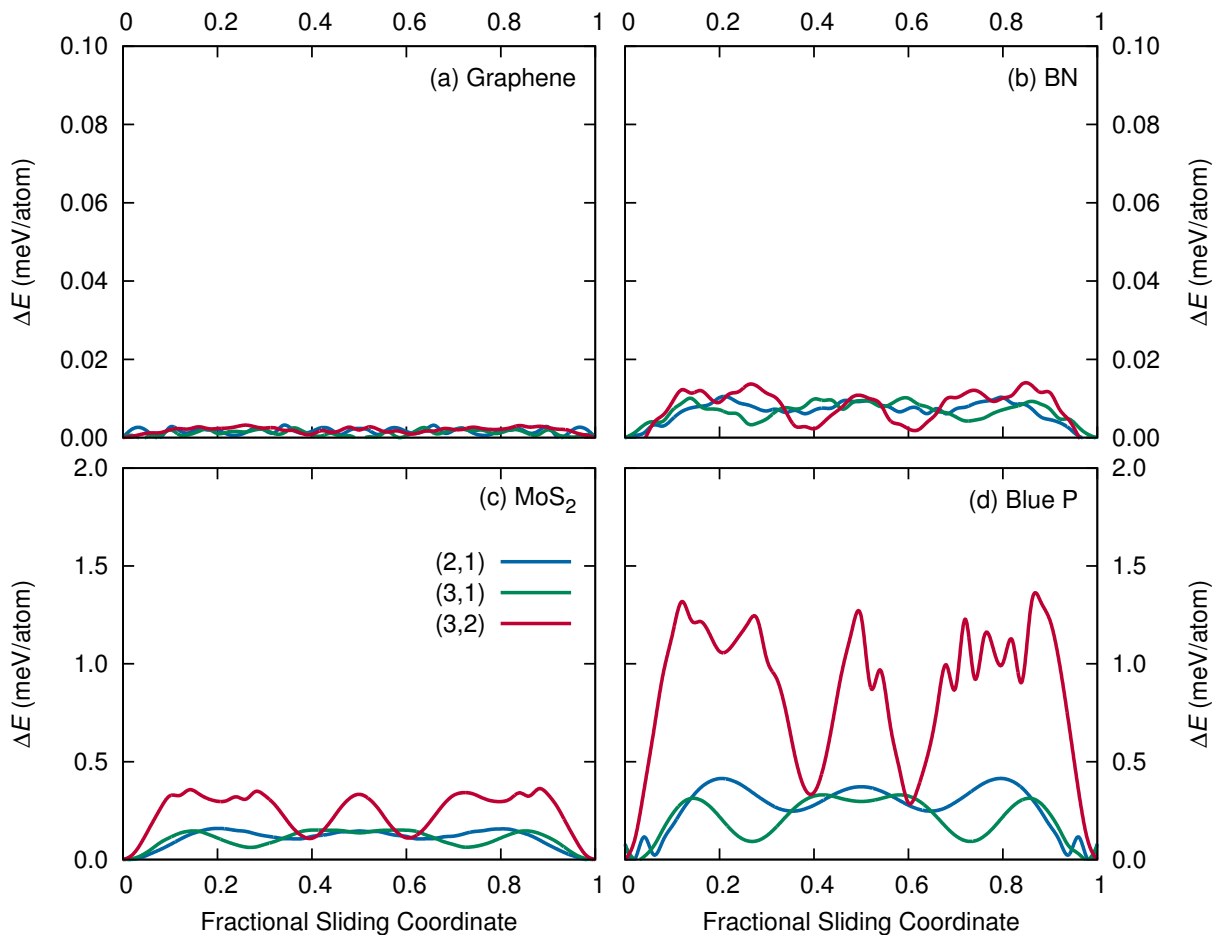
Table 4.8 shows the minimum, maximum, and average interlayer distances obtained along the sliding PES for each material and rotation angle. We find that the average interlayer distances for the unrotated (1×1) cells nearly match those of the rotated cells in all cases.

Table 4.8 also shows the difference between the maximum and the minimum interlayer distances, $\Delta d = d_{\max} - d_{\min}$, for each PES. There is a clear correlation between the Δd values and the maximum sliding barriers. For the (1×1) cells, b-P and MoS_2 show Δd values that are 3-4 times greater than those observed for graphene and h-BN, which is comparable to the observed differences in sliding barriers. Due to their corrugated nature, MoS_2 and b-P have the largest sliding barriers, interlayer-distance differences, and dispersion contributions to the rotation energies (Table 4.7). Further, the (1×1) unit cells consistently show higher interlayer-distance differences than their rotated counterparts and, as we will see in Sec. 4.3.5, much higher sliding barriers as well.

4.3.5 Sliding PES with Rotation, $\varphi \neq 0°$

Figure 4.3 shows the interlayer-sliding PES for the rotated unit cells of graphene, h-BN, MoS$_2$, and b-P. While exhibiting Moiré patterns, these structures have clearly defined unit cells, and satisfy the periodic boundary conditions required in planewave DFT codes. We created each unit cell using the (m, n) scheme,[83, 164] where each combination of integers m and n corresponds to a specific relative rotation angle of the overlayer (see Table 4.2).

A superlubric regime was achieved in the rotated cells for each material. From Figure 4.3 and Table 4.6, the PES for the $(2, 1)$, $(3, 1)$, and $(3, 2)$ Moiré unit cells display much lower sliding barriers than those obtained for the unrotated cells, even along the minimum-energy zig-zag paths. For MoS$_2$ and b-P, which possess corrugated layers, the relative energies across the PES for the rotated cells are are 3-10 times lower than the minimum barriers for the (1×1) cells. Graphene and h-BN, which possess completely planar layers, slid with effectively zero barriers for all the rotated cells and should exhibit ultra-low friction.

We have observed a strong connection between the changes in the interlayer distance reported in Table 4.8, and the sliding barriers. For the rotated cells, virtually no changes in interlayer distance over the sliding PES occurred for graphene and h-BN. For MoS$_2$, a non-zero distance difference was obtained only for $(3,2)$, which gives the highest sliding barrier. Larger changes in interlayer distance are seen for rotated b-P, but they remain much smaller than for the (1×1) cell. In particular, the $(3, 2)$ geometry for b-P showed an interlayer-distance difference greater than 0.1 Å, leading to a sliding potential with relatively high barriers, as shown in Figure 4.3.

Overall, the materials with the smallest changes in the interlayer distance during sliding (graphene and h-BN) result in the smoothest sliding potentials. This means that the lowest friction will be observed in graphene and h-BN, followed by MoS$_2$ and b-P. The variation in the frictional properties in the flat versus the corrugated materials can be understood in terms of averaged contacts and surface area. The disruption of high-energy contact points in the rotated geometries leads to removal of the two distinct maxima observed on the unrotated PES curves. As the rotated geometries involve a distribution of favourable and unfavourable contacts along the entire sliding coordinate, the PES peaks are flattened, thereby permitting structural superlubricity in the rotated structures.

4.4 Conclusions

In this work, we investigated friction in both (1×1) and rotated unit cells of graphene, h-BN, MoS$_2$, and blue-P through density-functional modeling of the potential energy surfaces for interlayer sliding. Higher interlayer sliding barriers are predicted for MoS$_2$ and blue-P, compared to graphene and h-BN, which is likely due to the corrugation of the layers and the larger contact areas for these two materials.

The average of the interlayer distances across the unrotated PES is consistently found to be a good approximation to the interlayer distance in the rotated cells. Similarly, the average of the unrotated sliding potential is found to be a good approximation to the rotation energy, since the rotated cells involve both favorable and unfavorable contacts. This distribution of contacts results in a smoothing of the PES, leading to ultra-low friction for the rotated cells.

The PES for the unrotated structures indicate that the zig-zag sliding path (see Figure 4.2) predicted for unrotated MoS_2 by Claerbout *et al.*[20] should be observed for all 4 materials. However, provided the rotational barriers can be overcome, much lower friction regimes are achieved in the rotated structures. Our findings confirm structural superlubricity in rotated graphene, h-BN, and MoS_2, and provide the first prediction of this phenomenon in the novel material b-P for two of the three rotation angles considered.

Although superlubricity is expected in the rotated configurations, sliding without rotation will tend to be more favourable because of the greater stability of the unrotated cells. Altering the geometrical arrangement of the atoms, which results from the formation of Moiré patterns in the lattice, is an integral part to achieving ultra-low friction in each material. Further work is henceforth needed to find new strategies for obtaining stable Moiré structures.[160, 182, 183]

For many years, incommensurability has been the center of attention in achieving superlubricity in 2D materials. Superlubricity is intrinsically more prominent in heterostructures[15] as it is harder to maintain incommensurability in homogeneous configurations because the lattices are more prone to collapse back into their default commensurate orientations. Since achieving incommensurability in experimental settings is a challenge, perhaps targeting specific rotation angles[184, 185] may provide new strategies for achieving superlubricity, and bring us closer to the design of industrially applicable solid superlubricants.

Chapter 5

Computation and Analysis of the Coefficients of Friction from DFT Results

5.1 Motivation

In the previous chapter, we investigated superlubricity in bilayer graphene, h−BN, MoS$_2$, and b−P by examining the interaction energy, E, between the layers as the overlayer slides atop the substrate. The interaction energy is an interplay between Coulomb repulsion and van der Waals interactions. As the top layer slides over the substrate, the interlayer distance, d, varies with the interaction energy along the normal direction. As we demonstrated in the previous chapter, the key to achieving superlubricity lies in attaining smooth potential energy curves with low barriers. Large changes in d and E lead to large energy barriers and high corrugation of the potential energy surface landscape, making interlayer sliding energetically less favourable. Average friction is therefore expected to increase as the change in d and the change in E increase. Though the link between friction and interaction energy is fairly intuitive, it can be quite challenging to fully comprehend the frictional properties of materials solely through the eyes and language of computational chemistry results. For all practical purposes, friction is more broadly understood in terms of the coefficient of friction. The goal of this chapter is, therefore, to showcase how to compute the coefficients of friction, μ, from raw DFT results using the principles of classical physics and basic calculus. We compute μ for the commensurate and rotated cells of all four materials using the DFT data obtained in chapter 4.

5.2 Theory and Methods

5.2.1 Friction

Friction, being a dissipative force, performs negative work, causes a loss in kinetic energy and, therefore, impedes the motion of moving bodies. Friction is generally understood in terms of static and kinetic (or dynamic) friction. Static friction refers to the friction force that prevents a stationary body from sliding (e.g., a body on an inclined plane is kept stationary by static friction), while kinetic friction resists the motion of bodies with non-zero kinetic energy. From classical physics, friction is defined by the empirical Coulomb relation (named after Charles-Augustin de Coulomb),[186–188]

$$F_r = \mu F_N, \tag{5.1}$$

where F_r is the friction, F_N is the normal force (or the load), and μ is the coefficient of friction, which is material dependent. μ is typically 10^{-2} for smooth surfaces, and closer to 1 for rough contacts.[189] In order to calculate μ, we must know F_r and F_N.

5.2.2 Computing F_N from Interaction Energy

In DFT, there are two common calculations that one can perform: 1) self-consistent field (SCF) calculations, where the ground state energy of the system is obtained by solving the KS equations self-consistently, and 2) geometry optimization, where the atomic coordinates of the system are adjusted through multiple cycles of energy and force evaluations until equilibrium is reached (i.e., until the forces acting on each atom $\rightarrow 0$, and the total energy is minimized).

One way of computing the normal load is by performing multiple energy evaluations at the same x position for different interlayer distances. This will generate different energy values corresponding to the interlayer distances, $d = d_1, d_2, ..., d_n$. The normal load at that particular x position can then be evaluated using the scheme described by Zhong *et al.*[189, 190] by taking the derivative of the interaction energy, E, with respect to the interlayer distance, d. This process can be repeated at different x positions to get the respective normal loads at those positions. However, if instead of single-point energy evaluations, a geometry optimization is performed (on the z coordinates of the atoms, while keeping the other coordinates frozen) at each sliding position, x_i, an optimal interlayer distance, d_i, that gives the lowest energy, E_i, will be obtained. Thus, for the range of sliding coordinates, $x_1, x_2, .., x_n$, we will obtain optimized interlayer distances, $d = d_1, d_2, ..., d_n$, and energies, $E = E_1, E_2, ..., E_n$. The normal load at position x will then be computed by taking the derivative of E with respect to d, such that

$$F_N = -\frac{\partial E}{\partial d}. \tag{5.2}$$

In our work, a geometry optimization was performed at each sliding position $x_i = x_1, x_2, ..., x_n$. Since d values where obtained from the optimizations, these values were not evenly spaced. Taking numerical derivatives (e.g., using finite difference algorithms) directly from this data yielded unstable and inconsistent results. Curve fitting methods were therefore employed instead, in a similar manner to that used in previous studies by Wang *et al.*[191–193] The normal loads were then evaluated by taking the derivative of the fit function. A normal load was obtained at each sliding position, x, corresponding to the change in energy with respect to interlayer distance at that particular position. The average friction was computed from an averaged normal force across the entire sliding scan. This averaged normal load is a good approximation of the intrinsic normal force of each material when no external loads are applied. Any value of the normal force below this minimum threshold bares no physical meaning.[194]

5.2.3   Position-Dependent Potential Energy, $V(x, F_N)$

As the top layer slides above the substrate, the overlayer atoms experience a potential that depends on the position of the sliding body and varies in accordance with the work done by the force normal to the substrate at each sliding position. The position-dependent potential, $V(x, F_N)$, is defined as

$$V(x, F_N) = E(d) + F_N d(x) - V_0, \tag{5.3}$$

where the first term is the interaction energy, the second term is the work done by the normal force, and V_0 is a relative term that can be chosen arbitrarily as a reference point. In this work, V_0 was taken to be the potential at the minimum-energy point along the sliding coordinate.

5.2.4   Computing the Coefficients of Friction, μ

Since $V(x, F_N)$ varies at each x position due to variations in the interlayer energy and the work done at each position, we can define a position-dependent force along x by taking the derivative of $V(x, F_N)$, such that

$$F_x(x, F_N) = \frac{\partial V(x, F_N)}{\partial x} \tag{5.4}$$

is a lateral force in the x direction and is perpendicular to F_N, as shown in Figure 5.1. Since this force is in the opposite direction to the motion of the body, the maximum value of F_x gives the static friction, $F_r = |F_x|$. To calculate the kinetic friction, we average F_r using

$$\langle F_r \rangle = \frac{\Delta V}{\Delta x}, \tag{5.5}$$

Figure 5.1: An illustration of the relationship between the normal force, F_N, and the lateral force, F_x, during interlayer sliding.
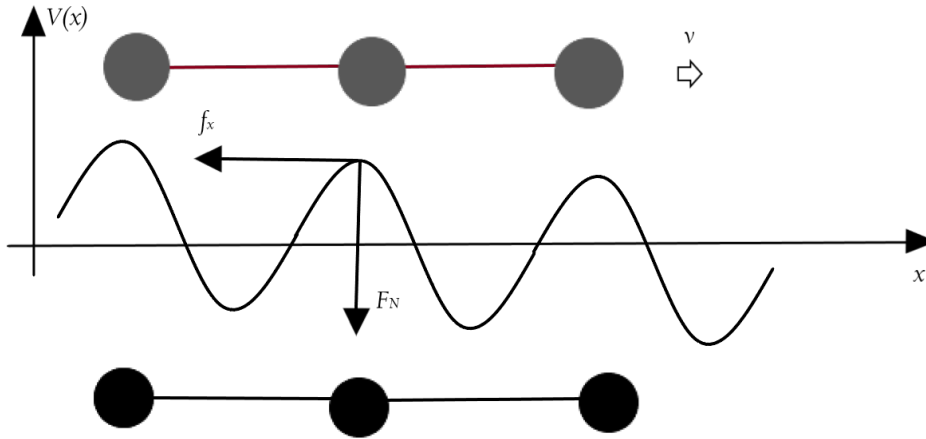
where ΔV is the difference between the maximum and the minimum $V(x, F_N)$, and Δx is the corresponding change in x. Finally, we obtain the coefficients of friction by applying the empirical law of friction 5.1,

$$\mu = \frac{\langle F_r \rangle}{F_N}. \tag{5.6}$$

The scheme described above[189, 190] was implemented in MATLAB code for the purpose of computing the coefficients of friction for this work. The energy values were converted to Joules, and all the fractional coordinates to meters, in order to obtain the forces in Newtons. Note that the values of μ are dimensionless.

5.3   Results and Discussion

Table 5.1 shows the coefficients of friction obtained from $E(d)$ data fit to first, third, and fifth degree polynomials, and sums of 1, 3, and 5 sine functions. μ values were computed from the normal loads obtained using Equation 5.2. For the commensurate cells, the data is nearly linear. Therefore, only polynomial fits were considered in the analysis. The data from the incommensurate geometries, on the other hand, was mostly random and not representative of any mathematical function. However, due to the similarity of the points (very small changes in the interlayer distance and interlayer energy lead to virtually flat potentials for the incommensurate cells compared to their commensurate counterparts), an estimate value of μ was determined for each cell by averaging the performance of multiple fitting models, as reported in Table 5.1.

Table 5.1: Computed coefficients of friction using polynomial fits and sum of sine functions.

Material	(m, n)	Polynomial fitting			Sum of sines			Average μ
		$P(z)$	$P(z^3)$	$P(z^5)$	$n = 1$	$n = 3$	$n = 5$	
Graphene	(1×1)	0.0789	0.06771	0.0768	–	–	–	**0.0745**
	$(2, 1)$	0.0170	0.0023	0.0029	0.0005	0.0019	0.0024	**0.0045**
	$(3, 1)$	0.0337	0.0005	0.0006	0.0002	0.0001	0.0001	**0.0059**
	$(3, 2)$	0.0080	0.0008	0.0005	0.0003	0.0003	0.0003	**0.0002**
h−BN	(1×1)	0.2948	0.1848	0.2014	–	–	–	**0.2270**
	$(2, 1)$	0.0020	0.0010	0.0009	0.0010	0.0012	0.0011	**0.0012**
	$(3, 1)$	0.0001	0.0004	0.0003	0.0002	0.0004	0.0008	**0.0004**
	$(3, 2)$	0.0073	0.0109	0.0003	0.0037	0.0023	0.0025	**0.0049**
MoS$_2$	(1×1)	0.0417	0.1390	0.1475	–	–	–	**0.1094**
	$(2, 1)$	0.0073	0.0008	0.0010	0.0009	0.0010	0.0009	**0.0020**
	$(3, 1)$	0.0002	0.0006	0.010	0.0003	0.0003	0.0003	**0.0020**
	$(3, 2)$	0.0172	0.0034	0.0026	0.0029	0.0018	0.0021	**0.0050**
b−P	(1×1)	0.0195	0.0525	0.0474	–	–	–	**0.0398**
	$(2, 1)$	0.0030	0.0039	0.0038	0.0229	0.0038	0.0039	**0.0069**
	$(3, 1)$	0.0014	0.0015	0.0018	0.0026	0.0015	0.0023	**0.0018**
	$(3, 2)$	0.0005	0.0011	0.0013	0.0053	0.0016	0.0036	**0.0022**

5.3.1   Commensurate Structures

Graphene 1×1

The interlayer distance for the commensurate graphene structure increased with the interaction energy, as shown in Figure 5.2. d was lowest at the global minima (where the atomic layers were staggered, corresponding to an AB stacking) due to weak non-bonded repulsion when the C atoms were not vertically aligned. Likewise, the maximum value for d was seen at the 1/3 fractional coordinate, where the non-bonded repulsion was greatest. For most of the fitting models considered in this work, the largest values of μ appeared at sliding coordinates near the maximum interlayer distance, probably due to the reduction in the normal force at those points. The net normal load decreased at positions where the non-bonded repulsive effects were greatest due to the cancellation of forces in the z direction, i.e., the normal force pushing against the substrate with a negative sign (from Equation 5.2) will be resisted by a repulsive force acting in the opposite direction along the z axis.

Figure 5.3 shows the relationship between the lateral force, F_x, and the fractional sliding coordinate. Although the shape of F_x heavily relied on the method used to take the derivative of the position-dependent position, $V(x, F_N)$, (in our case, a sum of 3 sine functions was fit to the $V(x, F_N)$ data, then differentiated with respect to the sliding coordinate), the maximum of the F_x curve is a good

approximation to the static friction.[189]

The coefficients of friction for the commensurate graphene structure ranged between $0.067 - 0.079$, leading to an average μ value of 0.0745. Previous DFT studies using the Zhong *et al.* procedure[189,190] to compute the coefficients of friction between two layers of hydrogenated graphene sheets[191] have reported similar μ values with normal loads between $1 - 9$ nN (for clean graphene sheets, μ values between $0.06 - 0.25$ were reported[191]). In this work, normal loads between $0.1 - 0.3$ nN were computed for the commensurate case. We observed an increase in normal load with system size, i.e., the average normal load in the incommensurate structures was greater due to the larger number of atoms, which lead to higher interaction energies.

h−BN 1×1

Similar to commensurate graphene, the relationship between the interlayer distance and the interaction energy was nearly linear, as shown in Figure 5.2. The lowest interlayer distances were seen at the 0.00 and 1.00 sliding coordinates, where the B and N atoms were directly aligned to maximize favourable electrostatic interactions. Likewise, the interlayer distance was greatest at the $^1/_3$ sliding coordinate due to non-bonded repulsion when the N atoms were directly aligned, and the B atoms staggered. Contrary to the other 3 materials, the normal load became more negative (see Figure 5.2) at large interlayer distances for most of the models used in this analysis. This is likely due to partial positive contributions from the B atoms plus dispersion attractive interactions, which summed up to a downward net force (i.e., normal force) slightly greater than the non-bonded repulsion from the N atoms. Notice the small changes in the normal load and coefficient of friction for h−BN in comparison to the other materials. The normal load and the coefficient of friction for h−BN were virtually constant throughout the sliding scan due to the interplay between the attractive dispersion interactions and non-bonded repulsion, which lead to a cancellation of forces in the normal direction. An average coefficient of friction of 0.2270 was computed. This is in good agreement with a previous first-principles study[194] of friction in h−BN (where predicted μ values ranged between $0.223 - 0.265$), and with experiment (where μ values between $0.23 - 0.25$ were measured).[195]

MoS$_2$ 1×1

Figure 5.2 shows the nearly linear correlation between the interlayer distance and the interaction energy, similar to graphene and h−BN. The lowest interlayer distances were seen when the Mo atoms were aligned with S atoms to maximize favourable electrostatic interactions, while the largest distances occurred when the Mo atoms were staggered and the more electronegative S atoms were aligned to maximize non-bonded repulsion. We observe a similar behaviour to graphene, where the normal load is reduced in magnitude for large values of d. The computed coefficients of friction ranged between $0.04 - 0.15$ for normal loads

loads between $0.1 - 0.3$ nN. No first-principles analyses of the coefficient of friction for MoS_2 bilayers were found in the literature. However, experimental studies have reported very low coefficients of friction for MoS_2 ranging between $0.02 - 0.25$,[196, 197] and a surprising reduction of μ for increased loads.[198] Notice the large values of F_N (Figure 5.2) and F_x (Figure 5.3) in comparison to the other materials. Despite the large normal loads in MoS_2, the average coefficient of friction is still comparatively low. This suggests that the MoS_2 structure can sustain large loads while maintaining a low coefficient of friction, which makes it an ideal material for high-load applications.[198]

b−P 1×1

Similar to graphene, h−BN, and MoS_2, the interlayer distance increased proportionally to the interaction energy and the largest increase in d was observed in b−P. The normal force was greatest when d was small, following a similar behaviour observed in graphene and MoS_2. However, the magnitude of the normal load was least in b−P, as shown in Figure 5.2. Although no theoretical or experimental studies regarding the tribological properties of b−P have been found in the literature, the smaller values of F_N may suggest a low load tolerance of this material. On the other hand, low coefficients of friction (between $0.02-0.05$, as shown in Table 5.1) were computed for b−P, likely due to the size of the unit cell (the b−P unit cell is about 0.8 times larger than the graphene 1×1 cell), since average friction involves dividing by the change in x, i.e., the displacement in the x direction. Despite having the highest energy barriers and low normal loads, the low coefficients of friction suggest that good tribological properties can be expected in b−P, which would be well-suited for low-load applications, e.g., in nanoelectromechanical systems (NEMS).[31, 39, 199]

5.3.2 Incommensurate Structures

The coefficients of friction for the incommensurate structures were computed for all materials in an analogous manner to the commensurate cells. Since all the rotated cells exhibited similar ultra-low friction behavior, we will only discuss the $(2, 1)$ case.

Unlike the commensurate cells, the relationship between the interlayer distance and the interaction energy was not very straightforward due to the misalignment of the atoms leading to distribution of contact points between the atomic layers and a disruption of distinct stationary position (i.e., minima and maxima on the energy and distance plots). In general, the smallest changes in the interlayer distance were seen in these cells, as well as the lowest predictions of μ ($\sim 1 - 3$ orders of magnitude lower than for the commensurate cells, as reported in Table 5.1). The lowest changes in the interlayer distance were observed in graphene ($0.00 - 1.2 \times 10^{-4}$ nm), followed by h−BN ($0.00 - 2 \times 10^{-4}$ nm), MoS_2 ($0.00 - 6 \times 10^{-4}$ nm), and b−P ($0.00 - 6 \times 10^{-3}$ nm), as shown in Figure 5.4.

Note the positive component of the normal loads in Figure 5.4, signifying a change in direction of the

Figure 5.2: Results for commensurate unit cells of (a) graphene, (b) h−BN, (c) MoS$_2$, and b−P. Shown for each material: 1) the relationship between the interlayer distance and the sliding coordinate (top left), 2) the interaction energy and the sliding coordinate (top right), 3) the relationship between the normal load and the sliding coordinate (bottom left), and 4) the coefficient of friction at different sliding positions (bottom right). The red horizontal line is the value of μ computed from the average friction, and the average normal load. These values have been reported in Table 5.1 for various curve fitting methods. The results shown below were computed by fitting third degree polynomials to the $E(d)$ data.

(a) Graphene (1×1)

(b) h−BN (1×1)

(c) MoS$_2$ (1×1)

(d) b−P (1×1)
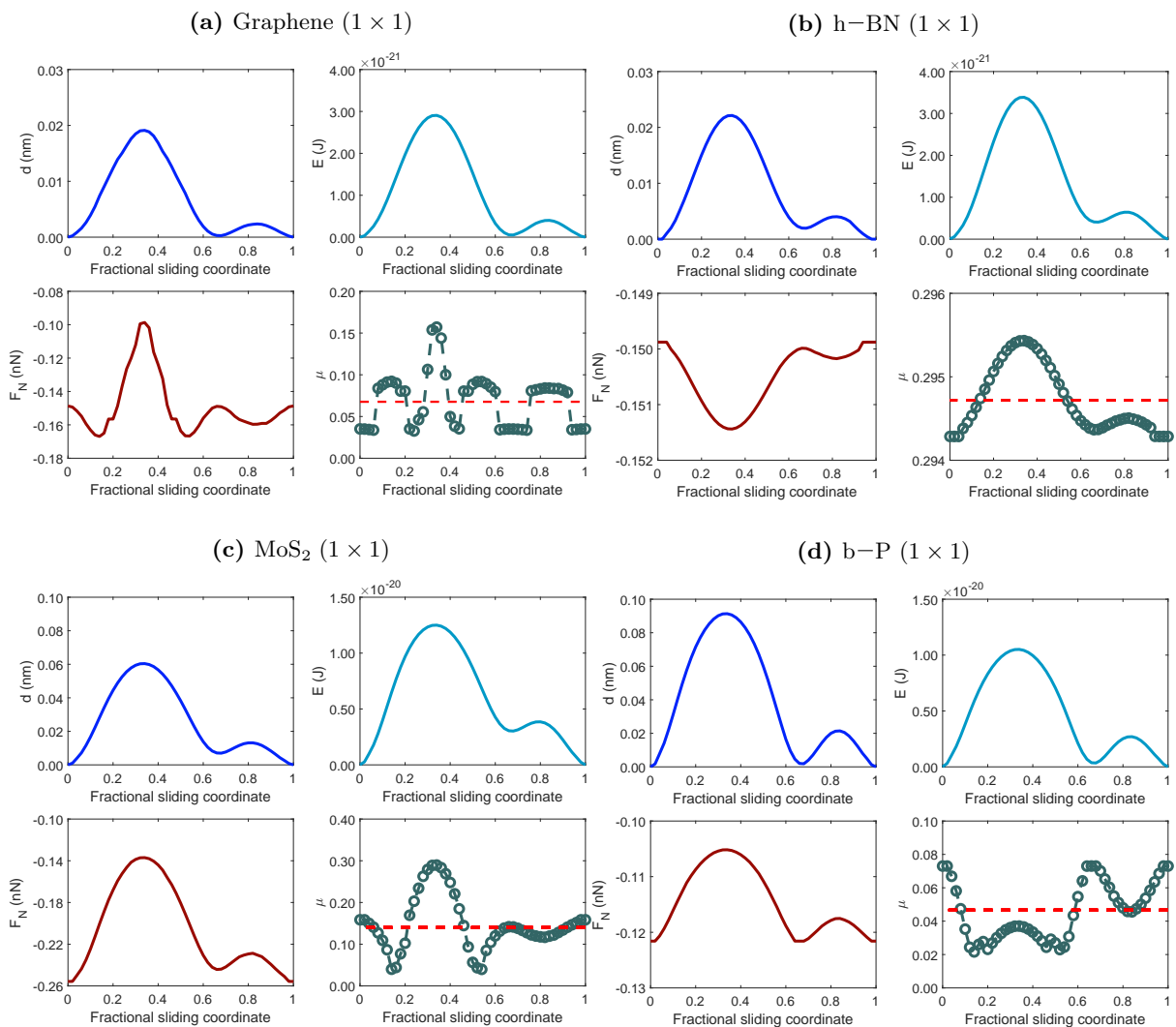
Figure 5.3: The relationship between the friction and sliding coordinate for commensurate (a) graphene, (b) h−BN, (c) MoS$_2$, and (d) b−P. The red and the broken lines represent the friction and the lateral force, respectively.

(a) Graphene (1×1)

(b) h−BN (1×1)

(c) MoS$_2$ (1×1)

(d) b−P (1×1)
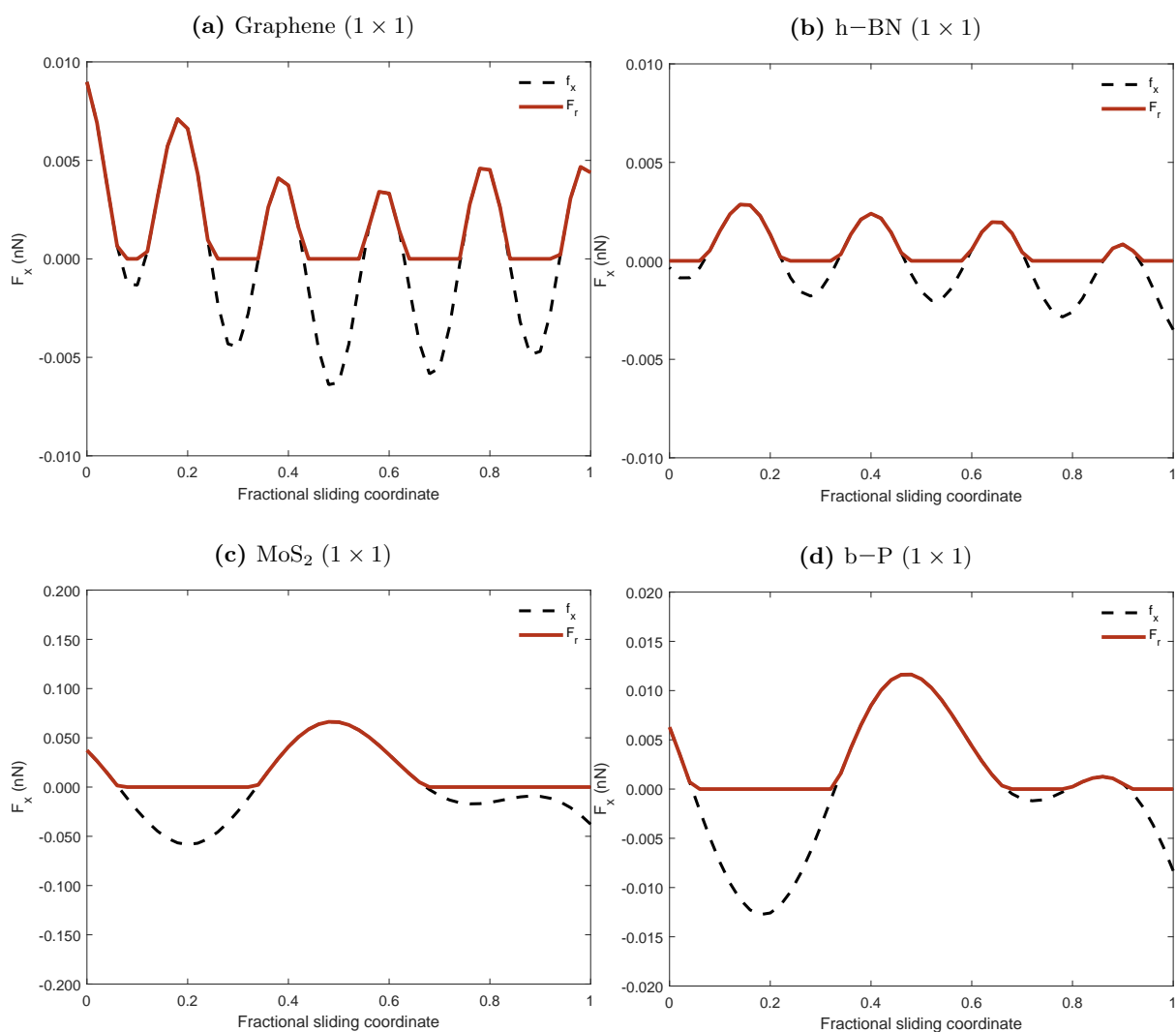
normal force. In the commensurate cells, the load was consistently negative, implying that this force was constantly pushing the overlayer against the substrate (i.e., doing work to the substrate in accordance with Equation 5.3). This gives us some insight into the mechanism of superlubricity; during sliding with ultra-low friction, the change in direction of the normal force implies that work was being done to the overlayer by the substrate. This process leads to a change in direction of the friction, meaning that during superlubric sliding, friction is not only significantly decreased, but also supports sliding of the overlayer. Some fitting models employed in this work yielded negative values of μ at some sliding coordinates (e.g., the negative spikes in Figure 5.4 (d)), which may be artifacts of the fitting process. In Table 5.1, we report the average coefficients of friction (denoted by the red horizontal lines on the plots) computed from the average absolute values of the normal load and the friction.

As shown in Figure 5.5, the lowest friction occurred in graphene, followed by h−BN, MoS_2, and b−P, which corresponds to the trend in the energy barriers from our DFT analysis in Chapter 4. However, for the $(2, 1)$ case, the lowest average coefficient of friction was obtained in h−BN, followed by MoS_2, graphene, and b−P (see Table 5.1), although the computation of μ was highly sensitivity to the fitting model used with an error of about 0.01. Nevertheless, we observe from the low coefficients of friction obtained for the rotated cells a clear exhibition of ultra-low friction in these incommensurate structures, as predicted in Chapter 4.

5.4 Conclusions

In this chapter, we have demonstrated how to compute the coefficients of friction from raw DFT results using the scheme developed by Zhong *et al.*[189, 190] The normal forces of a system can be computed by taking the negative derivative of the interaction energy with respect to the interlayer distance. An expression for the position-dependent potential can then be defined, which is a sum of the interaction energy and the work done by the normal force. The average friction is the derivative of this potential with respect to the sliding position. To evaluate the coefficients of friction, the classical physics equation of friction can then be employed to finally compute μ.

We have implemented the procedure described by Zhong *et al.*[189, 190] in a MATLAB code to compute μ using different polynomial fits for the energy-distance data obtained from DFT geometry optimizations. The estimated μ values were computed by averaging over the fitting methods used. First, third, and fifth degree polynomials were used, as well as sums of 1, 3, and 5 sine functions. The μ values computed for the commensurate cells of graphene, h−BN, and MoS_2 are in excellent agreement with available literature results. The trend in friction for the rotated cells was as follows: graphene < h−BN < MoS_2 < b−P, which agrees with the order of the energy barriers obtained from DFT in Chapter 4. Coefficients of friction $\sim 1 - 3$ orders of magnitude lower than the commensurate structures were obtained for the

Figure 5.4: Results for the $(2, 1)$ incommensurate unit cells of (a) graphene, (b) h−BN, (c) MoS$_2$, and b−P. Shown for each material: 1) the relationship between the interlayer distance and the sliding coordinate (top left), 2) the interaction energy and the sliding coordinate (top right), 3) the relationship between the normal load and the sliding coordinate (bottom left), and 4) the coefficient of friction at different sliding positions (bottom right). The red horizontal line is the value of μ computed from the average friction, and the average normal load. These values have been reported in Table 5.1 for various curve fitting methods. The results shown below were computed by fitting a sum of 3 sine functions (graphene and h−BN) and third degree polynomials (MoS$_2$ and b−P) to the $E(d)$ data.

(a) Graphene $(2, 1)$

(b) h−BN $(2, 1)$

(c) MoS$_2$ $(2, 1)$

(d) b−P $(2, 1)$
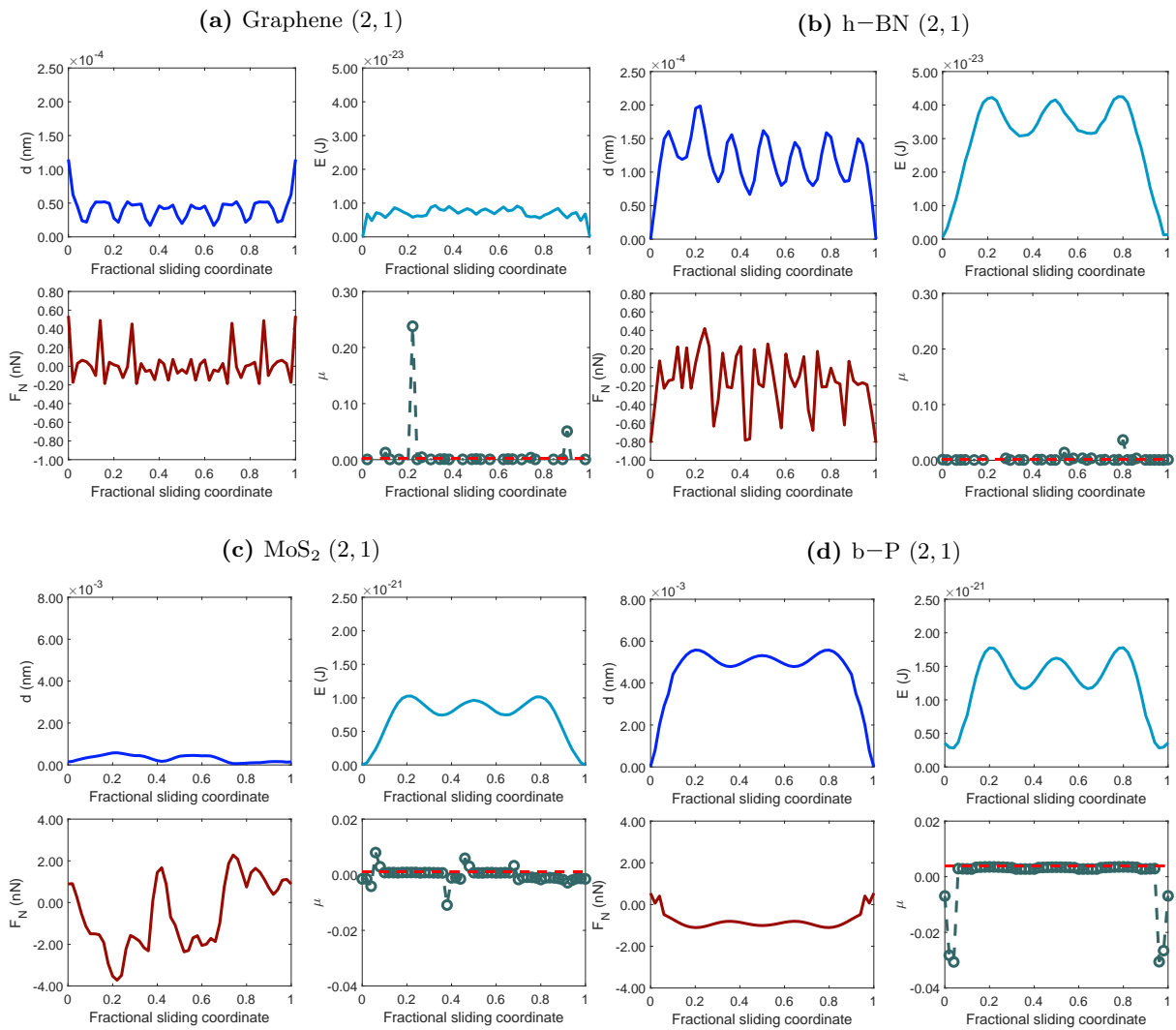
Figure 5.5: The relationship between the friction and sliding coordinate for the $(2, 1)$ incommensurate unit cell of (a) graphene, (b) h−BN, (c) MoS_2, and (d) b−P. The red and the broken lines represent the friction and the lateral force, respectively.

(a) Graphene $(2, 1)$

(b) h−BN $(2, 1)$

(c) MoS_2 $(2, 1)$

(d) b−P $(2, 1)$
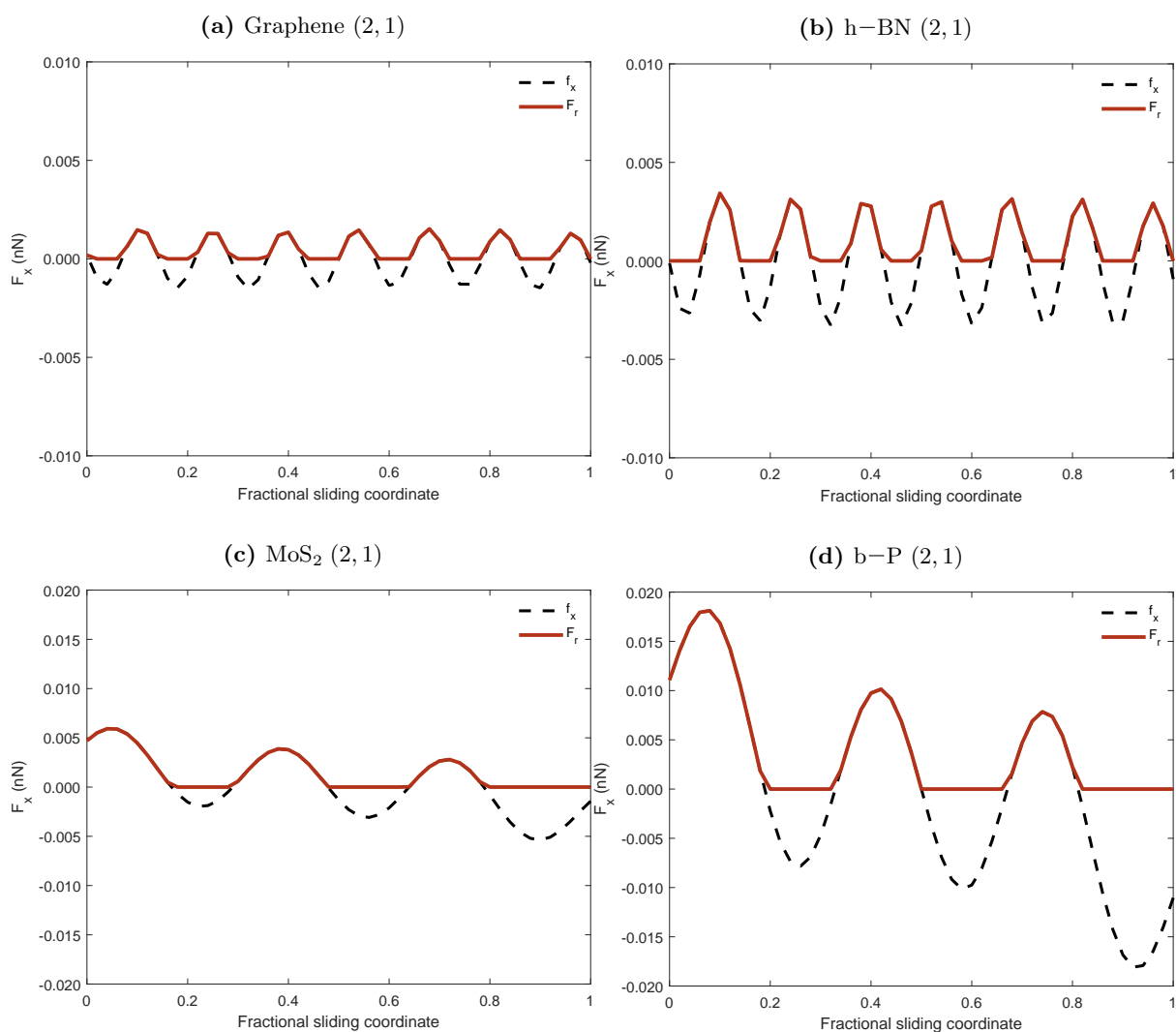
rotated cells. Large normal loads were obtained for MoS_2, with comparatively low coefficients of friction, suggesting a high load tolerance in this material. Conversely, low normal loads obtained for b−P, which were accompanied by low coefficients of friction, may suggest a low-load utility for b−P in nanoscale applications, such as nanoelectromechanical systems (NEMS).[31, 39, 199]

Insight into the mechanism of superlubricity during sliding was obtained by analyzing the normal forces. For the commensurate cells, the normal load was negative at all sliding positions, signifying work done to the substrate by the overlayer. The change in direction of the normal force during interlayer sliding indicated that work was being done by the substrate to the overlayer at some points during sliding. This resulted in a change in direction of the friction as well (i.e., in the direction that supported sliding), which promoted superlubric effects in the system. Since the substrate plays an important role in inducing superlubricity by means of doing work to the overlayer, changing the substrate type in tribological systems is a strategy that should be explored further, theoretically and experimentally.

Lastly, we hope that the work presented in this chapter, which combines quantum-mechanical results with classical-physics concepts, will foster innovation and further the pursuits for a more complete theory and understanding of ultra-low friction.

Chapter 6

Conclusions and Future Work

First-principles analyses of structural superlubricity in 2D materials were uncharted territory in frictional studies for many years due to the complexity of structurally constructing incommensurate systems, and the computational hardships associated with modeling them. The work presented in this thesis has addressed both of these issues by: 1) developing an open-source program that builds Moiré unit cells for planewave DFT codes, thereby permitting for the first time DFT calculations on computationally tractable incommensurate structures, and 2) demonstrating the efficacy of this innovative approach through a theoretical study of ultra-low friction in selected well-known solid lubricants, and the novel material b−P.

DFT has risen in popularity as a first-principles electronic structure method among computational researchers over the years for justifiable reasons. Unlike other computational chemistry methods, such as post-HF methods, DFT has an excellent trade-off between accuracy and computational cost. DFT methods have been shown to yield consistently reliable results in friction- and surface-related studies given an appropriate choice of exchange-correlation functional and dispersion model. The first half of Chapter **2** of this thesis was therefore dedicated to introducing DFT fundamentals, DFT functionals, and the accurate treatment of London dispersion in DFT calculations. The remaining half detailed Moiré pattern theory, on which the `BiCrystal` program is based.

An important feature of structural superlubricity is incommensurability, i.e., the structural misalignment of atoms in a system, which is characterized by Moiré patterns. In a 2D bilayer system, the periodicity and, hence, the size of the resulting Moiré unit cell, will be determined solely by the relative rotation angle between the layers. To our knowledge, there is currently no software or algorithm readily available for the purpose of creating Moiré unit cells for plane-wave DFT calculations. This deficit, combined with the insurmountable challenge of creating arbitrarily large Moiré unit cells by hand, was sufficient motivation to develop the `BiCrystal` program. In chapter **3**, the 8-step algorithm of the `BiCrystal` program was thoroughly discussed. Here, the usage and performance of this `python 3` code

were described, including examples and limitations of the program. From the performance curves, different components of the program were shown to scale differently with structure size. Replication of the top and bottom layers are the most computationally expensive subroutines in the code due to the inverse matrix operations required for every substrate and overlayer atom. Despite the computational challenge posed by these matrix operations, the program has demonstrated great reliability for large structures. Even for structures with as many as five thousand atoms and more, the `BiCrystal` program was able to generate sensible results within a few minutes. This far exceeds the system-size limit of standard DFT codes, which are confined to only a few hundred atoms due to the computational cost of DFT itself. Nonetheless, endeavors to improve the overall performance and capabilities of the `BiCrystal` shall be pursued in future versions for optimization and research purposes. Moiré unit cells of graphene, $h-BN$, MoS_2, and $b-P$ generated using the program enabled the study of superlubricity of these materials from first principles.

In chapter 4, friction in both commensurate (i.e., structurally aligned) and incommensurate (misaligned) unit cells of graphene, $h-BN$, MoS_2, and $b-P$ was investigated by modeling the potential energy surfaces for interlayer sliding. Higher interlayer sliding barriers were predicted for MoS_2 and blue-P, compared to graphene and $h-BN$, which is likely due to the corrugation of the layers and the larger contact areas for the former two materials. The average of interlayer distances during commensurate sliding was consistently similar to the interlayer distance in the optimized incommensurate cells. The commensurate PES showed distinct minima and maxima that corresponded to low and high frictional points. On the other hand, no distinct stationary points were observed on the incommensurate PES. This was rationalized through understanding the distribution of contacts between the top and bottom layers. The distinct high and low friction contacts seen in the commensurate structures were terminated in the incommensurate structures. This led to flattening of the PES and gave rise to structural superlubricity in the rotated cells. The shape of the commensurate PES showed that the low-friction zig-zag sliding path previous predicted for commensurate MoS_2 should be observed for all 4 materials. However, much lower friction regimes will be achieved in the incommensurate geometries provided the rotation barriers can be overcome. Our detailed first-principles analysis of superlubricity using DFT has confirmed our understanding of the origin of ultra-low friction at the atomic level through the idea of averaged contacts in incommensurate configurations.

In many engineering and applied science fields, the coefficient of friction is more informative than the interaction energy. Explicitly computing the coefficient of friction not only provides convenience for researchers in the applied sciences, but can also reveal greater and more realistic insights into the frictional properties of the system. In chapter 5, a method for the explicit computation of the coefficient of friction from DFT results was therefore presented. The computed coefficients of friction were $1-3$ orders of magnitude lower for the rotated structures, evidencing structural lubricity in these incommensurate

systems. Further, an analysis of the normal loads indicated a high load tolerance in MoS_2, which highlighted its suitability for high-load applications. The low loads and low coefficients of friction predicted for b−P suggested a utility of this material for low-load applications, e.g., in nanotechnology.

For many years, incommensurability has been the center of attention in achieving superlubricity in 2D materials. We hope that our findings will provide a fresh perspective for future experimental work. Since achieving incommensurability in experimental settings is a challenge, perhaps targeting specific commensurate rotation angles rather than arbitrary ones may provide new strategies for achieving superlubricity, and bring us closer to the design of industrially applicable solid superlubricants.

Superlubricity will continue to motivate a lot of research across many fields due to its promise in diverse practical applications, from nanotribology in nanoelectromechanical systems (NEMS) to efficient clean energy through the lubrication of bearings in wind turbines.[31,39,199] The issue of incommensurability is not the only hinderance to superlubricity. Effects such as distortions of the edge atoms and surface contamination contribute to friction between the surfaces during sliding. These still remain open areas of research in ultra-low friction studies.

Lastly, superlubricity is intrinsically more prominent in heterostructures than in homogeneous ones.[15] This is due to the similarity in the lattice constant and periodicity of the overlayer and substrate in homogeneous materials, which promotes commensurability. It is harder to maintain incommensurability in homogeneous configurations because the lattices are more prone to collapse back into their default commensurate orientations. We hope to explore superlubricity in heterostructures in our future work.

Appendix A

BiCrystal: Supplementary Information

A.1   Download

The latest version of BiCrystal can be found on the author's github page. For more information, questions, thanks, bug reports and so forth, please contact Tilas Kabengele: tilas.kabengele@dal.ca.

A.2   Packages

`BiCrystal` is a Python 3 program that uses Scipy and Shapely libraries. Additionally, the Crystal and shapely packages, which are not part of the standard Python packages, must be installed. We do this in the terminal by using `pip` or `conda`, i.e.

```
$ pip install crystals
```

```
$ pip install shapely
```

or

```
$ conda install -c conda-forge crystals
```

```
$ conda install -c conda-forge shapely
```

For more information on crystals and shapely, visit: link to crystals and link to shapely packages, respectively.

A.3   Files

The files contained in the zip file from the source include

- **bicrystal** - Bash script which runs the python program.

- **cifs/** - Directory with sample cif files.

- **examples/** - Directory with 33 examples of Quantum ESPRESSO input files generated by BiCrystal.

- **periodic_table.csv** - Periodic table of elements.

- **code.py** - Python program to be called from bicrystal script.

A.4 Installation

Installation of `BiCrystal` follows the standard installation procedure for Unix environments. Below, we demonstrate the steps for installing the program within the Bash environment.

After downloading the files from the github repository, unzip to the directory of your choice. Next, make **bicrystal** and **program.py** into executables as follows:

```
$ chmod u+x bicrystal program.py
```

Next, we add this directory to the $PATH variable. In Bash, this can be done by adding the lines

```
$ export PATH="$/path/to/your/directory/with/bicrysal/:$PATH"
$ export PYTHONPATH="${PYTHONPATH}:/path/to/your/directory/with/bicrysal/"
```

to the **.bashrc** file which is normally located in the home directory. We open the ./bashrc file with any text editor, for example, vim, nano, gedit, emacs:

```
$ vim ~/.bashrc
```

After making the changes to the .bashrc file, save and close the file, and then source it using the source command

```
$ source ~/.bashrc
```

in order to activate the changes. The `BiCrystal` program is now ready for use. The usage of the program with examples is described in sections 3.2.2 and 3.2.3 of this work.

Bibliography

[1] B. G. Hatcher. The mechanisms of metallic friction and lubrication. *Phys. Bul.*, 18:254–258, 1967.

[2] J. Haider and M. S. J. Hashmi. Health and environmental impacts in metal machining processes. In *Comprehensive Materials Processing*, pages 7 – 33. 2014.

[3] K. Holmberg, P. Andersson, and A. Erdemir. Global energy consumption due to friction in passenger cars. *Tribol. Int*, 47:221 – 234, 2012.

[4] K. Holmberg and A. Erdemir. Influence of tribology on global energy consumption, costs and emissions. *Frict.*, 5:263–284, 2017.

[5] K. Holmberg and A. Erdemir. The impact of tribology on energy use and CO_2 emission globally and in combustion engine and electric cars. *Tribol. Int*, 135:389 – 396, 2019.

[6] C. J. Bart, E. Gucciardi, and S. Cavallaro. Biolubricant product groups and technological applications. In *Biolubricants*, pages 565 – 711. 2013.

[7] L. Prandtl. Ein gedankenmodell zur kinetischen theorie der festen körper. *ZAMM - J. Appl. Math. Mech. / Z. Angew. Math. Mech.*, 8:85–106, 1928.

[8] S. Aubry and P. Y. Le Daeron. The discrete Frenkel-Kontorova model and its extensions: I. Exact results for the ground-states. *Phys. D: Nonlin. Phenom.*, 8:381 – 422, 1983.

[9] S. Aubry. The twist map, the extended Frenkel-Kontorova model and the devil's staircase. *Phys. D: Nonlin. Phenom.*, 7:240 – 258, 1983.

[10] S. Fayeulle. Superlubricity: When friction stops. *Phys. Worl.*, 10:29–32, 1997.

[11] M. Hirano and K. Shinjo. Atomistic locking and friction. *Phys. Rev. B*, 41:11837–11851, 1990.

[12] M. Hirano. Superlubricity: A state of vanishing friction. *Wear*, 254:932–940, 2003.

[13] M. Dienwiebel, G. S. Verhoeven, N. Pradeep, J. W. M. Frenken, J. A. Heimberg, and H. W. Zandbergen. Superlubricity of graphite. *Phys. Rev. Lett.*, 92:11837–11851, 2004.

[14] S.-W. Liu, H.-P. Wang, Q. Xu, T.-B. Ma, G. Yu, C. Zhang, D. Geng, Z. Yu, S. Zhang, W. Wang, Y.-Z. Hu, H. Wang, and J. Luo. Robust microscale superlubricity under high contact pressure enabled by graphene-coated microsphere. *Nat. Comm.*, 8:14029, 2017.

[15] Y. Song, D. Mandelli, O. Hod, M. Urbakh, M. Ma, and Q. Zheng. Robust microscale superlubricity in graphite/hexagonal boron nitride layered heterojunctions. *Nat. Mater.*, 17:894–899, 2018.

[16] B. Jiang, Z. Zhao, Z. Gong, D. Wang, G. Yu, and J. Zhang. Superlubricity of metal-metal interface enabled by graphene and $MoWS_4$ nanosheets. *Appl. Surf. Sci.*, 520:146303, 2020.

[17] M. Dienwiebel, N. Pradeep, G. S. Verhoeven, H. W. Zandbergen, and J. W. M. Frenken. Model experiments of superlubricity of graphite. *Surf. Sci.*, 576:197 – 211, 2005.

[18] J. M. Martin, H. Pascal, C. Donnet, T. Le Mogne, J. L. Loubet, and T. Epicier. Superlubricity of MoS_2: Crystal orientation mechanisms. *Surf.Coat. Tech.*, 68-69:427 – 432, 1994.

[19] J. Martin, C. Donnet, T. Le Mogne, and T. Epicier. Superlubricity of molybdenum disulphide. *Phys. Rev. B*, 48:10583, 1993.

[20] V. E. P. Claerbout, T. Polcar, and P. Nicolini. Superlubricity achieved for commensurate sliding: MoS_2 frictional anisotropy *in silico*. *Comput. Mater. Sci.*, 163:17 – 23, 2019.

[21] K. Liu, L. Zhang, T. Cao, C. Jin, D. Qiu, Q. Zhou, A. Zettl, P. Yang, S. G. Louie, and F. Wang. Evolution of interlayer coupling in twisted molybdenum disulfide bilayers. *Nat. Comm.*, 5:1–6, 2014.

[22] S. Jain, V. Juričić, and G. T. Barkema. Structure of twisted and buckled bilayer graphene. *2D Mater.*, 4:015018, 2016.

[23] L. Huder, A. Artaud, T. Le Quang, G. Trambly de Laissardiere, A. G. M. Jansen, G. Lapertot, C. Chapelier, and V. T. Renard. Electronic spectrum of twisted graphene layers under heterostrain. *Phys. Rev. Lett.*, 120:156405, 2018.

[24] V.L. Pokrovsky and A. L. Talapov. Ground state, spectrum, and phase diagram of two-dimensional incommensurate crystals. *Phys. Rev. Lett.*, 42:65–67, 1979.

[25] C. R. Woods, L. Britnell, A. Eckmann, R. S. Ma, J. C. Lu, H. M. Guo, X. Lin, G. L. Yu, Y. Cao, R. V. Gorbachev, A. V. Kretinin, J. Park, L. A. Ponomarenko, M. I. Katsnelson, Yu.N. Gornostyrev, K. Watanabe, T. Taniguchi, C. Casiraghi, H.-J. Gao, A. K. Geim, and K. S. Novoselov. Commensurate–incommensurate transition in graphene on hexagonal boron nitride. *Nat. Phys.*, 10:451–456, 2014.

[26] K. Uchida, S. Furuya, J. Iwata, and A. Oshiyama. Atomic corrugation and electron localization due to Moiré patterns in twisted bilayer graphenes. *Phys. Rev. B*, 90:155451, 2014.

[27] G. Ru, W. Qi, K. Tang, Y. Wei, and Y. Xue. Interlayer friction and superlubricity in bilayer graphene and $MoS_2/MoSe_2$ van der Waals heterostructures. *Tribol. Inter.*, 151:106483, 2020.

[28] I. Leven, D. Krepel, O. Shemesh, and O. Hod. Robust superlubricity in graphene/h-BN heterojunctions. *J. Phys. Chem. Lett.*, 4:115–120, 2013.

[29] Y. Guo, J. Qiu, and W. Guo. Reduction of interfacial friction in commensurate graphene/h-BN heterostructures by surface functionalization. *Nanoscale*, 8:575–580, 2016.

[30] J. Wang, L. Li, Z. Shen, P. Guo, M. Li, B. Zhao, L. Fang, and L. Yang. Ultralow interlayer friction of layered electride Ca_2N: A potential two-dimensional solid lubricant material. *Mater.*, 11:2462, 2018.

[31] R. Vazirisereshk, H. Ye, Z. Ye, A. Otero-de-la Roza, Meng-Qiang Zhao, Zhaoli G., A. T. C. Johnson, E. R. Johnson, R. W. Carpick, and A. Martini. Origin of nanoscale friction contrast between supported graphene, MoS_2, and a graphene/MoS_2 heterostructure. *Nano Lett.*, 19:5496–5505, 2019.

[32] A. E. Filippov, M. Dienwiebel, J. W. M. Frenken, J. Klafter, and M. Urbakh. Torque and twist against superlubricity. *Phys. Rev. Lett.*, 100:046102, 2008.

[33] A. S. de Wijn, C. Fusco, and A. Fasolino. Stability of superlubric sliding on graphite. *Phys. Rev. E*, 81:046105, 2010.

[34] M. M. van Wijk, M. Dienwiebel, J. W. M. Frenken, and A. Fasolino. Superlubric to stick-slip sliding of incommensurate graphene flakes on graphite. *Phys. Rev. B*, 88:235423, 2013.

[35] X. Feng, S. Kwon, J. Y. Park, and M. Salmeron. Superlubric sliding of graphene nanoflakes on graphene. *ACS Nano*, 7:1718–1724, 2013.

[36] M. Ma, A. Benassi, A. Vanossi, and M. Urbakh. Critical length limiting superlow friction. *Phys. Rev. Lett.*, 114:055501, 2015.

[37] A. Benassi, M. Ma, M. Urbakh, and A. Vanossi. The breakdown of superlubricity by driving-induced commensurate dislocations. *Sci. Rep.*, 5:16134, 2015.

[38] T. A. Sharp, L. Pastewka, and M. O. Robbins. Elasticity limits structural superlubricity in large contacts. *Phys. Rev. B*, 93:121402, 2016.

[39] Z. Baykara, R. Vazirisereshk, and A. Martini. Emerging superlubricity: A review of the state of the art and perspectives on future research. *Appl. Phys. Rev.*, 5:041102, 2018.

[40] Q. Li, Y. Dong, D. Perez, A. Martini, and R. W. Carpick. Speed dependence of atomic stick-slip friction in optimally matched experiments and molecular dynamics simulations. *Phys. Rev. Lett.*, 106:126101, 2011.

[41] A. Vanossi, C. Bechinger, and M. Urbakh. Structural lubricity in soft and hard matter systems. *Nat. Comm.*, 11:4657, 2020.

[42] Z. Liu, J. Yang, F. Grey, Jefferson Z. Liu, Y. Liu, Y. Wang, Y. Yang, Y. Cheng, and Q. Zheng. Observation of microscale superlubricity in graphite. *Phys. Rev. Lett.*, 108:205503, 2012.

[43] Q. Zheng, B. Jiang, S. Liu, Y. Weng, L. Lu, Q. Xue, J. Zhu, Q. Jiang, S. Wang, and L. Peng. Self-retracting motion of graphite microflakes. *Phys. Rev. Lett.*, 100:067205, 2008.

[44] M. Weiss and F. Elmer. Dry friction in the frenkel-kontorova-tomlinson model: Static properties. *Phys. Rev. B*, 53:7539, 1996.

[45] Y. Dong, A. Vadakkepatt, and A. Martini. Analytical models for atomic friction. *Tribol. Lett.*, 44:367–386, 2011.

[46] O. M. Braun, A. R. Bishop, and J. Röder. Hysteresis in the underdamped driven Frenkel-Kontorova model. *Phys. Rev. Lett.*, 79:3692–3695, 1997.

[47] A. Vanossi., J. Röder, A. R. Bishop, and V. Bortolani. Underdamped commensurate dynamics in a driven Frenkel-Kontorova–type model. *Phys. Rev. E*, 67:016605, 2003.

[48] E. Granato and S. Ying. Dynamical transitions and sliding friction in the two-dimensional Frenkel-Kontorova model. *Phys. Rev. B*, 59:5154, 1999.

[49] Martin H. Müser. Structural lubricity: Role of dimension and symmetry. *Europhys. Lett.*, 66:97–103, 2004.

[50] Y. Dong, Q. Li, and A. Martini. Molecular dynamics simulation of atomic friction: A review and guide. *J. Vac. Sci. Technol. A*, 31:030801, 2013.

[51] K. Wang, C. Qu, J. Wang, W. Ouyang, M. Ma, and Q. Zheng. Strain engineering modulates graphene interlayer friction by Moiré pattern evolution. *ACS Appl. Mater. Inter.*, 11:36169–36176, 2019.

[52] J. A. Harrison, C. T. White, R. J. Colton, and D. W. Brenner. Molecular-dynamics simulations of atomic-scale friction of diamond surfaces. *Phys. Rev. B*, 46:9700–9708, 1992.

[53] S. Jun, E. Hiroshi, Y. Masashi, and O. Etsuji. Molecular dynamics simulation of friction on the atomic scale. *Nanotech.*, 9:118–123, 1998.

[54] Q. Li, Y.Dong, D. Perez, A. Martini, and R. W. Carpick. Speed dependence of atomic stick-slip friction in optimally matched experiments and molecular dynamics simulations. *Phys. Rev. Lett.*, 106:126101, 2011.

[55] J. E. Lennerd-Jones. Cohesion. *Proc. Phys. Sci.*, 43:461–482, 1931.

[56] S. D. Murray and M. I. Baskes. Embedded-atom method: Derivation and application to impurities, surfaces, and other defects in metals. *Phys. Rev. B*, 29:6443–6453, 1984.

[57] D. W. Brenner. Empirical potential for hydrocarbons for use in simulating the chemical vapor deposition of diamond films. *Phys. Rev. B*, 42:9458–9471, 1990.

[58] S. J. Stuart, A. B. Tutein, and J. A. Harrison. A reactive potential for hydrocarbons with intermolecular interactions. *J. Chem. Phys.*, 112:6472–6486, 2000.

[59] A. C. T. van Duin, S. Dasgupta, F. Lorant, and W. A. Goddard. ReaxFF: A reactive force field for hydrocarbons. *J. Phys. Chem. A*, 105:9396–9409, 2001.

[60] T. Shan, B. D. Devine, T. W. Kemper, S. B. Sinnott, and S. R. Phillpot. Charge-optimized many-body potential for the hafnium/hafnium oxide system. *Phys. Rev. B*, 81:125328, 2010.

[61] J. Yu, S. B. Sinnott, and S. R. Phillpot. Charge optimized many-body potential for the Si/SiO_2 system. *Phys. Rev. B*, 75:085311, 2007.

[62] R. J. Bartlett and M. Musiał. Coupled-cluster theory in quantum chemistry. *Rev. Mod. Phys.*, 79:291, 2007.

[63] I. Shavitt and R. J. Bartlett. *Many-body methods in chemistry and physics: MBPT and coupled-cluster theory.* 2009.

[64] T. D. Crawford and H. F. Schaefer. An introduction to coupled cluster theory for computational chemists. *Rev. Comp. Chem.*, 14:33–136, 2000.

[65] I. Shavitt. The method of configuration interaction. In *Methods of electronic structure theory*, pages 189–275. 1977.

[66] J. A. Pople, M. Head-Gordon, and K. Raghavachari. Quadratic configuration interaction. a general technique for determining electron correlation energies. *J. Chem. Phys.*, 87:5968–5975, 1987.

[67] S. R. Langhoff and E. R. Davidson. Configuration interaction calculations on the nitrogen molecule. *Int. J. Quant. Chem.*, 8:61–72, 1974.

[68] H. B. Schlegel. Møller-Plesset perturbation theory with spin projection. *J. Phys. Chem.*, 92:3075–3078, 1988.

[69] S. Grimme. Improved second-order Møller-Plesset perturbation theory by separate scaling of parallel- and antiparallel-spin pair correlation energies. *J. Chem. Phys.*, 118:9095–9102, 2003.

[70] P. Pulay and S. Saebø. Orbital-invariant formulation and second-order gradient evaluation in Møller-Plesset perturbation theory. *Theor. Chim. Acta*, 69:357–368, 1986.

[71] M. Wolloch, G. Feldbauer, P. Mohn, J. Redinger, and A. Vernes. *Ab initio* friction forces on the nanoscale: A density functional theory study of fcc Cu(111). *Phys. Rev. B*, 90:195418, 2014.

[72] J. C. Spear, B. W. Ewers, and J. D. Batteas. 2D-nanomaterials for controlling friction and wear at interfaces. *Nano Today*, 10:301–314, 2015.

[73] Z. Ye, A. Otero de la Roza, E. R. Johnson, and A. Martini. Oscillatory motion in layered materials: graphene, boron nitride, and molybdenum disulfide. *Nanotech.*, 26:165701, 2015.

[74] V. L. Popov and J. A. T. Gray. Prandtl-Tomlinson model: History and applications in friction, plasticity, and nanotechnologies. *ZAMM - J. Appl. Math. Mech. / Z. Angew. Math. Mech.*, 92:683–708, 2012.

[75] H. Sakuma, K. Kawai, I. Katayama, and S. Suehara. What is the origin of macroscopic friction? *Sci. Adv.*, 4:eaav2268, 2018.

[76] M. S. Christian and E. R. Johnson. Effect of the metal substrate on interlayer interactions in bilayer graphene. *J. Phys. Chem. C*, 122:8910–8918, 2018.

[77] M. S. Christian, A. Otero-de-la Roza, and E. R. Johnson. Surface adsorption from the exchange-hole dipole moment dispersion model. *J. Chem. Theory Comput.*, 12:3305–3315, 2016.

[78] A. Otero-de-la-Roza, L. M. LeBlanc, and E. R. Johnson. Pairwise dispersion corrections can describe layered materials accurately. *J. Phys. Chem. Lett.*, 11:2298–2302, 2020.

[79] J. Moellmann and S. Grimme. Importance of london dispersion effects for the packing of molecular crystals: a case study for intramolecular stacking in a bis-thiophene derivative. *Phys. Chem. Chem. Phys.*, 12:8500–8504, 2010.

[80] M. Christian. *Modeling Dispersion interactions on metal surfaces using the exchange-hole dipole moment.* PhD thesis, Dalhousie University, 2018.

[81] K. Hermann. Periodic overlayers and Moiré patterns: theoretical studies of geometric properties. *J. Phys.: Conden. Matt.*, 24:314210, 2012.

[82] R. Bistritzer and A. H. MacDonald. Moiré bands in twisted double-layer graphene. *Proc. Nat. Acad. Sci.*, 108:12233–12237, 2011.

[83] G. Trambley de Laissardire, D. Mayou, and L. Magaud. Localization of dirac electrons in rotated graphene bilayers. *Nano Lett.*, 10:804–808, 2010.

[84] A. Otero-de-la Roza and Erin R. Johnson. van der Waals interactions in solids using the exchange-hole dipole moment model. *J. Chem. Phys.*, 136:174109, 2012.

[85] E. R. Johnson. The exchange-hole dipole moment dispersion model. In A Otero-de-la-Roza and G A DiLabio, editors, *Non-covalent Interactions in Quantum Chemistry and Physics*, chapter 5, pages 169–194. 2017.

[86] N. Mardirossian and M. Head-Gordon. Thirty years of density functional theory in computational chemistry: An overview and extensive assessment of 200 density functionals. *Mol. Phys.*, 115:2315–2372, 2017.

[87] D. G. Feitelson. The supercomputer industry in light of the top500 data. *Comput. Sci. Eng.*, 7:42–47, 2005.

[88] W. A. de Jong., E. Bylaska, N. Govind, C. L. Janssen, K. Kowalski, T. Müller, I. M. B. Nielsen, H. J. J. van Dam, V. Veryazov, and R. Lindh. Utilizing high performance computing for chemistry: Parallel computational chemistry. *Phys. Chem. Chem. Phys.*, 12:6896–6920, 2010.

[89] D. F. Bacon, S. Graham, and O. J. Sharp. Compiler transformations for high-performance computing. *ACM Comput. Surv.*, 26:345–420, 1994.

[90] D. Lim, T. R. Anderson, and T. Shott. Technological forecasting of supercomputer development: The march to exascale computing. *Omega*, 51:128 – 135, 2015.

[91] M. Born and R. Oppenheimer. Zur quantentheorie der molekeln. *Ann. Phys.*, 389:457–484, 1927.

[92] P. Hohenberg and W. Kohn. Inhomogeneous electron gas. *Phys. Rev.*, 136:B864–B871, 1964.

[93] W. Kohn and L. J. Sham. Self-consistent equations including exchange and correlation effects. *Phys. Rev. A*, 140:1133–1138, 1965.

[94] C.W. Gear, B. Leimkuhler, and G.K. Gupta. Automatic integration of Euler-Lagrange equations with constraints. *J. Comp. Appl. Math.*, 12-13:77 – 90, 1985.

[95] O. P. Agrawal. Formulation of Euler-Lagrange equations for fractional variational problems. *J. Math. Anal. Appl.*, 272:368 – 379, 2002.

[96] O. P. Agrawal. Generalized Variational Problems and Euler-Lagrange equations. *Comp. Math. Appl.*, 59:1852 – 1864, 2010.

[97] J. Schwinger. Thomas-Fermi model: The leading correction. *Phys. Rev. A*, 22:1827–1832, 1980.

[98] Y. Tal and R. F. W. Bader. Studies of the energy density functional approach. I. Kinetic energy. *Int. J. Quant. Chem.*, 14:153–168, 1978.

[99] J. Schwinger. *Thomas-Fermi model: The second correction*, pages 770–778. 1981.

[100] H. S. Yu, S. L. Li, and D. G. Truhlar. Perspective: Kohn-sham density functional theory descending a staircase. *J. Chem. Phys.*, 145:130901, 2016.

[101] A. J. Cohen, P. Mori-Sánchez, and W. Yang. Challenges for density functional theory. *Chem. Rev.*, 112:289–320, 2012.

[102] A. D. Becke. Density functional calculations of molecular bond energies. *J. Chem. Phys.*, 84:4524–4529, 1986.

[103] A. D. Becke. Completely numerical calculations on diatomic molecules in the local-density approximation. *Phys. Rev. A*, 33:2786, 1986.

[104] P. Ziesche, S. Kurth, and J. P. Perdew. Density functionals from LDA to GGA. *Comp. Mat. Sci.*, 11:122 – 127, 1998.

[105] A. Boese, N. L. Doltsinis, N. C. Handy, and M. Sprik. New generalized gradient approximation functionals. *J. Chem. Phys.*, 112:1670–1678, 2000.

[106] P. Haas, F. Tran, P. Blaha, K. Schwarz, and R. Laskowski. Insight into the performance of GGA functionals for solid-state calculations. *Phys. Rev. B*, 80:195109, 2009.

[107] A. D. Becke. On the large-gradient behavior of the density functional exchange energy. *J. Chem. Phys.*, 85:7184–7187, 1986.

[108] C. Adamo and V. Barone. Exchange functionals with improved long-range behavior and adiabatic connection methods without adjustable parameters: The mPW and mPW1PW models. *J. Chem. Phys.*, 108(2):664–675, 1998.

[109] A. D. Becke. Density-functional exchange-energy approximation with correct asymptotic behavior. *Phys. Rev. A*, 38:3098–3100, 1988.

[110] J. P. Perdew, K. Burke, and M. Ernzerhof. Generalized gradient approximation made simple. *Phys. Rev. Lett.*, 77:3865–3868, 1996.

[111] G. K. H. Madsen. Functional form of the generalized gradient approximation for exchange: The PBEα functional. *Phys. Rev. B*, 75:195108, 2007.

[112] B. Hammer, L. Hansen, and J. Nørskov. Improved adsorption energetics within density-functional theory using revised Perdew-Burke-Ernzerhof functionals. *Phys. Rev. B*, 59:7413, 1999.

[113] J. Perdew, K. Burke, and M. Ernzerhof. Perdew, Burke, and Ernzerhof reply. *Phys. Rev. Lett.*, 80:891, 1998.

[114] J. P. Perdew and W. Yue. Accurate and simple density functional for the electronic exchange energy: Generalized gradient approximation. *Phys. Rev. B*, 33:8800–8802, 1986.

[115] G. I Csonka, J. P. Perdew, A. Ruzsinszky, P. Philipsen, S. Lebègue, J. Paier, O. A. Vydrov, and J. G. Ángyán. Assessing the performance of recent density functionals for bulk solids. *Phys. Rev. B*, 79:155107, 2009.

[116] S. R. Whittleton, A. Otero-de-la Roza, and E. R. Johnson. Exchange-hole dipole dispersion model for accurate energy ranking in molecular crystal structure prediction. *J. Chem. Theory Comput.*, 13:441–450, 2017.

[117] S. Grimme. Density functional theory with london dispersion corrections. *WIREs Comp. Molec. Sci.*, 1:211–228, 2011.

[118] F. M. Fowkes. Attractive forces at interfaces. *Indust. Eng. Chem.*, 56:40–52, 1964.

[119] K. Berland, V. R. Cooper, K. Lee, E. Schröder, T. Thonhauser, P. Hyldgaard, and B. I. Lundqvist. van der Waals forces in density functional theory: a review of the vdW-DF method. *Reports on Progress in Physics*, 78:066501, 2015.

[120] S. Grimme, A. Hansen, J. G. Brandenburg, and C. Bannwarth. Dispersion-corrected mean-field electronic structure methods. *Chem. Rev.*, 116:5105–5154, 2016.

[121] J. Klimeš and A. Michaelides. Perspective: Advances and challenges in treating van der Waals dispersion forces in density functional theory. *J. Chem. Phys.*, 137:120901, 2012.

[122] B. M. Axilrod and E. Teller. Interaction of the van der Waals type between three atoms. *J. Chem. Phys.*, 11:299–300, 1943.

[123] A. Otero-de-la-Roza, L. M. LeBlanc, and E. R. Johnson. What is "many-body" dispersion and should I worry about it? *Phys. Chem. Chem. Phys.*, 22:8266–8276, 2020.

[124] S. Grimme. Semiempirical GGA-type density functional constructed with a long-range dispersion correction. *J. Comp. Chem.*, 27:1787–1799, 2006.

[125] S. Grimme, J. Antony, S. Ehrlich, and H. Krieg. A consistent and accurate ab initio parametrization of density functional dispersion correction (DFT-D) for the 94 elements H-Pu. *J Chem. Phys.*, 132:154104, 2010.

[126] S. Grimme. Accurate description of van der Waals complexes by density functional theory including empirical corrections. *J.Comp. Chem.*, 25:1463–1473, 2004.

[127] A. Tkatchenko, R. A. DiStasio Jr, R. Car, and M. Scheffler. Accurate and efficient method for many-body van der Waals interactions. *Phys. Rev. Lett.*, 108:236402, 2012.

[128] A. D. Becke and E. R. Johnson. Exchange-hole dipole moment and the dispersion interaction revisited. *J. Chem. Phys.*, 127:154108, 2007.

[129] E. R. Johnson and A. D. Becke. A post-Hartree-Fock model of intermolecular interactions: Inclusion of higher-order corrections. *J. Chem. Phys.*, 124:174104, 2006.

[130] A. Otero-de-la Roza and E. R. Johnson. Application of XDM to ionic solids: The importance of dispersion for bulk moduli and crystal geometries. *J. Chem. Phys.*, 153:054121, 2020.

[131] A. D. Becke and E. R. Johnson. Exchange-hole dipole moment and the dispersion interaction: High-order dispersion coefficients. *J. Chem. Phys.*, 124:014104, 2006.

[132] A. D. Becke and E. R. Johnson. A density-functional model of the dispersion interaction. *J. Chem. Phys.*, 123:154101, 2005.

[133] E. R. Johnson and A. D. Becke. A post-Hartree–Fock model of intermolecular interactions. *J. Chem. Phys.*, 123:024101, 2005.

[134] A. D. Becke and E. R. Johnson. Exchange-hole dipole moment and the dispersion interaction. *J. Chem. Phys.*, 122:154104, 2005.

[135] P. Giannozzi, S. Baroni, N. Bonini, M. Calandra, R. Car, C. Cavazzoni, D. Ceresoli, G.L. Chiarotti, M. Cococcioni, I. Dabo, A. Dal Corso, S. Fabris, G. Fratesi, S. de Gironcoli, R. Gebauer, U. Gerstmann, C. Gougoussis, A. Kokalj, M. Lazzeri, L. Martin-Samos, N. Marzari, F. Mauri, R. Mazzarello, S. Paolini, A. Pasquarello, L. Paulatto, C. Sbraccia, S. Scandolo, G. Sclauzero, A. P. Seitsonen, A. Smogunov, P. Umari, and R. M. Wentzcovitch. Quantum ESPRESSO: a modular and open-source software project for quantum simulations of materials. *J. Phys.: Conden. Matt.*, 21:395502, 2009.

[136] P. Giannozzi, O. Andreussi, T. Brumme, O. Bunau, M. B. Nardelli, M. Calandra, R. Car, C. Cavazzoni, D. Ceresoli, and M. Cococcioni. Advanced capabilities for materials modelling with Quantum ESPRESSO. *J. Phys: Condens. Matt.*, 29:465901, 2017.

[137] A. D. Becke. A multicenter numerical integration scheme for polyatomic molecules. *J. Chem. Phys.*, 88:2547–2553, 1988.

[138] F. L. Hirshfeld. Bonded-atom fragments for describing molecular charge densities. *Theor. Chim. Acta*, 44:129–138, 1977.

[139] T. C. Lillestolen and R. J. Wheatley. Redefining the atom: Atomic charge densities produced by an iterative stockholder approach. *Chem. Commun.*, pages 5909–5911, 2008.

[140] P. Bultinck, C. Van Alsenoy, P. W. Ayers, and R. Carbó-Dorca. Critical analysis and extension of the Hirshfeld atoms in molecules. *J. Chem. Phys.*, 126:144111, 2007.

[141] F. O. Kannemann and A. D. Becke. van der Waals interactions in density-functional theory: Intermolecular complexes. *J. Chem. Phys.*, 6:1081–1088, 2010.

[142] F. Bloch. Quantum mechanics of electrons in crystal lattices. *Z. Phys.*, 52:555–600, 1928.

[143] J. D. Pack and H. J. Monkhorst. "Special points for Brillouin-zone integrations"—a reply. *Phys. Rev. B*, 16:1748–1749, 1977.

[144] D. Hamann, M. Schlüter, and C. Chiang. Norm-conserving pseudopotentials. *Phys. Rev. Lett.*, 43:1494, 1979.

[145] G. Kresse and J. Hafner. Norm-conserving and ultrasoft pseudopotentials for first-row and transition elements. *J. Phys.: Conden. Matt.*, 6:8245, 1994.

[146] P. Giannozzi. Notes on pseudopotential generation. *Universit'a di Udine*, 2017.

[147] P. E. Blöchl. Projector augmented-wave method. *Phys. Rev. B*, 50:17953, 1994.

[148] G. Kresse and D. Joubert. From ultrasoft pseudopotentials to the projector augmented-wave method. *Phys. Rev. B*, 59:1758, 1999.

[149] J. C. Slater. An augmented plane wave method for the periodic potential problem. *Phys. Rev.*, 92:603, 1953.

[150] Z. Y. Rong and P. Kuiper. Electronic effects in scanning tunneling microscopy: Moiré pattern on a graphite surface. *Phys. Rev. B*, 48:17427, 1993.

[151] S. Marchini, S. Günther, and J. Wintterlin. Scanning tunneling microscopy of graphene on Ru (0001). *Phys. Rev. B*, 76:075429, 2007.

[152] G. Chen, A. L. Sharpe, P. Gallagher, I. T. Rosen, E. J Fox, L. Jiang, B. Lyu, H. Li, K. Watanabe, T. Taniguchi, J. Jung, Z. Shi, D. Goldhaber-Gordon, Y. Zhang, and F. Wang. Signatures of tunable superconductivity in a trilayer graphene Moiré superlattice. *Nature*, 572:215–219, 2019.

[153] I. Martin. Moiré superconductivity. *Annal. Phys.*, page 168118, 2020.

[154] F. Guinea and N. R. Walet. Electrostatic effects, band distortions, and superconductivity in twisted graphene bilayers. *Proc. Nat. Acad. Sci.*, 115:13174–13179, 2018.

[155] D. Mandelli, I. Leven, O. Hod, and M. Urbakh. Sliding friction of graphene/hexagonal–boron nitride heterojunctions: A route to robust superlubricity. *Sci. Rep.*, 7:1–10, 2017.

[156] D. Post, B. Han, and P. Ifju. *High sensitivity Moiré: Experimental analysis for mechanics and materials.* 2012.

[157] A. T. N'Diaye, S. Bleikamp, P. J. Feibelman, and T. Michely. Two-dimensional Ir cluster lattice on a graphene Moiré on Ir (111). *Phys. Rev. Lett.*, 97:215501, 2006.

[158] P. Moon and M. Koshino. Electronic properties of graphene/hexagonal-boron-nitride Moiré super-lattice. *Phys. Rev. B*, 90:155406, 2014.

[159] E. A. Wood. Vocabulary of surface crystallography. *J. Appl. Phys.*, 35:1306–1312, 1964.

[160] X. Zheng, L. Gao, Q. Yao, Q. Li, M. Zhang, X. Xie, S. Qiao, G. Wang, T. Ma, Z. Di, et al. Robust ultra-low-friction state of graphene via moiré superlattice confinement. *Nat. com.*, 7:1–7, 2016.

[161] D. Mandelli, I. Leven, O. Hod, and M. Urbakh. Sliding friction of graphene/hexagonal –boron nitride heterojunctions: a route to robust superlubricity. *Sci. Rep.*, 7:10851, 2017.

[162] S. Kawai, A. Benassi, E. Gnecco, H. Söde, R. Pawlak, X. Feng, K. Müllen, D. Passerone, C. A. Pignedoli, P. Ruffieux, R. Fasel, and E. Meyer. Superlubricity of graphene nanoribbons on gold surfaces. *Science*, 351:957–961, 2016.

[163] Mineralogical Society of America. American mineralogist crystal structure database. *European Journal of Mineralogy and Physics and Chemistry of Minerals*, 1963.

[164] J. M. Campanera, G. Savini, I. Suarez-Martinez, and M. I. Heggie. Density functional calculations on the intricacies of Moiré patterns on graphite. *Phys. Rev. B*, 75:235449, 2007.

[165] L. P. de Cotret, M. R. Otto, and B. J. Siwick. An open-source software ecosystem for the interactive exploration of ultrafast electron scattering data. *Adv. Struct. Chem. Imag.*, 4:11, 2018.

[166] W. Miller. *A treatise on crystallography.* 1839.

[167] H-J. Bunge. *Texture analysis in materials science: Mathematical methods.* 2013.

[168] A. Rollett and S. R. Wilson. Rodrigues vectors, unit quaternions. *Iowa State. Uni.*, 2014.

[169] R. Becker and S. Panchanadeeswaran. Crystal rotations represented as rodrigues vectors. *Text. Stres. Microstr.*, 10:167–194, 1989.

[170] Y. He and J. J. Jonas. Representation of orientation relationships in rodrigues–frank space for any two classes of lattice. *J. Appl. Crystal.*, 40:559–569, 2007.

[171] P Neumann. Representation of orientations of symmetrical objects by rodrigues vectors. *Text. Microstr.*, 14:53–58, 1991.

[172] K. Shinjo and M. Hirano. Dynamics of friction: Superlubric state. *Surf. Sci.*, 283:473–478, 1993.

[173] R. Zhang, Z. Ning, Y. Zhang, Q. Zheng, Q. Chen, H. Xie, Q. Zhang, W. Qian, and F. Wei. Superlubricity in centimetres-long double-walled carbon nanotubes under ambient conditions. *Nat. Nanotech.*, 8:912–916, 2013.

[174] L. Wang, X. Zhou, T. Ma, D. Liu, L. Gao, X. Li, J. Zhang, Y. Hu, H. Wang, Y. Dai, and J. Luo. Superlubricity of a graphene/MoS$_2$ heterostructure: a combined experimental and DFT study. *Nanoscale*, 9:10846–10853, 2017.

[175] S. Gražulis, D. Chateigner, R. T. Downs, A. F. T. Yokochi, M. Quirós, L. Letterotti, E. Manakova, J. Butkus, P. Moeck, and A. Le Bail. Crystallography Open Database – an open-access collection of crystal structures. *J. Appl. Crystal.*, 42:726–729, 2009.

[176] Tao Hu and Jisang Hong. Electronic structure and magnetic properties of zigzag blue phosphorene nanoribbons. *J. Appl. Phys.*, 118:054301, 2015.

[177] Xiang Xiao, Mingyong Wang, Jiguo Tu, and Shuqiang Jiao. The potential application of black and blue phosphorene as cathode materials in rechargeable aluminum batteries: A first-principles study. *Phys. Chem. Chem. Phys.*, 21:7021–7028, 2019.

[178] A. Kokalj. Computer graphics and graphical user interfaces as tools in simulations of matter at the atomic scale. *J. Mol. Graph. Model.*, 17:176–179, 1999.

[179] G. Kresse and D. Joubert. From ultrasoft pseudopotentials to the projector augmented-wave method. *Phys. Rev. B*, 59:1758–1775, 1999.

[180] W. Ouyang, I. Azuri, D. Mandelli, A. Tkatchenko, L. Kronik, M. Urbakh, and O. Hod. Mechanical and tribological properties of layered materials under high pressure: Assessing the importance of many-body dispersion effects. *J. Chem. Theory Comput.*, 16:666–676, 2020.

[181] A. Ambrosetti, A. M. Reilly, R. A. DiStasio Jr., and A. Tkatchenko. Long-range correlation energy calculated from coupled atomic response functions. *J. Chem. Phys.*, 140:18A508, 2014.

[182] Y. Dong, Z. Duan, Y. Tao, Z. Wei, B. Gueye, Y. Zhang, and Y. Chen. Friction evolution with transition from commensurate to incommensurate contacts between graphene layers. *Tribol. Inter.*, 136:259–266, 2019.

[183] P. Gallagher, M. Lee, F. Amet, P. Maksymovych, J. Wang, S. Wang, X. Lu, G. Zhang, K. Watanabe, T. Taniguchi, et al. Switchable friction enabled by nanoscale self-assembly on graphene. *Nat. com.*, 7:1–7, 2016.

[184] E. Koren, I. Leven, E. A. Knoll, O. Hod, and U. Duerig. Coherent commensurate electronic states at the interface between misoriented graphene layers. *Nat. Nanotechnol.*, 11:752–757, 2016.

[185] Z. Yu, A. Song, L. Sun, Y. Li, L. Gao, H. Peng, T. Ma, Z. Liu, and J. Luo. Understanding interlayer contact conductance in twisted bilayer graphene. *Small*, 16:1902844, 2020.

[186] J. C. Trinkle, J. Pang, S. Sudarsky, and G. Lo. On dynamic multi-rigid-body contact problems with coulomb friction. *ZAMM - J. Appl. Math. Mech. / Z. Angew. Math. Mech.*, 77:267–279, 1997.

[187] W. Townsend and J. Salisbury. The effect of coulomb friction and stiction on force control. In *Proceedings. 1987 IEEE International Conference on Robotics and Automation*, volume 4, pages 883–889. IEEE, 1987.

[188] N. Mostaghel and T. Davis. Representations of coulomb friction for dynamic analysis. *Earthq. Eng. Struct. Dyn.*, 26:541–548, 1997.

[189] W. Zhong and D. Tománek. First-principles theory of atomic-scale friction. *Phys. Rev. Lett.*, 64:3054–3057, 1990.

[190] D. Tománek, W. Zhong, and H. Thomas. Calculation of an atomically modulated friction force in atomic-force microscopy. *Europhys. Lett.*, 15:887–892, 1991.

[191] J. Wang, F. Wang, J. Li, S. Wang, Y. Song, Q. Sun, and Y. Jia. Theoretical study of superlow friction between two single-side hydrogenated graphene sheets. *Tribol. Lett.*, 48:255–261, 2012.

[192] J. Wang, F. Wang, J. Li, Q. Sun, P. Yuan, and Y. Jia. Comparative study of friction properties for hydrogen-and fluorine-modified diamond surfaces: A first-principles investigation. *Surf. Sci.*, 608:74–79, 2013.

[193] J. Wang, M. Li, X. Zhang, X. Cai, L. Yang, J. Li, and Y. Jia. An atomic scale study of ultralow friction between phosphorus-doped nanocrystalline diamond films. *Tribol. Inter.*, 86:85–90, 2015.

[194] J. Koskilinna, M. Linnolahti, and T. A. Pakkanen. Friction coefficient for hexagonal boron nitride surfaces from ab initio calculations. *Tribol. Lett.*, 24:37–41, 2006.

[195] T Saito and F Honda. Chemical contribution to friction behavior of sintered hexagonal boron nitride in water. *Wear*, 237:253–260, 2000.

[196] Janez Jelenc and Maja Remskar. Friction on a single mos 2 nanotube. *Nanoscale research letters*, 7(1):1–9, 2012.

[197] Mohammad R Vazirisereshk, Ashlie Martini, David A Strubbe, and Mehmet Z Baykara. Solid lubrication with mos2: a review. *Lubricants*, 7:57, 2019.

[198] T. Gradt and T. Schneider. Tribological performance of mos2 coatings in various environments. *Lub.*, 4:32, 2016.

[199] D. Berman, S. A. Deshmukh, S. K. R. S. Sankaranarayanan, A. Erdemir, and A. V. Sumant. Macroscale superlubricity enabled by graphene nanoscroll formation. *Science*, 348:1118–1122, 2015.